Master thesis and internship[BR]- Master's Thesis : Aerodynamic optimization of an aileron of a racing car[BR]- Stage d'insertion professionnelle

Auteur : Martínez Cacho, Alicia
Promoteur(s) : Andrianne, Thomas
Faculté : Faculté des Sciences appliquées
Diplôme : Cours supplémentaires destinés aux étudiants d'échange (Erasmus, ...)
Année académique : 2019-2020
URI/URL : http://hdl.handle.net/2268.2/10046

UNIVERSITY OF LIÈGE - FACULTY OF APPLIED SCIENCES

Aerodynamic optimization of an aileron of a racing car

Graduation Studies conducted for obtaining the Master's degree in Aerospace Engineering by **Alicia Martínez Cacho**

PROMOTOR: Thomas Andrianne

Academic year 2019-2020

Contents

List of Figures

List of Tables

Abstract

On a race car, aerodynamics has determined consequences on the performance on each circuit. The downforce contributes to a better tire performance on the corners, whereas a reduction of the drag makes possible to reach higher maximum velocities and to reduce the fuel consumption. One of the most common devices used to improve the downforce is the aileron. Nevertheless, the downforce generated comes together with a rise on the drag, leading to a need of a wide study to have a compromise between the two effects.

In this report, the aileron of the Fun Cup Evo 3 race car is studied to optimize its position regarding the angle of attack. This study is conducted by means of wind tunnel experiments on the wing isolated and numerical simulations of the 2D profile of the wing. In addition, the deflection of the flow upstream of the aileron generated by the car is determined with a wind tunnel experiment performed on a scale model of the car. The vertical deflection obtained, which varies spanwise, is used by the application of the Prandtl lifting line theory to estimate the performance of the aileron on real conditions. Finally, the results of these experiments are used to select three angles of attack that optimized the performance for different situations: maximum downforce-to-drag ratio, α between $-19°$ and $-9°$; maximum downforce, $\alpha = -23°$; and minimum drag, $\alpha = 7°$.

1. Introduction

1.1. Car aerodynamics

The study of the aerodynamics of a vehicle is an important part during the car design that covers a wide range of aspects. The aerodynamic of a car can be divided into the one related to the external flow and the related to the internal one. Among the external flow, the principal field of study is the one related to the aerodynamic forces and momentums generated due to the interaction between the vehicle and the flow field. Moreover, a detailed study of the flow field is important as some aspects like the mechanisms of soil deposition and the wind noise, among others, depend on such characteristics. Regarding the internal flow, the two principal features are the engine cooling and the climate system inside the car. In this project only the external aerodynamic forces are of interest. [1]

On a conventional passenger car, the only force with a real interest is the drag. The drag is defined as the aerodynamic force opposed to the velocity, with its same direction but in the opposite way. So, the drag must be reduced as much as possible. The main interest in reducing the drag is to save fuel. The lower the drag is, the less energy is needed to travel at a determined velocity and, therefore, the less waste of fuel will be. This aspect has become even more important last years due to the actual fuel price crisis and due to the environmental impacts of the exhaust emissions. [2]

The second reason of the importance of the drag reduction is to achieve higher velocities. Drag rises with the square of the velocity ($D = 0.5\rho V^2 A C_D$) and consequently it is a limiting characteristic as for the maximum velocity a car can reach. This last feature is especially important on race cars. But, on race car, not only a reduction of the drag is important but also an increase of the negative lift or downforce is essential to improve the race performance. In fact, race cars usually have a higher C_D than conventional passenger vehicles since a downforce rise is at expense of increase the drag. [1] Thus, the main objective of the external aerodynamic forces on the design of a race car is the compromise between both. That is, getting the needed downforce for better tire adhesion to go faster through corners [3] while maintaining the drag as low as possible in order to get a higher velocity on straight stretches and a less fuel consumption with the consequent weight reduction.
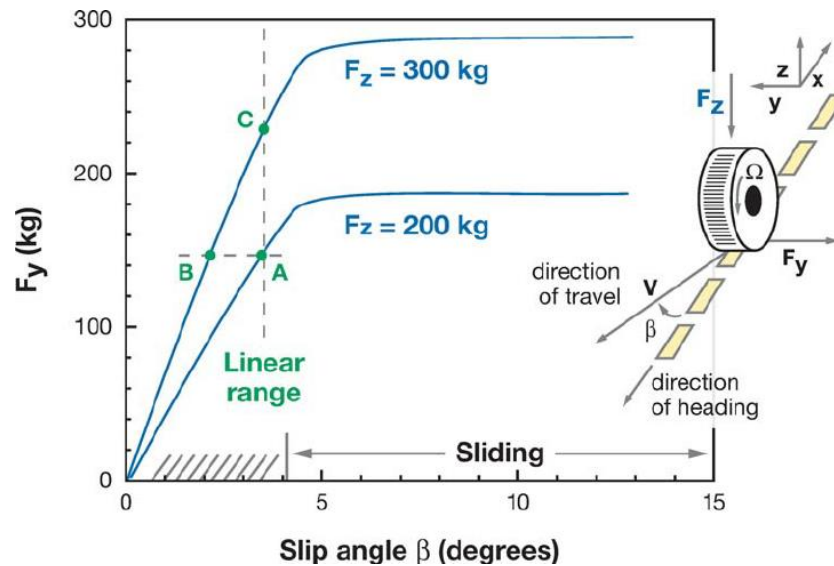
Figure 1. Effect of the downforce on the tire adhesion [4]

In order to have a better understanding of the effect of the downforce on tire adhesion, and subsequently on cornering, the Figure 1 is going to be analysed. This figure shows the side force or cornering force generated by the tire as a function of the slip angle, β, on a typical race car. To generate a side force an amount of slip angle is needed, but this force not only depends on the slip angle but also on the normal force. As it can be observed from the figure, an increase in the normal force implies a rise on the side force for a certain slip angle, and therefore, a rise on the cornering capacity that can be seen as an effective increment on the friction coefficient between the tire and the pavement. One way of increasing the normal force is by increasing the weight of the car, but this would also increase the side force needed to turn the car. So, for improving cornering ability, the normal negative force has to be risen without a penalty on car's weight. This could be got by the downforce. [4]

Considering that the increment in the normal force on the graphic between 200 kg and 300 kg is due to the downforce, the benefits of the downforce on the cornering performance can be analysed. Firstly, it can be observed that the maximum side force and therefore the maximum cornering speed is increased. Secondly, comparing the A point with the point B it can be seen that for turning at the same speed, that is to say, maintaining the side force needed, a lower slip angle is required and, consequently, the tire degradation is reduced. And finally, for maintaining the slip angle, points A and C, the side force is risen, and a higher cornering speed can be reached.
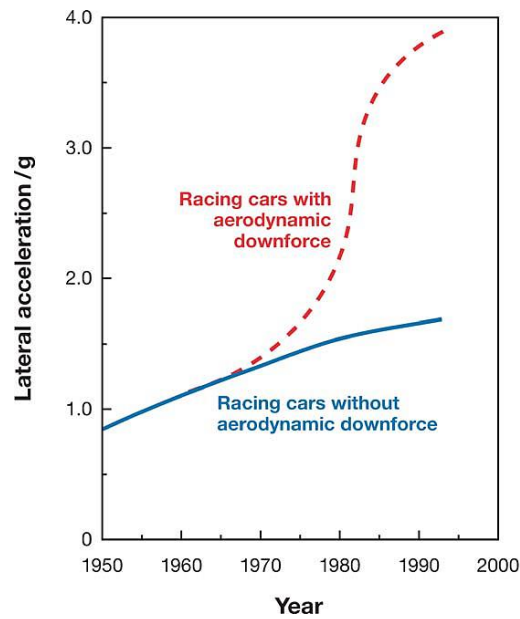
Figure 2. Evolution of the lateral acceleration on racing cars with and without aerodynamic downforce [4]

Once understood how the aerodynamic downforce improves the cornering ability, it is important to have a quantitative idea on the amount of this improvement. In order to do that, the Figure 2, in which the evolution of the maximum cornering speed is shown, can be observed. In this figure there are two lines, one broken line for the racing cars with aerodynamic downforce and a solid line for the race car without it. The reason why the broken line starts at the end of 1960s is due to the fact that the benefits of the downforce were unknown before this date and, because of this, the aerodynamic was focused exclusively on decreasing the drag. [4] The rise of the solid line is the result of the improvement of the tire technology with the years. [3] As can be observed, this upgrade is completely negligible comparing to the one obtained thanks to the aerodynamic downforce.

The next question is how the downforce can be generated. In a general manner, the downforce can be obtained by two ways: by modifying the vehicle's body shape and by adding inverting wings. Reducing the lift of the car's body, or getting a downforce with it, is based generally on getting a low pressure under the car. The body configuration that better matched this requirement is a low nose and an elevated tail, together with a smooth upper surface to reduce he drag. [4] Moreover, numerous elements can be added to facilitate obtaining a low pressure under the car, taking advantage of the ground effect. One of the most important ones is the usage of underbody channels also called diffusers or venture (as they are based on the Venturi effect). Other elements are the side skirts, that are flexible seals used to prevent the airflow from penetrating the area under the vehicle, but the regulations normally banned this type of elements. In addition, they are numerous simple elements grouped together with the name of add-ons, like the spoilers that can be used in both, front or rear of the car; the vortex generators (VG) with several applications; and the gurney flaps added to the trailing edge of the wings. [5]
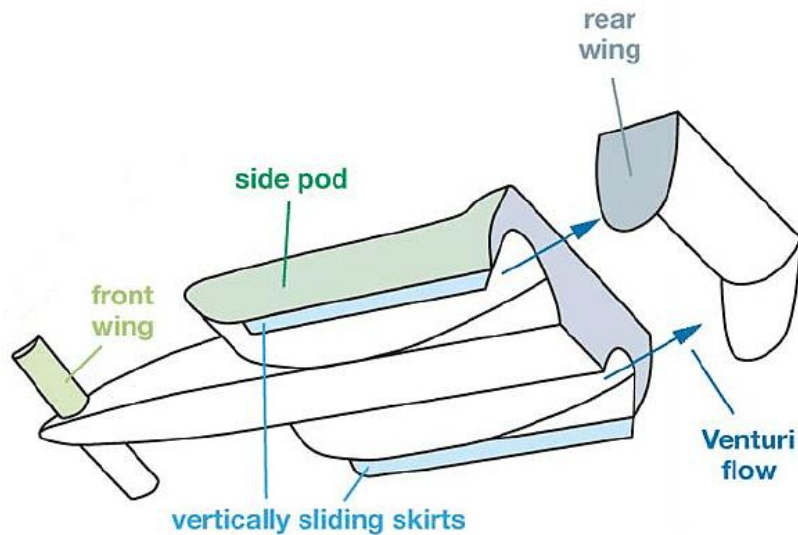
Figure 3. Elements that improve the downforce of a race car

As for the race car wing, they can be found on the front of rear of the car, being very common to have both at the same time. The inverted wings were the first technique for generated downforce, and it is the most obvious approach. Even though the aerodynamic of the wings has been widely studied for aviation, there are three special features on the car wings that must be extensively studied. On the first place, the ground effect has to be taken into account specially in front wings. Secondly, some car wings can have a very small aspect ratio. And thirdly, the interaction car-wing is usually very strong and has to be studied. Studies have demonstrated that the interaction between the wing and the body has positives benefices, obtaining a larger downforce with the coupled configuration than combining the downforce creating by the body and the wing alone. [4]
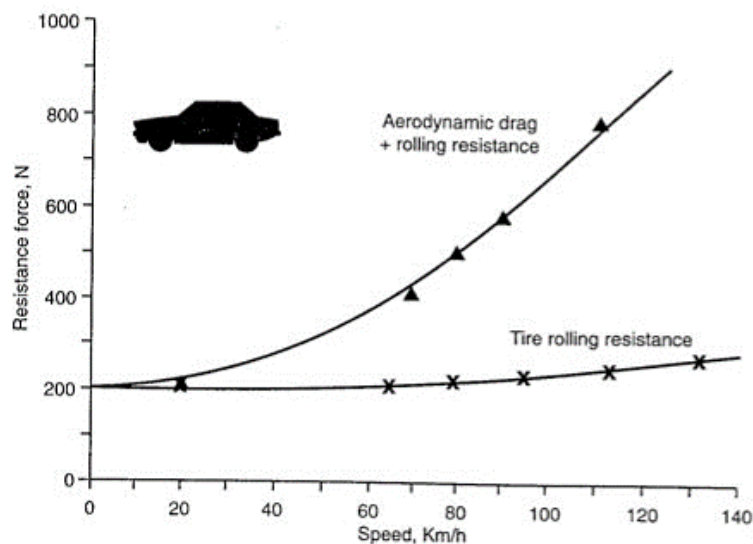
Figure 4. Evolution of tire rolling resistant and drag with the speed [1]

Another important aspect to consider is the drag generated by the wing that comes together with the downforce. Both forces increased rapidly with the speed, so the better approach would be a moveable device to adjust the angle of attack at higher speed. [1]

4

However, regulations normally banned the use of such devices, and therefore a widely study of the operating point is needed, not only to avoid a large drag, but also since the tire performance depends far less on speed. The best operational point could change depending on the circuit characteristics. Finally, especially when only one wing is used, it is important to take into account the balance of the downforce on the tire for the car stability.

1.2.   Problem definition and objectives

Figure 5. Picture of the VW racing car in Fun Cup (credits: LETHION.BE)

This thesis is based on the aerodynamic study of the rear-wing of the Volkswagen Fun Cup racing car (Figure 5). The Fun Cup is a motor racing competition for both professional and amateur pilots, created by Franz Dubois in 1997 in Belgium and organized by Kronos Events. This championship is characterized by its small cost compared with other competitions and by transforming the mythic VW Bettle into a race car. Nowadays the specific car used for this competition is the one called Fun Cup Evo 3. Among the aerodynamic improvements that the car has, the incorporation of a rear-wing is outlined. The competition's regulations allow to install as rear-wing one type of aileron exclusively, which is supplied by WRT. This wing has a span length of 1.35 m and a constant chord length of 0.17 m.
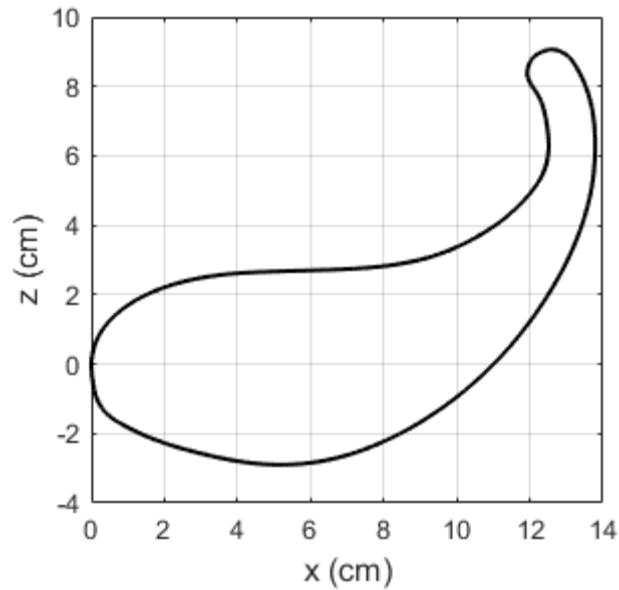
Figure 6. Profile of the studied aileron

This project has as objective to evaluate the aerodynamic properties of this wing for a variety of angles of attack to optimise its performance. Moreover, the Reynolds effect is study, as the velocity of the car on a circuit has a high variation. In order to perform this, a total of three different experiments are carried out on a wind tunnel. Two of them are performed on the wing isolated in which both the 3D forces and the 2D pressure distribution on the profile are obtained. The third experiment, however, is accomplished on a scaled model of the car for studying the flow deflection generated due to its presence upstream of the aileron. Those experiments are complemented by Computational Fluid Dynamics (CFD) simulations on the 2D airfoil for a better understanding of the flow around it.

All the experiments carried out on the wing are performed with the wing isolated in the middle of a uniform flow. Nevertheless, the flow seen by the wing placed at the rear of the car is quite different. So, in order to obtain an approximation of the real performance of the wing on the car, the vertical deflection of the flow measured on the rear part of the car and the 2D results are combined using the Prandtl Lifting Line theory to obtain the 3D aerodynamic forces generated by the wing.

Finally, all these results are analysed so as to find the angle of attack that optimizes the aileron performance. Since the required effect of the wing may change depending on the circuit, three different optimum points are stablished. On the one hand, on circuits with long straight stretches where a high-top speed is required, it is important to keep the drag as low as possible. So, the optimum angle in those circuits is considered to be the one that minimized the drag. On the other hand, there are circuits where the best cornering performance is necessary, so the optimum point is the one with the highest downforce, regardless of the value of the drag. Lastly, on the circuits where both aspects are important, the selected angle is the one that maximize the aileron efficiency, that is, maximize the negative lift-to-drag ratio.

2. Methods

In order to analyse the performance of the aileron at different angles of attacks and different velocities, two different approaches have been used: experimental tests on a wind tunnel and numerical simulations.

2.1.   Wind tunnel tests

All the measurements were performed in the wind tunnel of the University of Liège, located at the campus of Sart-Tilman. This is a low-speed wind tunnel with a modular structure that allows multiple configurations. In order to perform the tests of this work, the configuration stablished has been the closed circuit one and closed test section. The tunnel has two different test sections of different sizes. In this work, all the measurements were carried out in the test section one, called aeronautic/automobile test section, which dimensions are 2 m of width, 1.5 m of height and 5m of length. This section has a boundary layer suction device, to make the airflow more uniform near the ground, a speed range from 2 to 60 m/s for the configuration used and a turbulence level of 0.15%. [6]
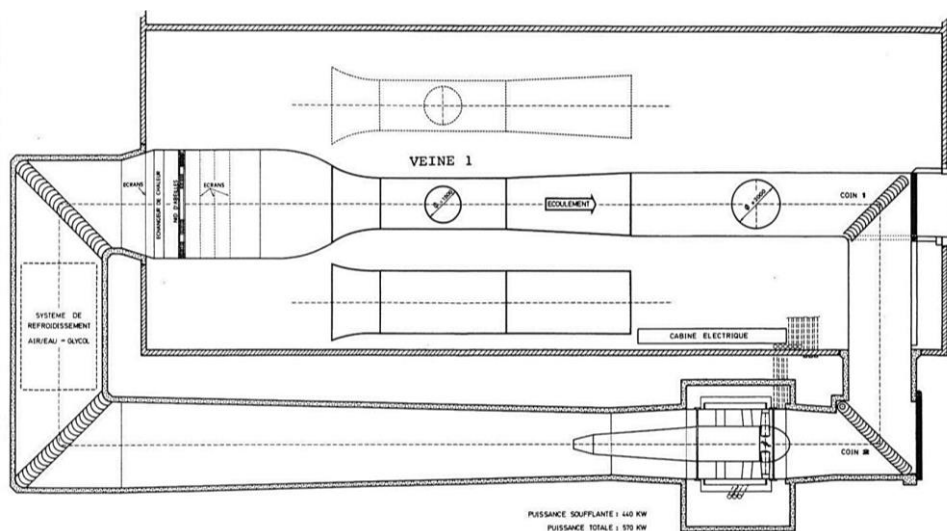
Figure 7. Subsonic wind tunnel of the University of Liège [6]

Three different experiments were carried out. The first one involves an approximate scale model of the car to measure its influence on the airflow noticed by the aileron. In the second one, the forces of the rear-wing were measured for a variety of angles of attack. And the third one consists in a 2D study of the profile of the wing for different angles of attack.

2.1.1.   Deflection of the flow upstream of the aileron generated by the bodywork of the car
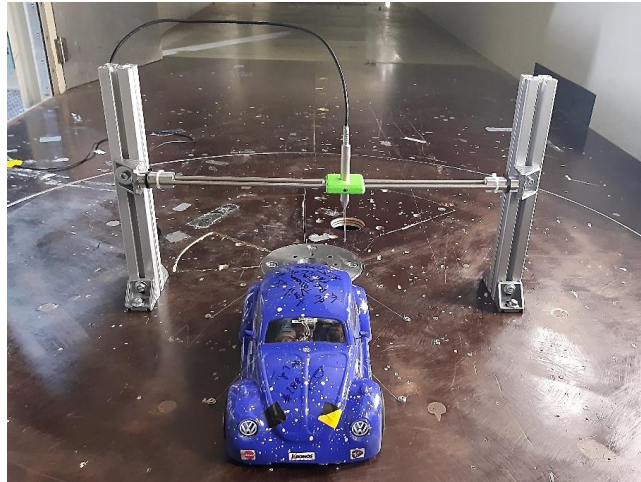
Figure 8. Wind tunnel set-up for the car upstream deflection test performed with a scaled model and the cobra probe

The first experiment was developed on a 1:10 scale car without aileron. The aim of this experiment was to determinate the real direction of the airflow seen by the aileron. In order to do that, the three components of the velocity were measured at the rear part of the car, around the position taken up by the leading-edge of the aileron. The measurements were conducted with a cobra probe. The cobra probe can measure the three components of the velocity in real time thanks to its multiple holes.
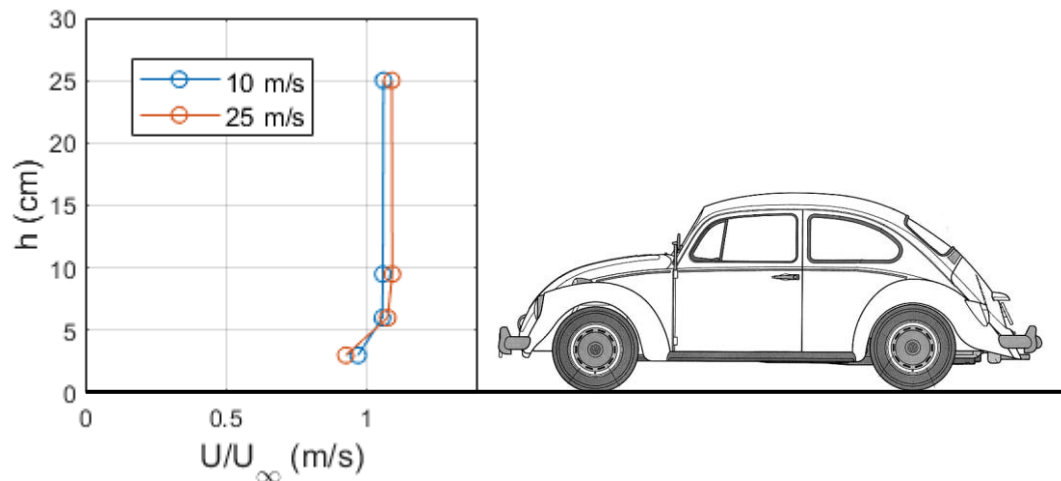
Figure 9. Normalized velocity profile of the flow seen by the front part or the car at $10\ m/s$ and $25\ m/s$.

In order to carry out the experiment, the car was placed on the floor of the wind tunnel. At the back of the car, the cobra probe was mounted on a structure that allows its movement along the span of the car. Before positioning the car and the probe in the mentioned places, the cobra probe was used to characterize the flow seen by the car in order to verify that the measurements were not perturbed by the boundary layer of the tunnel. In order to do this, the velocity was measured at different heights in the position

taken up, later, by the front of the car. A totality of four heights were measured, 3 cm, 6 cm, 9.5 cm and 25 cm, for two different velocities, 10 m/s and 25 m/s. The results of this tests can be observed on Figure 9, where a scheme of the lateral view of the car at the same scale is shown. The velocity profile is stabilized at the height of the front of the car, so the measurements are not affected by the presence of the ground.

After verifying that the profile of the velocity was correct, the car and the probe were placed on their correspondent positions. In order to correctly place the probe in both, vertically and longitudinally, a scale model of the aileron and its frame was used. Placing both in the car at the correspondent original position, the location of the leading-edge of the wing was measured. Its height was measured taking as reference the floor and its longitudinal position, with respect to the rear of the hood of the car. Once the structure that holds the probe was correctly placed at the back of the car, the probe was placed on it facing the free stream velocity. The structure consists of two vertical bars that holds two parallel rails, placed horizontally, where the support of the probe is placed. The rails allow the spanwise movement of the probe. Using the rails to move the probe along the span of the car, the velocity was measured at 11 different positions for 4 different free stream velocities: 10, 15, 20 and 25 m/s.

2.1.2.   3D force measurements of the aileron

Figure 10. Wind tunnel force test set-up

The second experiment was carried out again on a full-scale wing mounted on the same frame used in the race car. As the aim of the experiment was evaluating the aerodynamic forces of the wing for different angles of attack, the aileron with its support was situated on a hinge that allows to modify the angle of attack by steps of 5° approximately. This hinge was placed, in turn, on a force sensor OMEGA160 by ATI that measures the forces and moments on three perpendicular axes at 200 Hz. This set up, that can be observed on Figure 10, has a maximum blockage in the test section of 8%. The tests were done for 10 angles of attack between $-45°$ and 0° at a free stream velocity of $30\,m/s$. Furthermore, at $\alpha = -31.3°$ two additional tests are performed at the free stream velocities of $10\,m/s$ and $20\,m/s$, respectively, in order to analyse the Reynolds effect. Each angle of attack has been measured as the angle between the direction of

the flow and the tangent line to the aileron in the upper side. On Figure 11, this is illustrated, with a schematic representation of the profile of the wing on the original position that corresponds with $\alpha = -30.5°$.
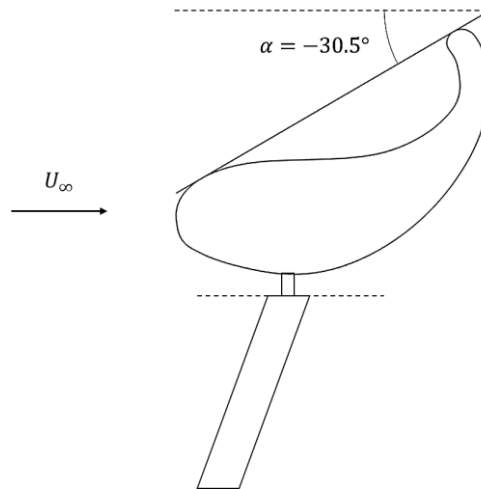
Figure 11. Schematic representation of the original position of the aileron

Before conducting the tests, the sensor must be calibrated. This calibration is carried out by the addition of known masses in different locations. The aim of this calibration is to determine the parasitic horizontal force that appears when the masses are located out of the mass centre of the sensor. This parasitic force is proportional to the moment that causes it and, hence, it is easy to determine. The parasitic force can appear in both x and y axes, but as the assembly is symmetric about the x-axis, the momentum along the x-axis is null and therefore, there is no parasitic force along the y-axis. So, the calibration is done only along the x-axis, relating the momentum along the y-axis with the parasitic force along the x-axis through the constant k:

$$F_{x_{parasitic}} = k \cdot M_y \tag{1}$$

After measuring the parasitic force for four different values of momentum, the result obtained with the calibration is $k = 0.442$.
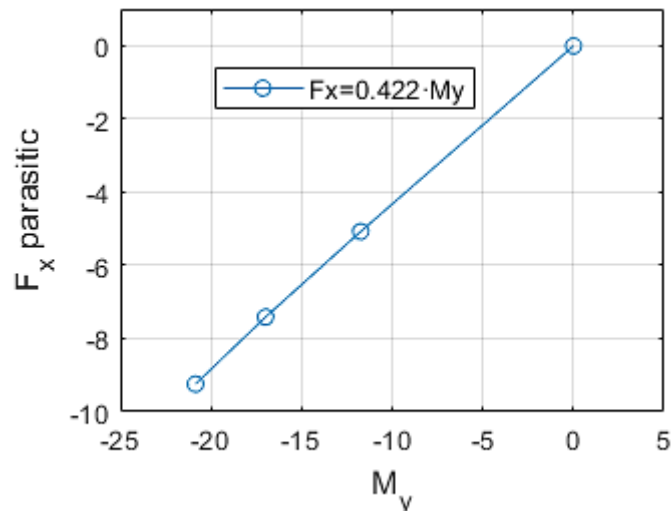
Figure 12. Result of the calibration of the parasitic x-axis as a function of the applied y-axis momentum.

In addition, as the sensor measures the aerodynamic force of all the structure that comprises the frame, it is necessary to determine the aerodynamic forces of the frame isolated, in order to subtract this value.

2.1.3.   2D pressure measurements of the aileron

Figure 13. Wind tunnel pressure test set-up. Detail of the pressure tubes exit
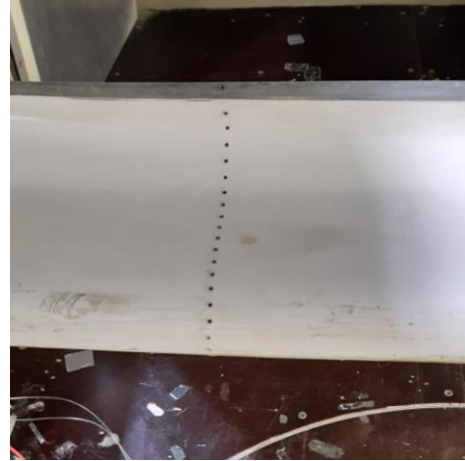
Figure 14. Detail of the pressure taps.

The third experiment was done using the same assembly that in the second one. The aim of the experiment was to obtain the pressure distribution over the 2D profile for a variety of angles of attack and velocities. A total of eleven different angles of attack were evaluated between $-50°$ and $0°$ for three free stream velocities: 20, 30 and 40 m/s.
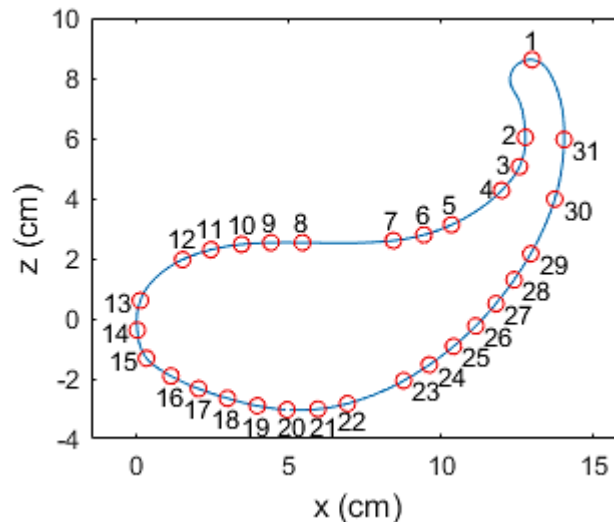
Figure 15. Location of the pressure taps on the profile of the aileron ($\alpha = -30.5°$)

The pressure was measured with 31 pressure tubes distributed along a 2D profile of the wing (Figure 15). These tubes are connected to two Dynamic Pressure Measurement System that measure the different between the pressure of each tap and a reference pressure, that is, the dynamic pressure. Each of them contains 16 pressure ports for pressure taps and an additional port for the reference pressure. Regarding the situation

of the profile where the measurements were done, as it was impossible to perform the measurement in the profile situated in the middle of the span due to the hole used for the evacuation of all the tubes is situated at this right position and due to the effect of the frame on this zone, the measurements were done in the profile located on the right side of the wing at $y = 40 \, cm$.

2.2. CFD model

Apart from the three experiments performed on the wind tunnel, some Computational Fluid Dynamics (CFD) simulations are performed on the 2-dimensional profile of the wing. These simulations are performed at a totally of 6 different angles of attack taking the angle of $\alpha = -30.5°$ as the reference angle, where a Reynolds effect study is performed too.

The simulations carried out in the work were performed using ANSYS Fluent 19.0. A turbulent flow, as the one that exists around the studied aileron, is a high three-dimensional and non-stationary flow that involves a wide range of length scales, from big eddies of size of the same order of magnitude than the characteristic length to the Kolmogorov microscale, which is the responsible of the energy dissipation. So, in order to accurately determine the flow, all the scales have to be resolved. Carrying this out solving the Navier-Stokes equations, known as direct numerical simulation, is computationally extremely expensive and completely unpractical. For this reason, there are two alternatives that allow not to solve all the scales, but to model some of them. These two approaches are the Reynolds Averaged Navier-Stokes (RANS) or Unsteady Averaged Navier-Stokes (URANS) equations and the Large Eddy Simulation (LES). [7]

The LES model is intermediate in terms of computational cost. It is based on filtering the Navier-Stokes equations in order to remove the smallest scales, responsible for much of the computational cost, that are modelled. [7] The fastest method are the RANS and URANS models and are the ones used in this work. [8] As the profile is thick and has an extreme curvature near the trailing edge, its behaviour is expected to be like the one of a bluff body and vortices are expected. Due to this, the unsteady behaviour is essential, and the Unsteady RANS equations are used.

In the RANS and URANS models all the spatial scales are modelled while only the equations averaged are solved. [8] It is based on the Reynolds decomposition in which each instantaneous quantity, as the velocity u, is separated into its time-averaged value, $U = \bar{u}$ and its fluctuation, u': $u(x,t) = U(x,t) + u'(x,t)$. Applying this decomposition to the Navier-Stokes equations and averaging them, we obtain the URANS equations, that for incompressible flows are: [9]

$$\frac{\partial U_i}{\partial t} = 0 \tag{2}$$

$$\rho \frac{\partial U_i}{\partial t} + \rho U_j \frac{\partial U_i}{\partial x_j} = -\frac{\partial p}{\partial x_i} + \frac{\partial}{\partial x_j}\left(\mu \frac{\partial U_i}{\partial x_j} - \rho \overline{u_i' u_j'}\right) \tag{3}$$

In the momentum equations a new term appears, $\rho\overline{u_i'u_j'}$, called Reynolds stress. [9] This term adds six unknowns to the problem, so a turbulence model is needed as a closure. There are two different methods for modelling the turbulence: the Boussinesq approach and the Reynold Stress Transport Models (RSM). In the Boussinesq approach, the Reynolds stress term is related to the mean flow introducing the eddy viscosity or turbulent viscosity, μ_t: [10]

$$-\rho\overline{u_i'u_j'} = \mu_t\left(\frac{\partial u_i}{\partial x_j} + \frac{\partial u_j}{\partial x_i}\right) - \frac{2}{3}\left(\rho k + \mu_t\frac{\partial u_k}{\partial x_k}\right)\delta_{ij} \tag{4}$$

Different models apply the Boussinesq hypothesis introducing one or more equations to determine the turbulent viscosity and, in some cases, the turbulent kinetic energy and dissipation. In the RSM model each component of the Reynolds stress tensor is directly computed with transport equations, together with an equation for the dissipation rate, ϵ. This method is more elaborate, and could be more accurate than the Boussinesq approach, but is also more computational expensive. The use of an RSM model is normally relegated to those cases where the anisotropy of turbulence is important as the Boussinesq approach assumes that μ_t is isotropic. [10] In this project two different turbulence models based on the Boussinesq hypothesis have been used:

- SST $k - \omega$ [11]

The Shear-Stress Transport (SST) $k - \omega$ model, developed by Menter, is a variation from the Standard $k - \omega$ eddy viscosity model that combines this model and the high Reynolds version of the $k - \epsilon$ model, and modify the eddy viscosity formulation to account the transport effects of the principal turbulent shear stress.

The $k - \omega$ model is an empirical model that predicts the local turbulence by the differential equations for the turbulence kinetic energy, k, and the specific rate of dissipation, ω. The standard $k - \omega$ model is based on the Wilcox $k - \omega$ model and is considered by many authors as superior to the alternative two-equation models in the sublayer of the boundary layer, due to its simplicity and the high accuracy predicting the mean flow. In addition, its behaviour in the logarithmic part of the boundary layer is considered better that the one of the $k - \epsilon$ model. In spite of this high performance in the inner region of the boundary layer, this model has associated some deficiencies such as its strong sensitivity to the free stream conditions and a lack of accuracy in the prediction of the flow separation for strong adverse pressure gradients. [12]

In order to avoid the free stream dependency, the $k - \epsilon$ model, transformed into $k - \omega$ formulation, is applied far away from the surface, while the $k - \omega$ model is used in the inner region of the boundary layer. A gradual change between both methods is got thanks to a blending function. The $k - \epsilon$ model was the first two-equation model used in CFD and it is a semi-empirical model based on model transport equations for the turbulence kinetic energy and the rate of dissipation of the turbulence kinetic energy, ϵ. This combination leads to the $k - \omega$ baseline (BSL) model. In addition, to improve the behaviour for strong pressure gradients, in the SST $k - \omega$ model the turbulent viscosity formulation is modified to account for the transport effects of the principal turbulent shear stress and the modelling constants are changed. [13]

- $\gamma - Re$ Transition [14]

The SST $k - \omega$ model processes the fluid as turbulent throughout the domain. This implies that this model is unable to predict the laminar to turbulent transition and, therefore, can carry out errors in the computation of the aerodynamic forces on the airfoil and in the phenomenon of separation of the flow. So, the transition model $\gamma - Re$ has been used. This transition model coupled the transport equations of the SST $k - \omega$ model with two additional transport equations for the intermittency, γ, and for the transition momentum thickness Reynolds number, $\widetilde{Re_{\theta t}}$, respectively. An empirical correlation developed by Langtry and Menter is used in ANSYS Fluent for this model.
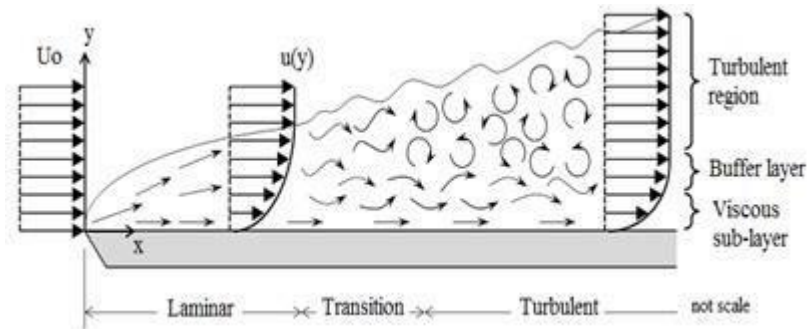
Figure 16. Scheme of the laminar-turbulent transition

Once the model is determined, the type of solver used must be stablished. Fluent features two different numerical approaches for solving the equations, the pressure-based solver and the density-based solver. On this work, the pressure-based solver has been selected, as all the simulations are done for incompressible flows. In this solver, in addition to the momentum equation, a pressure equation derived from both the continuity equation and the momentum equation is solved as for the mass conservation constrain. [15]

Regarding the algorithm used for solving these two equations, there are two different types: a coupled algorithm and segregated algorithms. In this work, the coupled one is selected. This method solves the system formed by the pressure-based continuity equation and the momentum equation jointly instead of sequentially as it occurs in the segregated algorithms. This leads to a higher requirement regarding the memory but improves the convergence. [15] [16]

2.2.1.   Mesh and boundary conditions

The study domain is limited externally by a rectangle, big enough not to influence on the flow seen by the airfoil, and internally by the profile. This domain has been divided into different sections in order to be able to control the mesh and in order to get a structured mesh in all the domain (Figure 17). The mesh is defined by controlling the number of divisions of each edge, that make up the subdomains, and its bias. With this approach, it is possible to get a more refined mesh in the areas of interest, the proximities of the profile, keeping a lower refinement in the farthest zones. Since this mesh is used

for simulations with different angles of attack of the flow, it is important that the mesh in the proximities of the profile is small enough in all the directions and having a low aspect ratio, except in the boundary layer, in order to get a similar accuracy for the different angles.
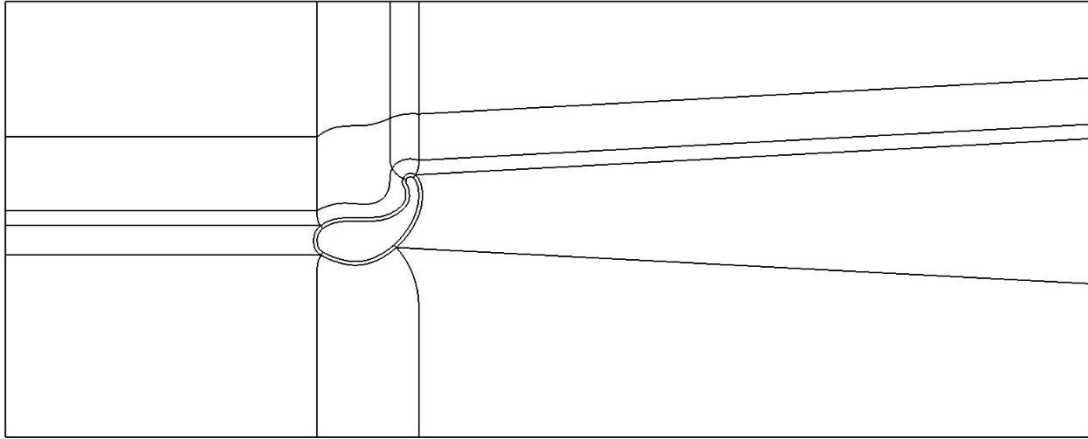
Figure 17. Partitions of the computational fluid domain

In terms of the boundary conditions applied, they depend on the angle of attack studied and they can be divided into three different configurations. In all the cases, the treatment of the airfoil is the same. The difference lies in the type of condition applied in the different sides of the external rectangle, more specifically, in the upper and lower edge conditions. The mesh has been made with the profile located at an angle of $-30.5°$ to the horizontal axis. For this angle of attack, considered as the reference angle, the velocity of the free stream only has horizontal component, so the upper and lower sides are defined as a wall, while the left edge is set as inlet and the right edge as outlet. For the positive angles with respect to the reference angle, the lower edge joins the left side to form the inlet and the upper side forms the outlet with the right one. For negative angles, the opposite happens; the upper edge becomes part of the inlet and the lower one is set as outlet. These configurations can be seen on the Figure 18.
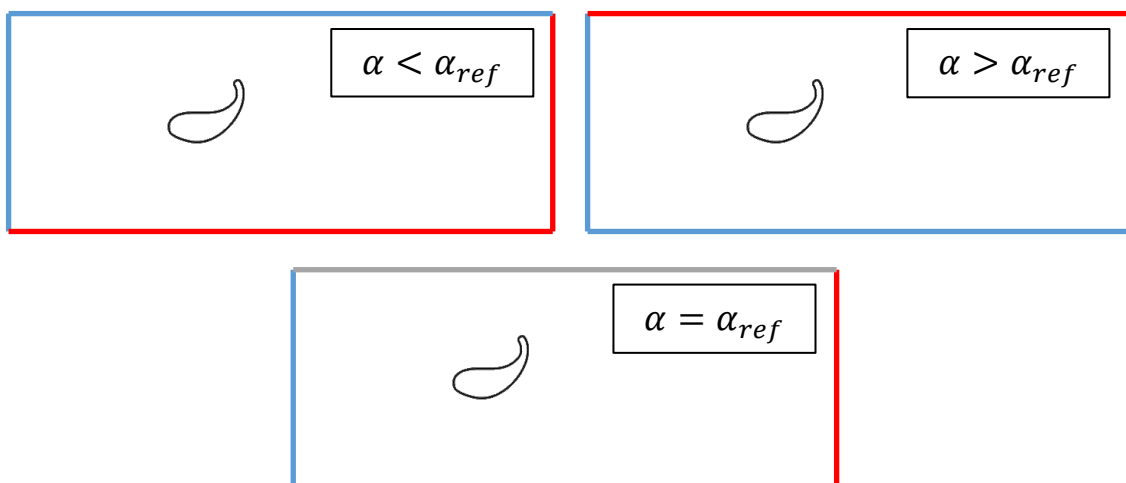
Figure 18. Types of boundary conditions depending on the angle of attack with respect to the reference one. Scale of colours: Black - Airfoil; Grey - Wall; Blue - Inlet; Red - Outlet

In all of them the conditions applied to each type of boundary are similar:

- Airfoil

The airfoil is defined as a stationary wall with a no-slip condition. This condition implies that the velocity of the flow in the wall has to be zero and therefore a boundary layer is developed which implies the need of a fine mesh around the profile for a correct model of it. In order to quantify the needed refinement, the y+ parameter is used. The y+ is an non-dimensional quantity which identifies the height of the first grid from the wall, using the height of its centroid, and it is defined as $y^+ = \frac{yu_*}{\nu}$, where u_* is the friction velocity, defined as $u_* = \sqrt{\tau_f/\rho}$. With this parameter, it is possible to identify in which layer of the boundary layer the first cell is placed.
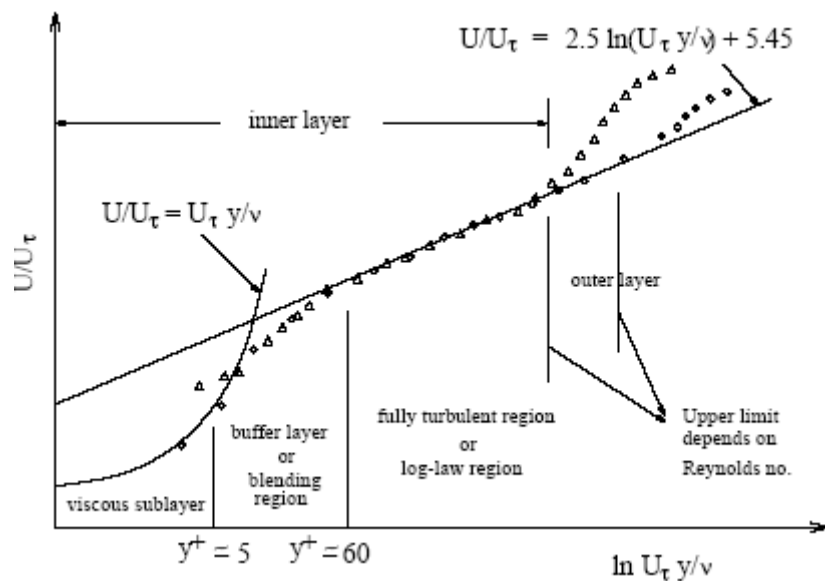
Figure 19. Scheme of the sublayers of the boundary layer [17]

The turbulent boundary layer is formed by three different sublayers. The inner layer, known as the viscous sublayer, where the viscous effects are dominant and the flow is almost laminar. The outer layer, or log-law region, where the turbulence is the dominant. And the interim region, called buffer layer, where both viscous and turbulent effects are important. [17] The subdivision of the boundary layer as a function of the y+ can be observed on Figure 19 .

The treatment of the boundary layer depends on the turbulence model applied and the accuracy required in the ongoing case. This treatment can be done in two different ways. In the first one, called wall functions or high Reynolds approach, the viscous sublayer is not resolved, and wall functions are used as a bridge between the wall conditions and the logarithmic layer. [17] For using this method, the y+ must be found in the log-layer, so $30 < y^+ < 300$. With the second approach known as low-Reynolds, all the boundary layer is resolved, so the value of the y+ must be of the order of $y \approx 1$ to be in the viscous sublayer (it is normally accepted for being in the viscous sublayer values of $y^+ < 5$). [17]

- Inlet [18]

For the inlet the Velocity Inlet Boundary Condition is used, in which the inlet velocity is specified and the stagnation pressure will be stabilized by the program to provide this velocity distribution. In order to obtain a uniform stagnation pressure, it is necessary to have this condition far enough from the airfoil. The velocity is specified by its magnitude and its direction. In addition, some turbulent parameters have to be set. There are several ways for defining the turbulence characteristics. The ones used in this project has been the turbulence intensity, I, define as $I = \frac{\sqrt{u'u'}}{U}$, and the turbulent viscosity ratio, μ_t/μ, for the SST $k - \omega$ model; and for the $\gamma - Re$ transition, the intermittency in addition with these two parameters.

The values selected for the turbulence characteristic used in all of the simulations done with the aileron on this work are: $I = 0.15\%$, $\mu_t/\mu = 1$ and $\gamma = 1$. The level of turbulence intensity used is the same that the one of the wind tunnel. Regarding the viscosity ratio and the intermittency, the same values as in similar studies are used. In addition, those studies determined that they influence on the final solution is almost negligible.

- Outlet [19]

For the outlet the Pressure Outlet Boundary Condition is employed. With this condition, the Gauge Pressure has to be specified and has been stablished in 0 (Pa). It is important, as in the inlet, to have this side far from the interest area in order not to influence the flow of this area. Also, the same turbulent parameters as in the inlet must be stipulated.

- Wall

In the simulations done for the reference angle of attack, the Wall Boundary Condition has been used. In contrast with the airfoil boundary, a slip condition with a null shear stress is utilized, in order to minimize its influence on the flow. This condition means that the flow will not cross these edges and, as both the upper and lower sides are horizontal, that the flow will be horizontal on them. As with the inlet and outlet this sides must be placed far enough from the profile. [16]

2.2.2.   Convergence study

In this section a convergence study is performed on the computational domain. This study is important as badly limits of the domain can induce into important errors on the simulations. To avoid this, it is important that the external boundary conditions are far enough from the region of interest, that is, from the airfoil. But the bigger the domain is, the higher the number of cells is too, and therefore, the computational demand increases quickly. So, a compromise is needed where the domain is big enough not to have an importance interference with the solution but with a reasonable computational cost.

The converge study is performed with the SST $k - \omega$ turbulent model and only on the reference angle ($\alpha = -30.5°$) and at $40 \, m/s$ that corresponds to $Re = 4.66 \cdot 10^5$. The

reason of choosing the highest velocity is because it is the one that need a biggest domain not to influence the flow on the airfoil. After performing the convergence study on this reference angles, some geometric considerations will be made to ensure that the domain is big enough for all the studied angles of attack. This procedure manages to avoid the need to do the study for all the angles. In contrast, the accuracy is lower as it is assumed that the boundary conditions affect in the same way to all of the angles. This is not completely true as some differences on the behaviour flow, especially on the wake, may exist, but is very precise.

On a domain convergence study, there are two important things that must be taken into account. First of all, it is important that the blockage ratio remains below a limit, that is normally imposed to be 4% or 5%. If the blockage is too high, the flow will artificially accelerate due to continuity. On the second place, it is important that the boundary conditions in general, that includes inlet, outlet and wall conditions, are far enough in order to not to disturb the flow. Within this last condition, it is important to treat each of the boundary conditions differently.

For the wall a determined minimum distance is necessary as the direction of the flow is determined in this condition and near enough it can prevent the flow curving to pass the obstacle. But this distance is normally accomplished more than enough when the maximum blockage ratio is respected and the domain is symmetric, as it is the case here. So, the wall distance to the profile is determined in this study exclusively considering the blockage ratio.

For the inlet condition the needed distance is not too big again. The direction of the flow on the inlet is imposed as for the wall condition and, furthermore, the velocity is stablished with the flow uniform. But the influence of this condition is avoided with a relatively not too big distance as happened with the wall conditions.

This does not happen with the outlet, that is going to be the most restricted boundary. On the outlet a fixed pressure is stablished, so it is easy to think that a similar distance as the ones for the other boundaries should be enough. The problem remains in the fact that this pressure could affect the wake of the aileron in areas of the domain away from the airfoil. As the wake is an essential part of the flow, and any modification on it could lead on perturbations upstream that end up affecting the flow around the airfoil, the outlet distance should be far enough to permit that all the wake is developed correctly.

So, basing on these considerations, the convergence study is performed varying only the longitudinal size of the domain. The lateral size of the domain is determined to satisfy the limit on the blockage ratio. As the height of the aileron is almost $12\,cm$, the total lateral size of the domain is stablished on $300\,cm$, with both boundaries at the same distance from the airfoil. As for the longitudinal length, based on other studies on bluff bodies, as a 2D cylinder, the distance between the outlet and the airfoil is imposed as twice the distance between the inlet and the airfoil.

Three different domain lengths have been studied, $30d$, $50d$ and $75d$, where $d = 0.15$ is the longitudinal measure at $\alpha = -30.5°$. Each of the domain lengths have been distributed with $L/3$ distance from inlet and $2L/3$ from outlet. The results obtained of the lift and drag coefficient on the three cases are shown on Figure 20 and Figure 21. It can be observed how both the negative lift coefficient and the drag coefficient decreases

when the length of the domain increases. Both the lift and the drag coefficient obtained for a total length of $50d$ and $70d$ are practically the same with a difference of the order of 0.001. So, the solution can be consider converged from the second domain of $50d$.
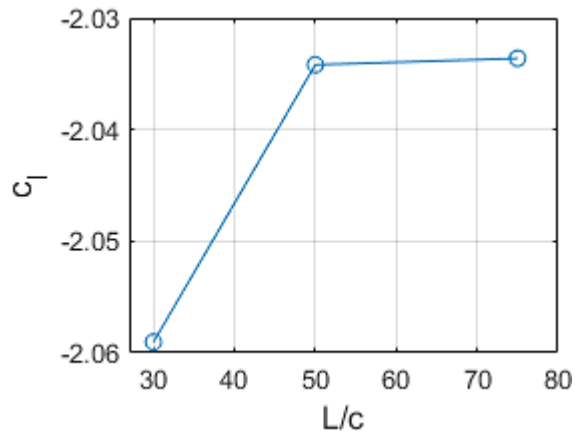
Figure 20. Lift coefficient of the domain convergence study.
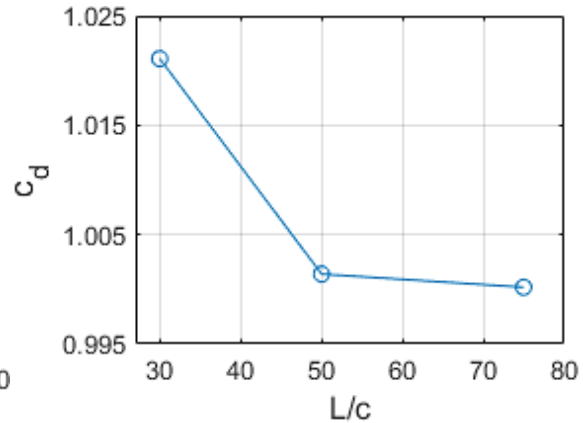
Figure 21. Drag coefficient of the domain convergence study.

Furthermore, on Table 1 it can be observed the time needed to make 1 time-step of 50 iterations with each of the domains.

Table 1. Computational time per time-step of 50 iterations with each domain of the convergence study

Length of the domain	Time (s)
$30d$	33
$50d$	41
$75d$	67

So, the better domain that has a compromise between the precision and the computational cost is the one of $50d$. Now, it has to be checked if with this domain the distance to the outlet is preserved for the rest of the angles of attack. Taking into account that the distance from the airfoil and the lateral surface is of $150\ cm$ and the distance to the outlet in this domain is of $500\ cm$, the maximum angle at which the distance of the outlet is preserve is $17.5°$. This would cover all the simulations excepting the one performed at $\alpha = -10.5°$ that would have a distance to the outlet of $438.5\ cm$. This deviation is considered small enough, so this domain is selected as the final one.

In addition to this study, a similar convergence study for the number of cells has been performed. Selecting as final mesh one with $1.5 \cdot 10^5$ cells.

3. Wind tunnel results

On this chapter the results of both the numerical simulations and the wind tunnel are presented and compared. First of all, the results of the three experiments performed on the wind tunnel are exposed: beginning with the pressure measurements on a 2-dimensional profile, continuing with the effect of the car on the flow seen by the aileron and ending with the study of the 3-dimensional wing. For this last study, as well as the results from the force experiment of the wind tunnel, the 2-dimensional performance of the aileron and the deflection of the flow induced by the car is studied together with the Prandtl lifting line theory to estimate the 3-dimensional forces. This study allows not only to study the performance of the aileron on the car, but also to correct the results obtained from the pressure experiment on the wind tunnel to obtain real 2-dimensional data.

Once the 2D data of the wind tunnel experiment are corrected, they are compared to the numerical results from the simulations.

3.1.   2. D profile

As it was explained before on the methodology chapter, the 2-dimensional experiment is performed based on pressure measurements around one profile place at $y = 40\ cm$. Since it is usual on aerodynamics, non-dimensional coefficients are used. Therefore, with the pressure measurements the pressure coefficient is obtained:

$$c_p = \frac{p - p_\infty}{\frac{1}{2}\rho U_\infty^2}$$

(5)

Once having the pressure coefficient along the profile, the 2-dimensional lift coefficient and the drag coefficient can be obtained integrating the pressure coefficient along the surface:

$$c_l = \frac{1}{c} \oint c_p n_y ds$$

(6)

$$c_d = -\frac{1}{c} \oint c_p n_x ds$$

(7)

Where n_x and n_y are the x-component and y-component, respectively, of the normal vector of the surface in each point. As the number of points where the pressure is known is finite, the integral is transformed into a sum. It is important to remark that for the drag, only the form drag or pressure drag is obtained. To obtain the total profile drag, it would be necessary to measure the skin friction drag on the wind tunnel, which is out of the

scope of this work. However, as the wing is not very streamlined, the dominant term of the profile drag is expected to be the form drag, so from now in this section it would be called as drag without any distinction.

Once the lift and drag coefficients are obtained for each α and each free stream velocity, the Reynolds effect can be studied. As the effect of the velocity varies according to the specific angle of attack, this study is done by comparing the evolution of the lift and the drag with α for the three free stream velocities tested. This is shown on Figure 22 for the lift coefficient and Figure 23 for the drag coefficient. It is important to remark that on Figure 22 the vertical axis correspond to $-c_l$ as we are interest on the negative lift. When talking about this coefficient, the forms 'negative lift coefficient' and 'downforce coefficient' are used indistinctly.
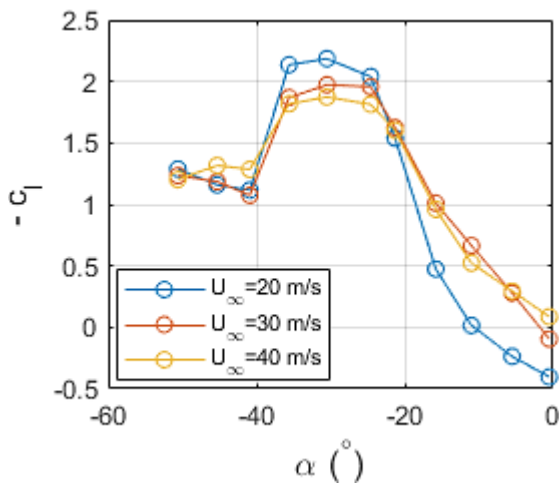
Figure 22. Variation of the 2-dimensional negative lift coefficient with the angle of attack obtained with wind tunnel pressure experiment for different velocities. Reynolds effect.
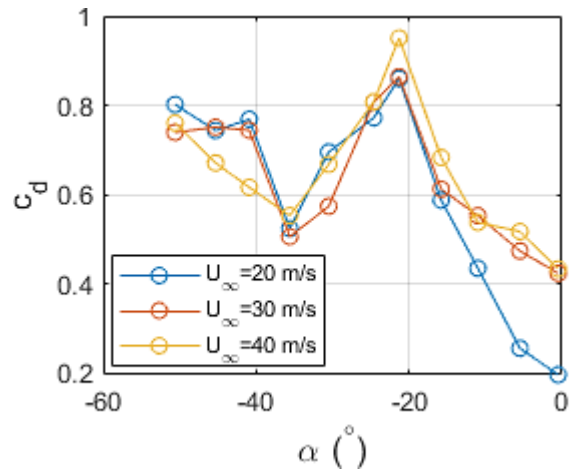
Figure 23. Variation of the 2-dimensional drag coefficient with the angle of attack obtained with wind tunnel pressure experiment for different velocities. Reynolds effect.

In both graphics it is observed that the shape of the curves is similar for the three velocities, but some differences appear. For the right part of the graphics, that corresponds to the angles of attack closest to $\alpha = 0°$ the curves for $U_\infty = 30 \, m/s$ and $U_\infty = 40 \, m/s$ are almost the same, whereas for $U_\infty = 20 \, m/s$ both downforce and drag are lower. This tendency changes for the lift when the zone of the maximum is reached, that is $\alpha \in [-35.6, -24.6]$, as in this range the lower the velocity is, the higher the downforce is. For the drag, in this range there is not a clear tendency. Finally for the left part of the graphics the results for $U_\infty = 20 \, m/s$ and $U_\infty = 30 \, m/s$ are similar, and now, it is the highest velocity the one that differs a little with a higher downforce and a lower drag.

From now on, as the Reynolds effect has already been analysed, the study is continued using the results obtained with the free stream velocity of $30 \, m/s$. For analysing the effect of the angle of attack, Figure 23 is used again for the drag, now paying attention only to the red curve. For analysing the downforce coefficient, the Figure 24, where the measured lift is accompanied with the result of the thin airfoil theory $c_l = 2\pi\alpha$, is used.
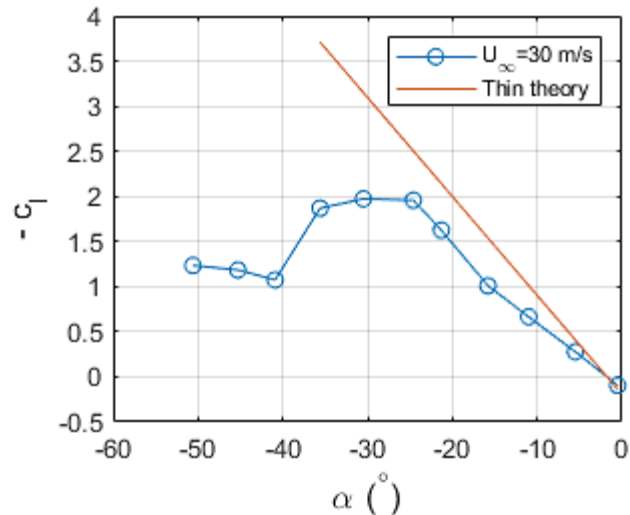
Figure 24. Variation of the 2-dimensional negative lift coefficient with the angle of attack obtained with wind tunnel pressure experiment for $U_\infty = 30\ m/s$. Comparison with the thin airfoil theory.

Regarding the negative lift and starting from $\alpha = 0.5°$ where the lift is almost zero, the downforce increases as the angle of attack decreases with an almost constant rate up to $\alpha = -24.6°$. Comparing this slope to the one of the thin airfoil theory, it can be observed that the one of the studied wing is a little lower (1.56π instead of 2π), but they do not differ excessively, even though it is not a really thin airfoil. After this point the downforce remains almost constant for $\alpha = -30.5°$ and decreases a little for $\alpha = -35.5°$ with less than 0.1 of difference. At $\alpha = -40.9°$ the downforce drops to almost $-c_l = 1$, rising a little after that but with values far from the ones of the maximums.

As for the drag, what looks like a zigzag pattern is observed. Beginning again on the right, the drag rises up to $\alpha = -21.3°$ where the maximum of $c_d = 0.95$ is found. Then decrease up to $\alpha = -35.5°$ with $c_d = 0.55$ and rises again to a value of 0.75 remaining almost constant for the last three angles.

On Figure 25 the ratio of downforce coefficient to drag coefficient, or what it is the same ratio of downforce to drag, is shown. The maximum ratio is located at $\alpha = -35.5°$ with a value of 3.7. Another good value of the ratio is found at $\alpha = -30.5°$ where $-c_l/c_d = 3.4$. For the rest of the angles of attack, the ratio is considerably lower with values around 2 and 1.5 at most.
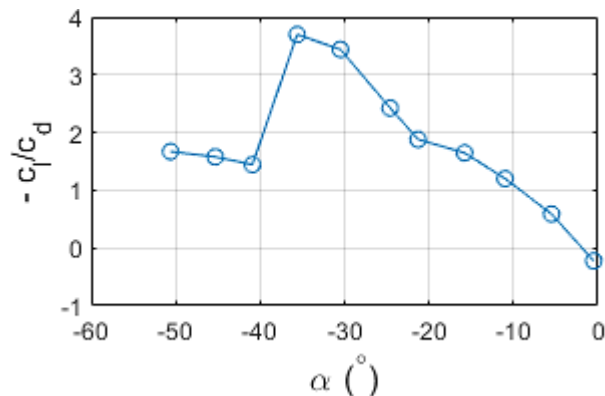
Figure 25. Variation of the ratio of the 2D negative lift to drag coefficients with the angle of attack obtained with wind tunnel pressure experiment for $U_\infty = 30\ m/s$.

After this, it can be concluded that the angle of attack with the better 2D performance is $\alpha = -35.5°$ as it has not only the highest ratio of downforce to drag, but also the lowest drag excluding the two highest angles of attack in which the lift is almost zero. It can be also interesting $\alpha = -30.5°$ as the lift coefficient is a little bit higher, even though the drag is a bit higher and the ratio is lower than the previous one.

Once determined the angles of attack of interest, the pressure distribution of these angles is studied. Both pressure coefficients are shown on Figure 26 where the suction side corresponds to the lower one and the pressure side is the upper one, as the aileron is an inverted wing. Regarding Figure 15 (where the profile is plot at $\alpha = -32.8°$) the limits between the lower side and the upper side are stablished on the pressure taps 1 and 14. The pressure coefficient for both angles is very similar with a practically equal pressure side. The biggest difference is at the mid part of the lower side (suction side) where the pressure for $\alpha = -30.5°$ is a little lower than for $\alpha = -35.5°$.
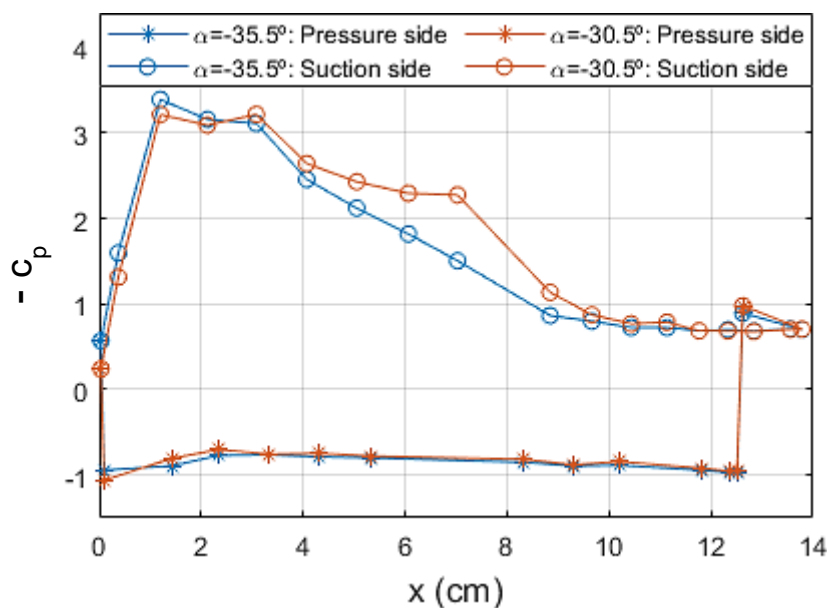
Figure 26. 2-dimensional pressure coefficient distribution for $\alpha = -30.5°$ and $\alpha = -35.5°$ for a free stream velocity of $30\ m/s$.

Up to now, all the results presented are the mean value of the correspondent variable. But, as the flow is unsteady, it is important to consider too the fluctuation of the results. In order to study it, the standard deviation of the pressure coefficient is used. To represent the standard deviation, σ, the value of each tab is represented with a circle place on the correspondent position on the profile, in order to ease its analysis. Where the size of the circle symbolises the magnitude of σ. Moreover, the same representation is used with the mean value of the pressure coefficient to complement the previous representation as a function of x and helping in the understanding of the flow behaviour. As the pressure coefficient can be both negative or positive, two colours are used: blue for the positive values and red for the negative ones.

On Figure 27 and Figure 28 it can be observed, respectively, the mean value and the standard deviation of the pressure coefficient at $\alpha = -30.5°$. Regarding the upper surface (pressure side), it can be observed how after the stagnation point (tap number 13), where the pressure coefficient is 1, the pressure decrease a little for the first two taps and then remains almost constant with a slightly rise up to the tap number 2, where

the pressure coefficient reach again a value of 1. This means that the velocity in almost all the pressure side is very low. As for the standard deviation, it has an almost constant value except for a peak on the tap number 10. After the tap 2, the pressure decreases quickly and σ strongly decrease. This seems to indicate the separation of the flow due to the bluff geometry near the leading edge.

With regard to the lower side, after the stagnation point the flow suffers a strong favourable gradient pressure, that is, a strong decrease of the pressure coefficient up to the tap number 16. Then, the pressure remains almost constant for the next two tabs and, after that, slightly decreases up to the tap 22. After that, the pressure coefficient decreases rapidly and remains almost constant for the until the last tap. As for σ, it increases up to the maximum located on the taps 22 and 23, and after that decreases again. This behaviour corresponds with the flow being separated for around the mid of the chord.
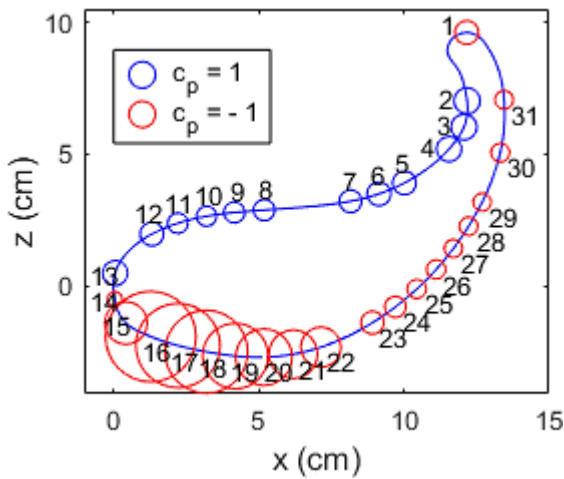
Figure 27. Mean pressure coefficient obtained from pressure experiment on the wind tunnel at $\alpha = -30.5°$ for a free stream velocity of $30\ m/s$.
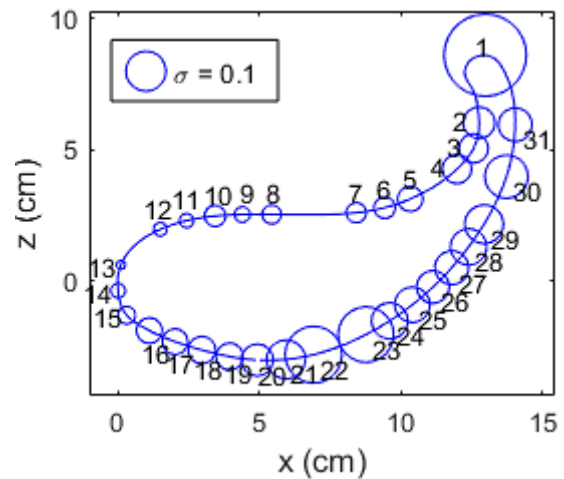
Figure 28. Mean pressure coefficient obtained from pressure experiment on the wind tunnel at $\alpha = -30.5°$ for a free stream velocity of $30\ m/s$.
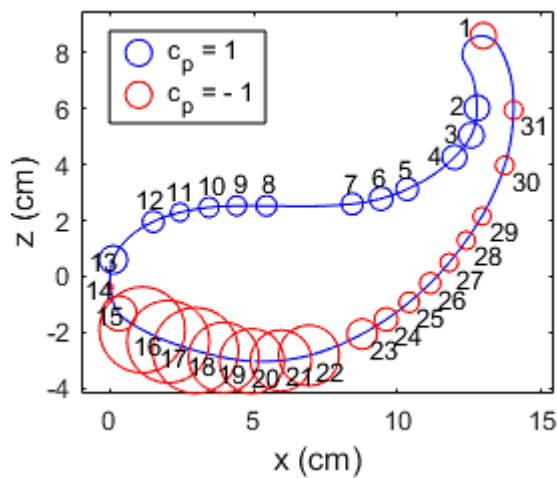
Figure 29. Mean pressure coefficient obtained from pressure experiment on the wind tunnel at $\alpha = -35.5°$ for a free stream velocity of $30\ m/s$.
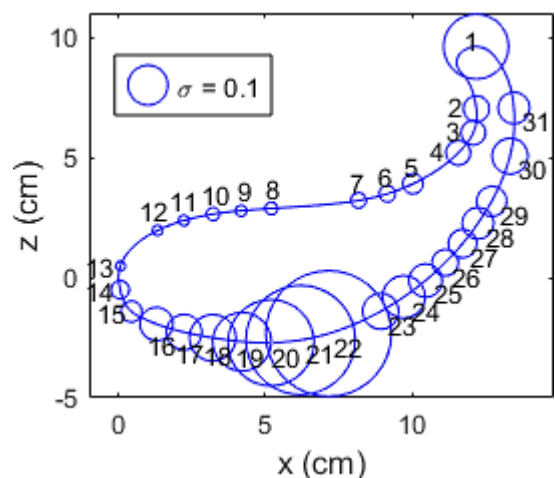
Figure 30. Mean pressure coefficient obtained from pressure experiment on the wind tunnel at $\alpha = -35.5°$ for a free stream velocity of $30\ m/s$.

On Figure 29 and Figure 30 the same graph but for $\alpha = -35.6°$ are shown. Both graphics are very similar to the ones of $\alpha = -30.5°$. The biggest differences are the σ of the tap 1, that is a little lower, and for the taps 18-22, where the standard deviation rises more than for the other angle of attack.

3.2. 3D car

The second wind tunnel experiment corresponds to the one performed with a scale car. In order to determine the real direction and magnitude of the velocity seen by the aileron, the flow on the rear part of the car, where the aileron is placed, has to be measured. The bodywork of the car placed upstream of the aileron changes the direction and the magnitude of the velocity. This effect has to be taken into account for the study of the performance of the aileron and it will be used with the Prandtl lifting line theory to estimate the forces of the aileron when it is placed on the Fun Cup Evo 3.
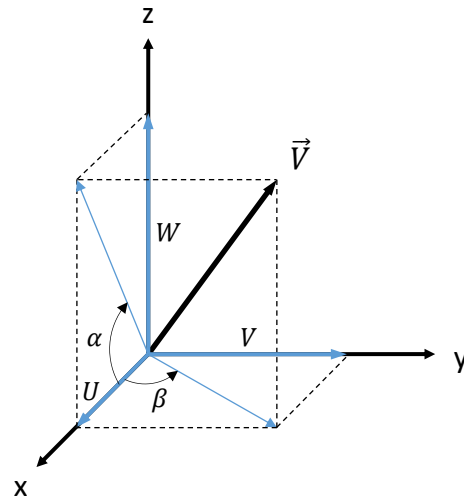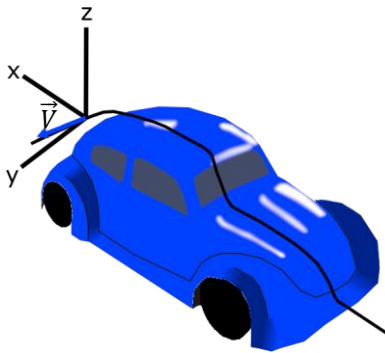
Figure 31. Scheme of a stream-line of the car and the measured velocity vector with the coordinates system used on this project.

Figure 32. Definition of the vertical deflection of the flow, α, and the sideslip angle, β, used on the experiment of the car of the wind tunnel

On Figure 31 there is a scheme of a streamline around the car, and the measured velocity at the rear part. In addition, the figure shows the criterion used on the coordinates axis: the x-axis on the direction of the free stream velocity, the z-axis on the vertical direction pointing upward, and the y-axis forming a right-handed coordinate system. Furthermore, on Figure 32, the criterion used to defined the vertical deflection angle, α_{car}, and the sideslip angle, β, is shown from the components of the velocity vector: U, V and W.
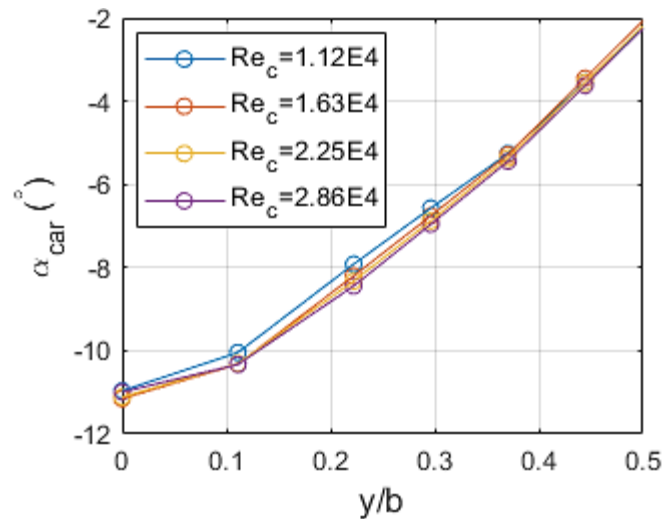
Figure 33. Deflexion of the flow induced by the car along the span for different Reynold numbers.

The study performed on a scale car on the wind tunnel has been done measuring the velocity in a totality of 11 points situated along the span of the wing. The measures were done in both sides of the wing, carrying out, afterwards, an average of both sides so as to minimize possible errors with the line-up or asymmetries of the model. The experiment was done for different velocities so as to analyse the Reynolds effect on the vertical deflection angle, α, the ratio of the norm of the measured velocity to the free stream velocity and the turbulence intensity. The values of these quantities along the span for the different Reynolds numbers are shown on Figure 33, Figure 34 and Figure 35, respectively.
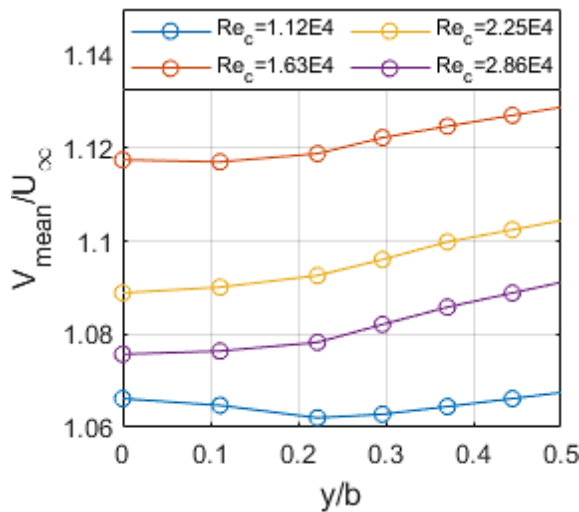
Figure 34. Ratio of the mean value of the velocity on the flow accelerated by the car to the free stream velocity along the span for different Reynold numbers.
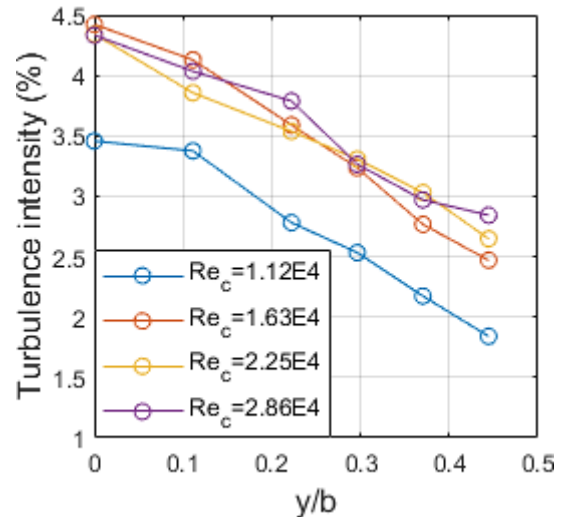
Figure 35. Turbulence intensity of flow on the rear of the car along the span for different Reynold numbers.

As the experiments were done on a 1:10 scale car, even though the tests were performed at $10\,m/s - 25\,m/s,$ the Reynolds numbers of these tests are smaller than the studied one for the experiments of the wing, that varies from $10\,m/s$ to $40\,m/s,$ corresponding to Reynolds numbers on the interval of $[1.12 \cdot 10^5, 4.5 \cdot 10^5]$. As a consequence, when the results of the deflection or the flow were needed, the ones

corresponding to the higher Reynolds number are going to be used, that is $Re_c = 2.86 \cdot 10^4$.

It is important to remark the c subscript that indicates that the Reynolds number used is the one based on the chord of the wing. The reason of this is for being able to compare it to the one of the wing data. But, in order to evaluate the flow on the rear of the car, it is important to know the Reynolds numbers of the experiment taking as reference longitude the length of the car. So, as the scale car's length is $38\ cm$ and the scale chord length is only $1.7\ cm$, the Reynolds numbers based on the length of the car are more than 20 times higher than the other one. This made values on the interval of $[2.5 \cdot 10^5, 6.5 \cdot 10^5]$. So, taking as reference the critical Reynold number of a flat plate, that is of about $5 \cdot 10^5$, it is probably that at least the highest Reynolds number corresponds to a supercritical one. So, the flow is expected to be turbulent at the rear part of the car for this velocity. This minimizes the differences between the results obtained for $Re_c = 2.86 \cdot 10^4$ and the quantities for higher Reynolds numbers, even though a Reynolds effect is still present.

Analysing the Figure 33, Figure 34 and Figure 35, it can be observed that the Reynolds effect is almost negligible, in the tested range, on the vertical deflection of the flow but is relatively important on the acceleration and the turbulence intensity of the flow on the rear of the car. Regarding the ratio of the measured velocity to the free stream velocity and the turbulence intensity, it is observed that there is an abrupt change between the first and the second Reynolds number (blue and orange lines, respectively). The reason of this behaviour could be on a transition to a supercritical Reynolds number. This would explain the fact that the turbulence intensity for the smallest velocity is lower than for the other cases of studies and would reinforce the theory that the Reynolds number is supercritical for at least the highest free stream velocity. In fact, all the tests would be at supercritical Reynolds numbers except the one made at $10\ m/s$ ($Re_c = 2.12 \cdot 10^4$).

Once the Reynolds effect is analysed, the evolution of the different parameters along the span are analysed too. For all the different velocities, the vertical deflection is more pronounced on the root of the wing than on the tips where only a deflection of $-2°$ is generated. This implies that the effective angle of attack seen by the wing root is lower, or more negative, than the one seen by the wing tips. An important spanwise evolution occurs too for the turbulence intensity. Just as for the induced α, the highest value in terms of the absolute value takes place in the middle of the wing. Regarding the ratio of the measured velocity to the free stream velocity, its variation along the span is not very important with a rise of only 0.015 from the middle of the wing to the tips for $Re_c = 2.86 \cdot 10^4$.

Apart from the mentioned variables, the components of the velocity and the sideslip angle, β, can be studied. Even though the effect of the sideslip angle on the wing is not studied on this work, as it can not be changed by placing the wing on a different position on the car, it is important to notice that the car has an effect not only on the direction of the flow on a vertical plane, but also induced a spanwise variable sideslip angle.

Up to now all the variables calculated have an even symmetry and, therefore, they have been represented for only one side of the wing. Although, as it was explained before, the measures have been done on both sides of the wing for minimizing the

asymmetries of the set up. But for studying the sideslip, the representation of both sides is needed as it has an odd symmetry, that is, the absolute values in both sides are the same but with opposite sign. In this case, β is positive for negative values of y, and is negative for positive values, so the flow is deviated to the symmetric plane. Representing both sides does not mean that the mean value of both sides has not been calculated. As for the rest of variables, for achieving real symmetric values, the mean between both sides is done, but this time considering only the absolute values.

In addition, some corrections are needed for the sideslip angle. For all the variables, there are some deviations between the symmetric values and the measured ones, but they are included into reasonable limits. But for the β angle, the deviations reach values of around $3°$, whereas for α all the deviations are smaller than $1°$. Moreover, due to the odd symmetry the sideslip angle must be zero at $y = 0$. However, the measured angle at this position has a value of around $-2.33°$ for all the velocities. Subtracting this value to all of the measures, a more symmetric angle is obtained, and the deviations are reduced to less than $1°$, that is, to similar values than for the other variables. The reason of this constant deviation is explained if there is an error on the alignment of the cobra probe on the set up, so the results are corrected by a rotation of this angle with respect to the z-axis.
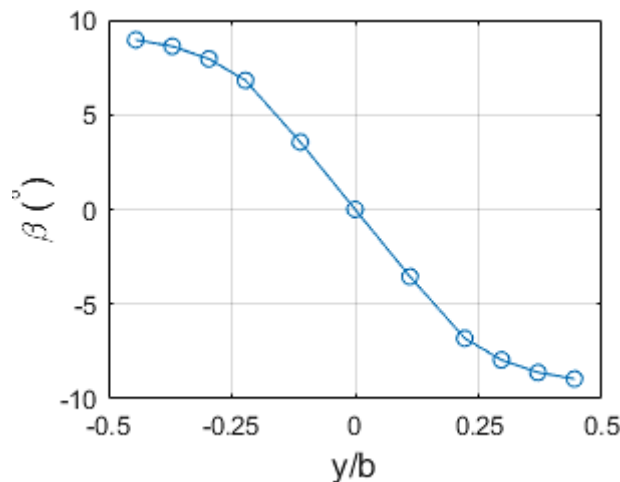
Figure 36. Sideslip angle induced by the car along the span for different Reynold numbers.

So once corrected the sideslip angle, the obtained values for the highest Reynolds number are shown on the Figure 36 .It can be observed that the lateral deflection is not negligible at all, reaching values of around $9°$ on the tips of the wing. In addition, a linear behaviour can be observed on the central region, with a high increase of β in a short range of y. However, near the tips, the curve bends, leading to smaller increases of β.

Furthermore, on Figure 37 the three components of the velocity for the same Reynolds number are shown. Consequently, with the correction of the β angle, the velocity along the y-axis has been corrected too. This variable has an odd symmetry too, while the other two components has an even symmetry. Analysing these three variables, it can be observed that the y-component, v, and the z-component, w, suffer a variation along the span very similar in magnitude, but with different evolutions, that correspondent to the behaviour of the respective angle (β and α). Whereas the x-component, u, is

almost constant along the span, having a variation of only $0.7\ m/s$ from the root to the tips when its values are around of $27\ m/s$, that is, less than a 3%.
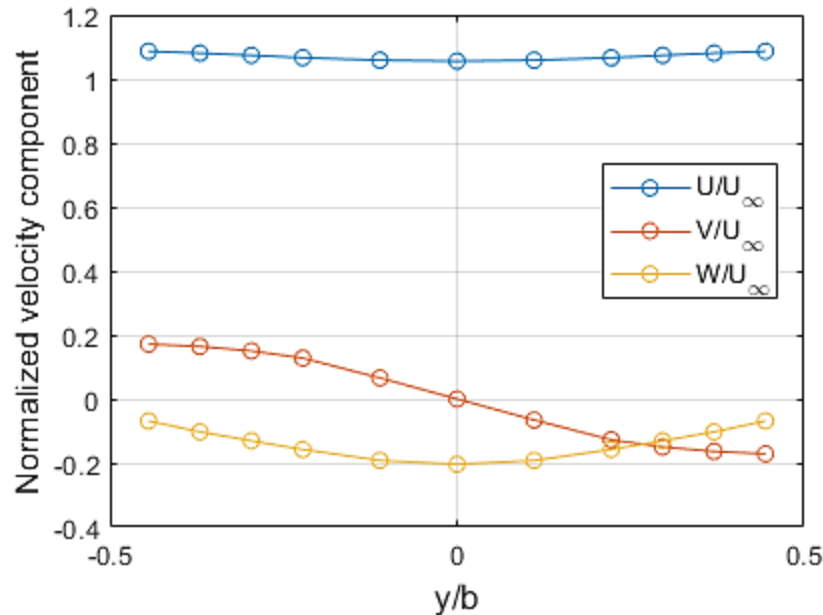
Figure 37. Turbulence intensity of flow on the rear of the car along the span for different Reynold numbers.

It is important to remark that, except the turbulence intensity, that quantifies the fluctuation of the flow, all the other variables are presented with their mean values along time.

3.3. 3D wing

Once the 2D profile is analysed, the completed wing is studied in this section. This study is divided into two parts. On one hand, there are the results of the force test carried out on the wind tunnel. On the other hand, the 2D measurements and the upstream deflection of the flow are used to estimate the 3D forces of the wing by the application of the Prandtl lifting line theory.

3.3.1.   Aerodynamic forces

In this section, the results of the experimental forces are presented. The ATI omega sensor measures the three components of forces and moments, but only the vertical force (z axis) and the longitudinal force (x axis) are studied as the two aerodynamic forces of more interest on the car are the downforce, or negative lift, and the drag. To analyse these forces, the dimensionless coefficients C_L and C_D are applied:

$$C_L = \frac{L}{\frac{1}{2}\rho V_\infty^2 S} \quad ; \quad C_D = \frac{D}{\frac{1}{2}\rho V_\infty^2 S} \tag{8}$$

Where $S = b \cdot c$ is the area of reference, $c = 0.17\,m$ is the chord length and $b = 1.35\,m$ is the span length.

As the tests are done with the wind and the frame mounted on the sensor, first, it is necessary to aerodynamically characterize the frame, so as to subtract its contribution to the total force measured. This study has been done for a range of angles of attack similar to the one of the wing tests and for three different velocities: $10\,m/s$, $20\,m/s$ and $30\,m/s$. It is important to recall the parasitic force that appears on the x-axis. This force must be subtracted in the frame tests to obtain the frame forces. Afterwards, in the tests with both the frame and the wing, not only the frame force has to be subtracted but also the correspondent parasitic force of these tests.
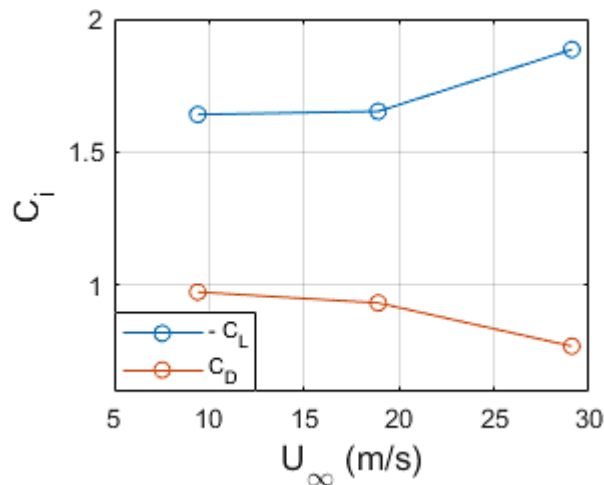
Figure 38. Reynolds effect of the downforce and drag coefficients obtained with wind tunnel force experiment.

First of all, the Reynolds effect in both quantities is analysed. This study is performed at $\alpha = -31.25°$ and for the three velocities: $10\,m/s$, $20\,m/s$ and $30\,m/s$. The results can be observed on Figure 38. Both downforce and drag are very similar for the two first velocities that correspond to $Re = 1.05 \cdot 10^5$ and $2.11 \cdot 10^5$, with a little decrease of the drag with the Reynolds number and an almost imperceptible rise of the downforce coefficient. This tendency grows for the last velocity, $30\,m/s$. This means that the performance of the aileron improves with the velocity in means of the downforce-to-drag ratio. But this does not mean that the drag decreases with the velocity, as the drag rises with the square of the velocity, being this effect higher than the reduction of the drag coefficient. This can be observed on Figure 39, where the forces are shown. Regarding the negative lift, both effects, the rise of the coefficient and the increment with the square of the velocity, are added, resulting in a big increase with the velocity. Normally this amount of increase is unnecessary as the tire performance slightly depends on the velocity.
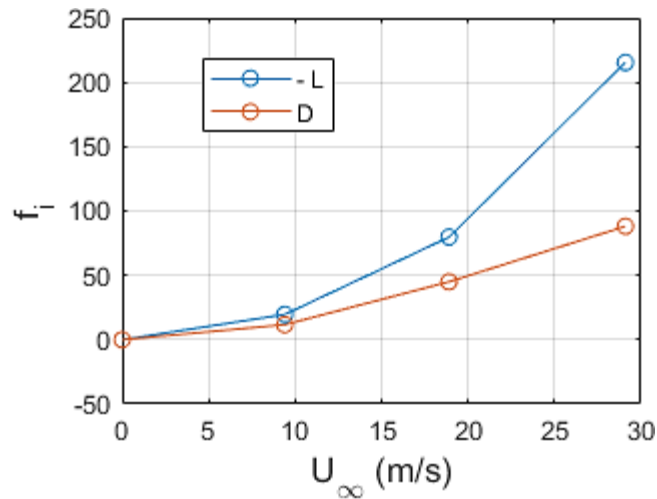
Figure 39. Reynolds effect of the downforce and drag coefficients obtained with wind tunnel force experiment.

Once the Reynolds effect is studied, the variation of the aerodynamic forces with the angle of attack is analysed for a velocity of $30\,m/s$. On Figure 40 the evolution of the downforce and drag coefficient is shown whereas on Figure 41 the lift-to-drag ratio can be observed. Starting from the highest angle of attack ($\alpha = -1.5°$), when the angle decreases, the drag increases in an almost linear way while the lift rise faster up to $\alpha = -31.3°$ where the maximum is found, and after that the downforce coefficient decreases.
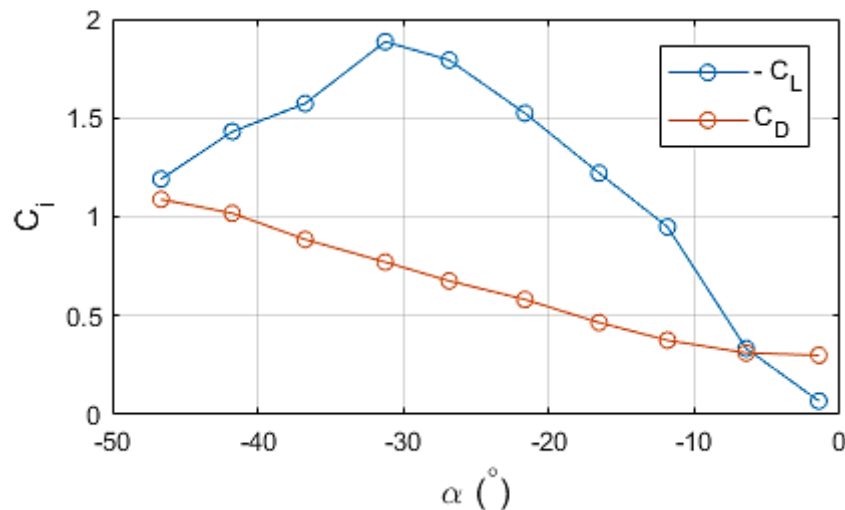
Figure 40. Variation of the negative lift and drag coefficients with the angle of attack obtained with wind tunnel force experiment.

As for the ratio of downforce to drag or, what it is the same, the ratio of downforce coefficient to drag coefficient, from left to right the ratio rise quickly up to $\alpha = -11.9°$. After that, there is an almost constant zone until $\alpha = -31.3°$ from which the ratio begins to decrease. Even though on the interval between $-11.9°$ and $-31.3°$ the ratio is almost the same, there is a maximum on $\alpha = -26.9°$ with $L/D = 2.65$. But this point does not have to mean that this is the optimum performance point, as it depends on the requirements. For example, at $\alpha = -16.6°$ the ratio is only 0.03 lower than in the maximum and a reduction of 0.21 on the drag coefficient is achieved.
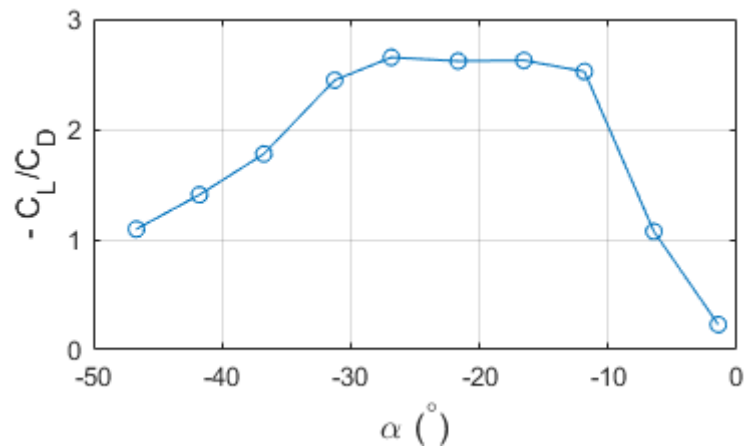
Figure 41. Variation of the ratio of downforce to drag obtained with wind tunnel force experiment.

As this point it is important to remark the bad performance of the wing comparing with the ones used in the airplane industry. The maximum downforce-to-drag ratio obtained for the studied wing is less than 3, whereas for a typical wing of a commercial airplane is between 12 and 20. Given the shape of the wing that is not streamlined, this bad result was expected.

3.3.2.   Prandtl Lifting Line

Up to now, the wing has been studied only for uniform free stream conditions. But, as it has been observed with the study of the deflection of the flow induced by the car, on the real conditions of the aileron placed on the car the flow is not uniform. To study how this non-uniformity affects the performance of the aileron, the Prandtl lifting line theory is used. The study is going to be made only with the vertical deflection of the flow, α_{car}, as it is considered the most important effect. But, on future works it would be interesting to add the effect of the sideslip angle, β_{car}, and the acceleration generated by the car. On the Prandtl lifting line the 3-dimensional forces are obtained being based on the 2-dimensional characteristics of the profile and as a function of the aspect ratio of the wing defined as $AR = S/c$.

This section is divided into several subsections. First of all, there is a brief introduction to the theory. Secondly, the method used to resolve numerically the fundamental equation of the lifting line is explained. Next, before implementing the theory for solving the aileron with the free stream conditions of when is placed on the car, two validations are done.

The first validation consists in applying the developed code with the explained numerical method on a wing whose solution is known, in order to confirm the correct behaviour of the implementation. The selected wing has been the widely-known elliptical wing with a flat plate profile. The second validation consists in solving the aileron with the wind tunnel conditions and making a comparison to the forces obtained from the wind tunnel experiment. As the wind tunnel forces were obtained for $30 \ m/s$ this is the velocity in which the lifting line is applied. This validation allows to study the limitations of the theory and try to correct the 2-dimensional data obtained from the wind tunnel, as it is

affected by 3-dimensional effects. Finally, the theory is applied to the case of interest of the aileron with flow perturbed by the induced angles of attack by the car.

Introduction: Prandtl Lifting Line theory

The Prandtl lifting line theory was developed by Ludwig Prandtl within the framework of potential theory. It allows to approximate, in a mostly accurate way, the lift and the induced drag of finite wings of high aspect ratio, with no sweep and no dihedral. [20] Being based on the potential 2D theory for infinite wings, Prandtl supposed that the lift of a spanwise section can be obtained by applying the Kutta- Yukowski law: [21]

$$L'(y_0) = \rho V_\infty \Gamma(y_0) \tag{9}$$

Moreover, Prandtl supposed that the circulation must vary spanwise. In order to obtain this effect, the wing is modelled by a line of bound spanwise vortex with ramifications of vortices trailing downstream. [22] Where each section of the bound vortex corresponds to the ones of a 2D section seeing a flow velocity due to the sum of the free stream velocity and the velocity induced by the trailing vortex sheet. [20] Since the total circulation has to be conserved in each ramification and having an infinite number of trailing vortex forming a continue sheet, the strength of each trailing vortex is $d\Gamma = (d\Gamma/dy) \cdot dy$. [22] Applying the Biot-Savart law, the vertical velocity induced in the section y_0 by the trailing vortex placed at y is:

$$dw = -\frac{(d\Gamma/dy)dy}{4\pi(y_0 - y)} \tag{10}$$
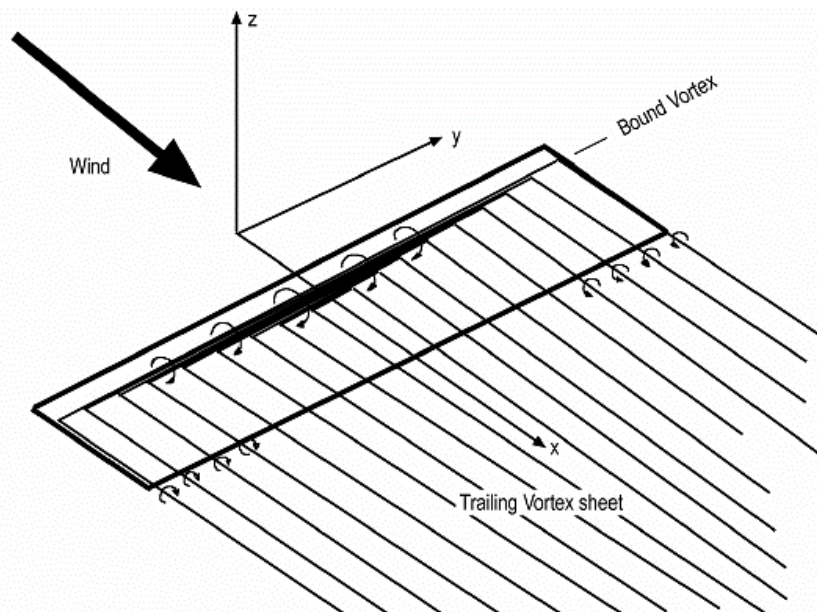
Figure 42. Vortices used to model the wing on Prandtl lifting line theory. [23]

Integrating the effect of all the vortices, the velocity induced in this section is:

$$w(y_0) = \frac{-1}{4\pi} \int_{-\frac{b}{2}}^{\frac{b}{2}} \frac{\left(\frac{d\Gamma}{dy}\right)dy}{(y_0 - y)} \tag{11}$$

Considering the induced velocity to be small with respect to the free stream velocity and defining the induced angle of attack, α_i, positive then the vertical velocity is upward[1], the α_i obtained in the spanwise section y_0 is:

$$\alpha_i = \tan^{-1}\left(\frac{w(y_0)}{V_\infty}\right) \approx \frac{w(y_0)}{V_\infty} \tag{12}$$

And the effective angle of attack, α_{eff} seen by each section is:

$$\alpha_{eff} = \alpha + \alpha_i \tag{13}$$

Where α is the geometric angle of attack.

Now, using the expression for the lift of the 2D airfoil theory for small angles of attack where the lift coefficient is approximated by: [22]

$$c_l(y_0) = a_0[\alpha_{eff}(y_0) - \alpha_{L0}] \rightarrow$$
$$\rightarrow L'(y_0) = \frac{1}{2}\rho V_\infty^2 c(y_0) c_l = \frac{1}{2}\rho V_\infty^2 c(y_0) a_0[\alpha_{eff}(y_0) - \alpha_{L0}] \tag{14}$$

where α_{L0} is the angle of attack of the 2D airfoil at which the lift is zero, and in combination with the Kutta-Yukowski law, the $\alpha_{eff}(y_0)$ can be expressed as a function of the circulation, $\Gamma(y_0)$:

$$\alpha_{eff}(y_0) = \frac{1}{a_0}\frac{2\,\Gamma(y_0)}{V_\infty c(y_0)} + \alpha_{L0} \tag{15}$$

Finally, applying the equation of the vertical induced velocity, the fundamental equation of the Prandtl lifting line theory is obtained:

$$\alpha(y_0) = \frac{2\Gamma(y_0)}{a_0 V_\infty c(y_0)} + \frac{1}{4\pi V_\infty}\int_{-\frac{b}{2}}^{\frac{b}{2}} \frac{\left(\frac{d\Gamma}{dy}\right)dy}{(y_0 - y)} + \alpha_{L0} \tag{16}$$

Resolution of the Prandtl lifting line equation

The fundamental equation of the Prandtl lifting line theory has associated the direct problem, in which the geometrical considerations are known and the equation is solved to obtain the circulation, and the indirect problem, in which the circulation distribution is known. The indirect problem is resolved immediately, but the direct problem, which requires solving an integral equation, is not that simple. Over the years several approaches have been proposed. One of the most common is using a collocation

---

[1] This sign convection, opposite to the habitual one, has been selected since having an inverted wing, it is expected an upwash instead the usual downwash for non-inverted wings.

method, expressing the circulation distribution with sine finite series. Among these methods is the straightforward scheme proposed by Glauert, that is the one used in this work. [24]

For resolving the equation, a change of variable replacing y by θ as the variable for the spanwise location is needed:

$$y = -b/2 \cos\theta \tag{17}$$

And the circulation is expressed as a Fourier sine series:

$$\Gamma(\theta) = 2bV_\infty \sum_{n=1}^{\infty} A_n \sin n\theta \tag{18}$$

As θ varies from 0 to π, the circulation on the tips is automatically zero. Substituting this expression in the expressions of α_i and α_{eff} and proceeding with the mentioned change of variable:

$$\alpha_i(\theta_0) = \frac{-1}{\pi} \int_{-\frac{b}{2}}^{\frac{b}{2}} \frac{\sum_{n=1}^{\infty} nA_n \cos n\theta \, d\theta}{(\cos\theta_0 - \cos\theta)} = \frac{1}{\pi} \int_{-\frac{b}{2}}^{\frac{b}{2}} \frac{\sum_{n=1}^{\infty} nA_n \cos n\theta \, d\theta}{(\cos\theta - \cos\theta_0)} \tag{19}$$

$$\alpha_{eff}(\theta_0) = \frac{4b}{a_0 \, c(\theta_0)} \sum_{n=1}^{\infty} A_n \sin n\theta_0 + \alpha_{L0} \tag{20}$$

In order to solve the integral of the equation of α_i, the Glauert integral is used:

$$\int_0^\pi \frac{\cos n\theta}{\cos\theta - \cos\theta_0} d\theta = \frac{\pi \sin n\theta_0}{\sin\theta_0} \tag{21}$$

And the induced angle of attack results:

$$\alpha_i(\theta_0) = -\sum_{n=1}^{\infty} nA_n \frac{\sin n\theta_0}{\sin\theta_0} \tag{22}$$

Joining these results together, the fundamental equation becomes:

$$\alpha(\theta_0) = \frac{4b}{a_0 c(\theta_0)} \sum_{n=1}^{\infty} A_n \sin n\theta_0 + \alpha_{L0} + \sum_{n=1}^{\infty} nA_n \frac{\sin n\theta_0}{\sin\theta_0} \tag{23}$$

Since in this report the studied wing has no twist, the geometric angle of attack is constant, $\alpha(\theta_0) = \alpha$.

As it corresponds for a collocation method, the infinite series is truncated at a finite number of terms N, that is solved by imposing the equation at N different locations along the span. [24] Moreover, for symmetrical wings, as for the one of this work, the odd coefficients A_n are equal to zero, and it is sufficient to consider just one side of the wing, that is, θ values from 0 to $\pi/2$. [24] This leads to a system of N equations with N unknown quantities. This system of equations has been solved numerically with the 'fsolve' command of Matlab.

Once the distribution of circulation is obtained, the lift and induced drag coefficients can be expressed as a function of the A_n parameters. As the total lift is obtained by integrating the local lift along the span, and considering the the Kutta-Yukowski law:

$$L = \int_{-\frac{b}{2}}^{\frac{b}{2}} L'(y_0) \, dy_0 = \rho V_\infty \int_{-\frac{b}{2}}^{\frac{b}{2}} \Gamma(y_0) \, dy_0 \tag{24}$$

Replacing the variable y by θ and introducing previously solved series, the coefficient of lift is:

$$C_L = \frac{L}{1/2 \, \rho V_\infty^2 S} = \frac{b}{V_\infty S} \int_0^\pi \Gamma(\theta_0) \sin \theta_0 \, d\theta_0 = \frac{2b^2}{S} \sum_{n=1}^{N} A_n \int_0^\pi \sin n\theta_0 \sin \theta_0 \, d\theta_0 \tag{25}$$

In order to solve the integral, the following property of the sines is used:

$$\int_0^\pi \sin m\theta \sin k\theta \, d\theta = \begin{cases} 0 & m \neq k \\ \dfrac{\pi}{2} & m = k \end{cases} \tag{26}$$

so, the integral is equal to zero for all the values of n except for $n = 1$ that is $\pi/2$. This leads to the fact that the lift coefficient depends only on A_1:

$$C_L = A_1 \frac{\pi A b^2}{S} = A_1 \pi AR \tag{27}$$

As for the drag, it is important to recall d'Alembert's paradox that the 2D potential theory, on which the Prandtl lifting line is based, satisfies. According to d'Alembert's paradox, the aerodynamic force produced on an object by an incompressible inviscid steady flow is perpendicular to the flow velocity, and therefore the drag is equal to zero. This is satisfied locally by each spanwise section, as the potential theory stipulates. But, as the direction of the local velocity (composed by the free stream velocity and the vertical induced velocity) is not the same as the free stream direction, the lift force in each section is not perpendicular to $\vec{V}_\infty$ and what is known as induced drag is generated. [22]

Taking into account the small angle hypothesis that is being used, the induced drag is calculated through the following equation:

$$D_i = \int_{-\frac{b}{2}}^{\frac{b}{2}} L'(y_0) \alpha_i(y_0) \, dy_0 = \rho V_\infty \int_{-\frac{b}{2}}^{\frac{b}{2}} \Gamma(y_0) \alpha_i(y_0) \, dy_0 \tag{28}$$

Introducing both the expressions for α_i and Γ and using the definition of the induced drag coefficient:

$$C_{D_i} = \frac{D_i}{1/2 \, \rho V_\infty^2 S} = \frac{2b^2}{S} \int_0^\pi \left(\sum_{n=1}^{N} A_n \sin n\theta_0 \right) \left(\sum_{n=1}^{N} n A_n \sin n\theta_0 \right) d\theta_0 \tag{29}$$

Solving the integral in the same way as with the lift:

$$C_{D_i} = \pi AR \left(A_1^2 + \sum_{n=1}^{N} n A_n^2 \right) = \pi AR \, A_1^2 (1 + \delta) = \frac{C_L^2}{\pi \, AR} (1 + \delta) \tag{30}$$

where:

$$\delta = \sum_{n=1}^{N} n \left(\frac{A_n}{A_1} \right)^2 \tag{31}$$

Total drag force

The aerodynamic drag can be divided into two components due to its cause: origin viscous and origin potential. For incompressible flows, the only potential term is the induced drag that is due to the vortices of the wake and can be obtained with the Prandtl lifting line, as it was already explained. For transonic and supersonic flows there is also what is called the wave drag, caused by shock waves.

On the other side, there are also two types of drag caused by the viscosity of the flow, associated to the boundary layer: the skin friction drag and the form drag or pressure drag. The skin friction drag is caused by the existing friction between the surface of the airfoil and the flow. And the form drag is due to the pressure distribution generated by the airfoil form. It is important to remark the viscous origin of this last term, which it is not immediate. The viscosity modifies the pressure distribution that otherwise will result in a null contribution.

The sum of skin friction drag and form drag is known as the profile drag or viscous drag. As its name indicates these terms have their origin on the viscosity, and therefore they cannot be determined by potential theory as the one used in this section. In order to obtain the profile drag, C_{D_p}, the bidimensional drag coefficient can be used, taking into account the effective angle seen by each spanwise section:

$$C_{D_p} = \frac{1}{b} \int_{-\frac{b}{2}}^{\frac{b}{2}} c_d \left(\alpha_{eff}(y_0) \right) \cdot dy_0 \tag{32}$$

The 2D drag coefficient, c_d, for different angles of attacks are extracted from the pressure wind tunnel test. It is important to take into account that with the wind tunnel experiment, only the form drag is obtained. But, as the studied aileron is not a streamline body but a bluff body with a detached boundary layer in much of its surface, the form drag term is the dominant term.

Test case #1: elliptic wing

In order to validate the developed implementation of the Prandtl lifting line, it is used to calculate the circulation distribution on an elliptic wing with flat plate profile and without

any twist. The elliptic wing and its circulation distribution are well-known as this configuration provides minimum induced drag for a certain value of lift in the framework of the Prandtl lifting line theory. Demonstrate this fact is relatively easy through the indirect problem. So, first of all, the distribution of circulation that generates minimum drag has to be known. Going to the equation that expresses the drag coefficient as a function of the lift coefficient, it can be easily observed that the minimum drag corresponds to $\delta = 0$. Hence, all the coefficients other than A_1 must be zero. This corresponds with an elliptical circulation distribution: [22]

$$\Gamma(\theta) = 2bV_\infty A_1 \sin\theta = \Gamma_0 \sin\theta \quad \rightarrow \quad \Gamma(y) = \Gamma_0 \sqrt{1 - \left(\frac{2y}{b}\right)^2} \tag{33}$$

Substituting this distribution in the expression of α_i as a function of θ, it is immediate that the induced angle of attack is constant along the span: $\alpha_i = -A_1$. Forcing the wing to have no twist, that is, have a constant geometric angle of attack, α, the effective angle of attack has to be constant too, and therefore:

$$c_l(y) = a_0 \left[\alpha_{eff} - \alpha_{L0}\right] = constant \tag{34}$$

Solving the definition of the 2D lift coefficient for the chord, $c(y)$, applying the Kutta-Yukowki law, it is obtained that the chord distribution must be elliptical as all the variables apart from the circulation are constant along the span: [22]

$$c(y) = \frac{L'(y)}{\frac{1}{2}\rho V_\infty^2 c_l} = \frac{2}{V_\infty c_l}\Gamma_0 \sqrt{1 - \left(\frac{2y}{b}\right)^2} = c_0 \sqrt{1 - \left(\frac{2y}{b}\right)^2} \tag{35}$$

So, as it was previously said, the elliptic wing provides minimum drag, and it has an elliptic circulation distribution.

Now that the circulation of the wing is known, the validation can be made. This validation is performed on an elliptic wing with the dimensions of the studied wing: $c_0 = 0.17\,m$ and $b = 1.35\,m$. This corresponds with a wing surface of $S = 0.18\,m$ and an aspect ratio of $AR = 10.11$, obtained using the following expressions:

$$S_{ellip} = \int_{-b/2}^{b/2} c(y)\,dy = c_0 \int_{-b/2}^{b/2} \sqrt{1 - \left(\frac{2y}{b}\right)^2}\,dy = \frac{\pi}{4}c_0 b \tag{36}$$

$$AR_{ellip} = \frac{S_{ellip}}{b^2} = \frac{4b}{\pi c_0} \tag{37}$$

For the 2D parameters, they are $a_0 = 2\pi$ as stablished by the thin airfoil theory, and $\alpha_{L0} = 0$ as the profile is a flat plate. Along this validation, the lifting line equation has been solved for $N = 10$. So, as the wing is symmetric with only 10 locations along one side of the wing is enough to obtain up to the coefficient A_{19}. This has been performed for nine α between $-20°$ and $20°$. For all of them, the coefficients obtained other than A_1 have negligible values. On Table 2, the value of A_1 and of the maximum value coefficient apart from A_1 written in absolute value are shown, for each α.

Table 2. Values of A_1 and the maximum value coefficient except A_1 for the elliptic wing at different angles of attacks

α (°)	A_1	$\max\{|A_n| : n = 2,3,...,2N-1\}$
-20	-0.0635	1.52938e-11
-15	-0.04765	1.1470e-11
-10	-0.031769	7.6469e-12
-5	-0.01588	3.82345e-12
0	0	0
5	0.01588	3.82345e-12
10	0.031769	7.6469e-12
15	0.04765	1.1470e-11
20	0.063538	1.52938e-11

So, the obtained circulation distribution has an elliptical form as expected and the induced angle of attack is constant spanwise. These results can be observed on Figure 43 and Figure 44 for $\alpha = 5°$, as an example.
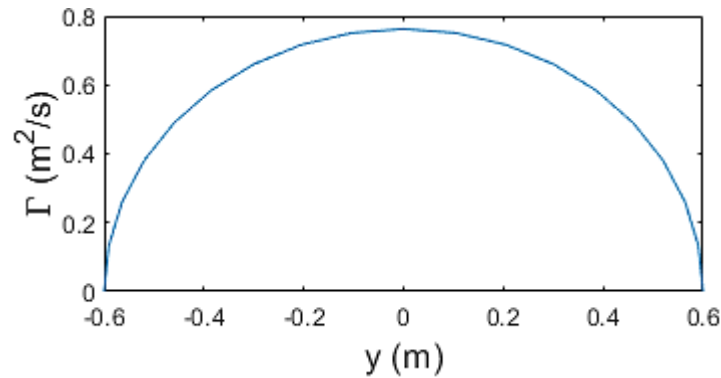
Figure 43. Circulation distribution of an elliptic wing with flat profile at $\alpha = 5°$ obtained with the Prandtl lifting line.
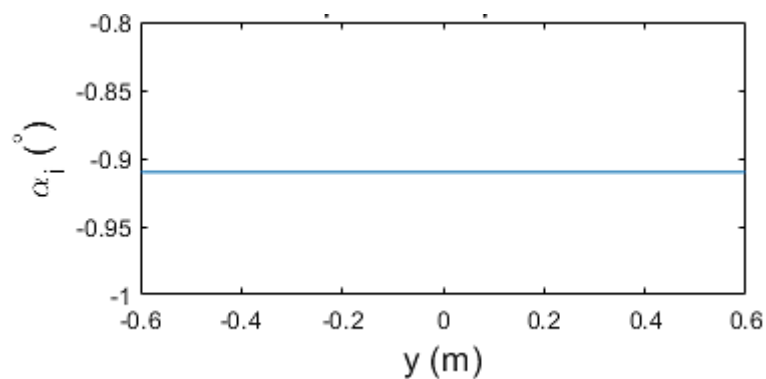
Figure 44. Induced angle of attack of an elliptic wing with flat profile at $\alpha = 5°$ obtained with the Prandtl lifting line.

Apart from checking that the distribution obtained has the desired form, in order to validate the program, it is important to check if the magnitude is the expected one. In order to do this, the distribution of C_L vs α is used through the coefficient $a = dC_L/d\alpha$. For the elliptic wing, the effective angle of attack of the sections is related to the geometric angle of attack by:

$$\alpha = \alpha_{eff} + A_1 = \alpha_{eff} + \frac{C_L}{\pi\, AR} \tag{38}$$

Calculating the derivative of this equation with respect to C_L and taking into account that for this wing $C_L = c_l$ so $a_0 = dC_L/d\alpha_{eff}$:

$$\frac{1}{a} = \frac{1}{a_0} + \frac{1}{\pi\, AR} \tag{39}$$

So

$$a = \frac{a_0}{1 + \dfrac{a_0}{\pi\, AR}} \tag{40}$$

This expression for a generic wing is modified to include the parameter τ, which depends on the shape of the wing:

$$a = \frac{a_0}{1 + \dfrac{a_0}{\pi\, AR}(1 + \tau)} \tag{41}$$

With the numeric values of a_0 and AR of the elliptic wing that is used in this validation, it is obtained a value $a = 1.67\pi$. On Figure 45 it can be observed that the values of C_L obtained numerically are fitted completely to a line with a slope a. And, therefore, the developed code is correctly validated.
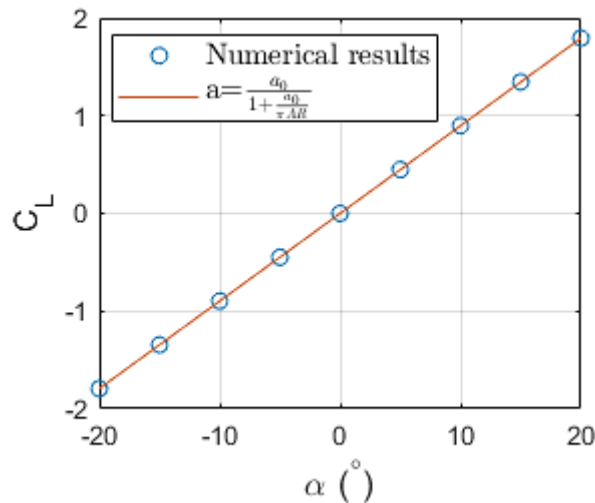
Figure 45. Comparison between the distribution of lift coefficient against α obtained numerically with the Prandtl lifting line and the predicted one for an elliptic wing with flat profile.

Test case #2: aileron without the car

Once it is checked that the developed code reproduces correctly the Prandtl lifting line theory, the code is going to be used on the study of the wing with the wind tunnel conditions, in order to validate it with the force test made on the wind tunnel. This study is performed for a free stream velocity of 30 m/s, same velocity than the forces

experiment. As the studied wing is a rectangular one, in this case the wing surface is $S = b \cdot c = 0.23\ m^2$ and $AR = b/c = 7.94$.

In addition to these parameters, the data of the bidimensional airfoil are needed, as the profile is not a plate anymore, but the studied profile. These data are obtained from the pressure test of the wind tunnel, but there are some issues with these results that has to be analysed. The first is that, as the lift coefficient is obtained by integrating the pressure distribution, the viscosity contribution to the lift is not taken into account. Nevertheless, as it is a bluff body, the viscosity contribution is expected to be small so this deviation can be considered despicable. Another issue is related with the fact that the pressure distribution does not correspond exactly with the ones of the bidimensional airfoil, as the test is affected by the same three-dimensional effects that are studied in this section. This will be treated later on.

Another thing that has to be taken into account is the fact that the curve of the lift coefficient against the angle of attack does not approximates a line, and therefore, the lift coefficient can not be approximated with a constant a_0. In order to use the same formulation used up to now, an a_0 is calculated for each angle of attack, obtaining a set of values, using the equation that express the 2-dimensional lift coefficient as a function of the parameter a_0. On Figure 46 and Figure 47, the values of c_l and a_0 against α can be observed.
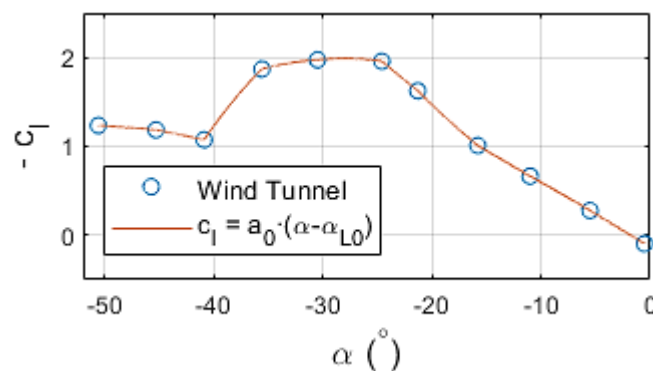
Figure 46. Distribution of the 2-dimensional negative lift coefficient against α obtained from pressure test on the wind tunnel. Experimental results and approximation of this results using a_0.
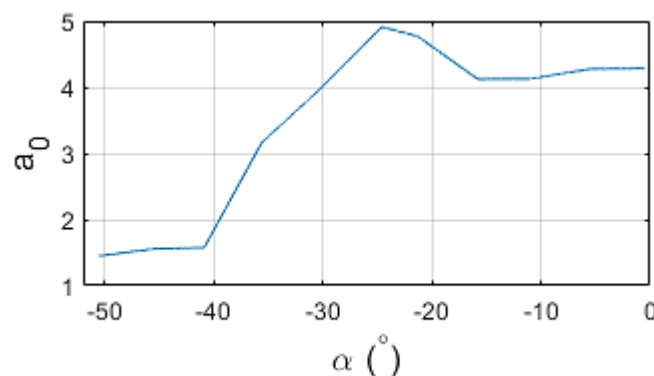
Figure 47. Distribution of a_0 against α obtained from results of the pressure test performed on the wind tunnel.

As the wing is symmetric, just as in the last section, only one side of the wind is used, allowing to calculate a number of coefficients A_n with half of the points. . This means

that, for example, to calculate the coefficients up to A_{15}, only 8 points along the wing are needed ($N = 8$), and therefore, a system of eight equations and eight variables is needed to be calculated (the variables correspond to the coefficients with odd n placed between A_1 and A_{15}, as the terms with even n are null). Notice that N has be defined as the number of points used, not the number of the maximum coefficient, so it corresponds to the dimension of the system of equations that is solved.

For the elliptical wing, as the problem was very simple, the number of coefficients calculated were not really relevant, so it was stablished on 19 (that is $N = 10$) since the beginning without a further study. But, for the actual problem the accuracy of the solution depends on the number of coefficients calculated. The more coefficients are calculated, the better the accuracy of the solution is, but the greater the dimension of the system of equations that has to be calculated is. This augmentation of the dimension of the system leads to an exponential increase of the computational cost. This is the reason why it is important to study the optimum number of terms calculated. This study is going to be done for the angle of attack of $-20°$ and comparing both the lift coefficient and the drag coefficient. The result of this study is shown on Table 3, Figure 48 and Figure 49, where the time of computation can be seen for each case as well as the values of C_L and C_{D_i} obtained.

Table 3. Execution time, lift coefficient and drag coefficient obtained with the Prandtl lifting line for different numbers of points along the span of the wing at $\alpha = -20°$

N	$t\,(s)$	C_L	C_{D_i}
3	0.02150	-1.17922	0.0730273
10	0.02275	-1.19497	0.0625567
30	0.03212	-1.19502	0.0625663
100	0.2874	-1.19502	0.0625665
∞	–	-1.19502	0.0625665
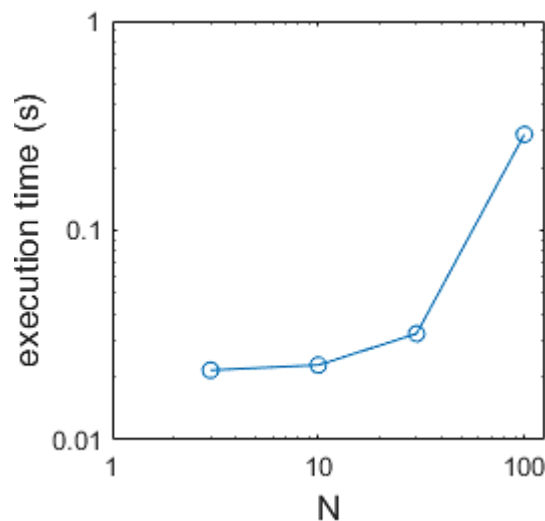
Figure 48. Execution time obtained with the Prandtl lifting line for different numbers of points along the span of the wing at $\alpha = -20°$.
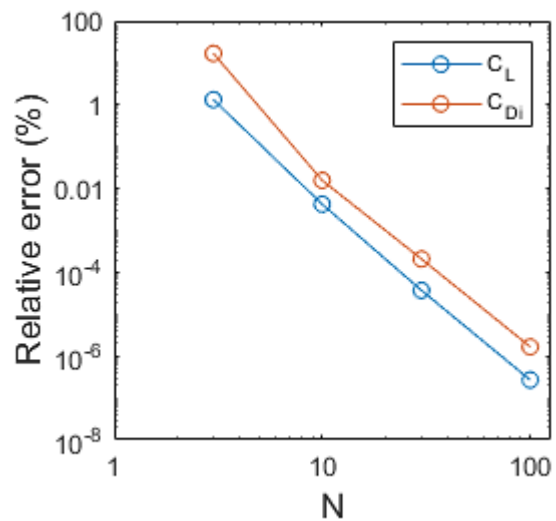
Figure 49. Relative error of lift and drag coefficient obtained with the Prandtl lifting line for different numbers of points along the span of the wing at $\alpha = -20°$.

As it was predicted, the computational cost increased exponentially with the number of terms of the system of equations. With regard to the lift and drag coefficient, it can be observed that they converge very quickly with N. Even with only 3 points along the wing, the relative error is only about 1% for the lift coefficient but it is about 15% for the drag coefficient, taking as reference the value obtained with 1000 terms considered as the limit value of $N \to \infty$. This relative error decreases exponentially with N, reaching despicable values with only tens or hundreds of points. Taking these aspects into account the selected N value is 30, as the accuracy is more than enough.

Both 10 or 100 could be used too, as neither the relative error of 10 is bad nor the execution time of 100 is too high. But, as the execution time of 10 and 30 are very similar, it compensates this little increment of time for having a better accuracy. And with regard to 100, even though the execution time is small, it is 10 times higher than for 30, and this increment of time is not justified as the reduction on the relative error is not required at all.

It is important to remark that this computation time corresponds to the time that it takes to solve once a specific system of equations. But, when applying the lifting line theory for solving different angles and where an iterative process is needed, as it will be explained later, hundreds of systems of equations could be needed to be solved. In addition, each specific system of equations requires a different execution time that depends on the initial point, hence the values shown on this convergence study are presented only as a reference. What it is maintained for all the cases is the evolution of the accuracy and the execution time with the number of terms.

Once selected the optimum number of points along the span of the wing, the code can be applied for solving the different geometric angles of attack. In this case, the same angles of attack as the ones used on the pressure test on the wind tunnel are used, but for a smaller range of values from $\alpha = -35.6°$ to $\alpha = -0.5°$ This limitation on the range of angles of attack is made as the Prandtl lifting line is expected to be used around the AoA of zero lift, that corresponds to $\alpha_{L0} = -1.77°$. The limit range has been selected based on the fact that for angles of attack below $\alpha = -35.6°$ the lift starts to descend when the angle of attack decreases, while up to this angle of attack the lift rises when the angle of attack decreases or at least remains more or less constant. This change of behaviour of the curve of the lift against α leads to problems when applying the Prandtl lifting line for angles below this value, with a distribution of induced angles along the span of the wing that tends to oscillate.

The reason of using the same angles of attack as for the pressure wind tunnel experiment is to use more easily the results to correct the two-dimensional data. This correction is based on the fact that the values of alpha on Figure 46 are the geometric alpha even when they should be the values of the effective angle. To improve this, once the distribution of induced angles of attack along the span is calculated for each geometric angle of attack, the value of α_i for $y = 40\ cm$ (the place of the pressure measurements) can be used to correct the angle for each test. In addition, for each angle of attack not only the effective angle changes, but also the contribution to the lift and the drag of the aerodynamic force is modified since the reference axes change, as can be seen on Figure 50. The relation between the new lift, L', and drag, D', is:

$$L' = \cos\alpha_i \cdot L - \sin\alpha_i \cdot D \tag{42}$$

$$D' = \sin\alpha_i \cdot L + \cos\alpha_i \cdot D \tag{43}$$

Where L and D are the lift and drag, respectively, on global axes and L' and D' are the lift and drag on local axes. With these changes, new distributions of c_l against α and c_d against α are obtained, and therefore, the values of a_0 have to be recalculated. Repeating this process in an iterative way, the desired solution is reached.
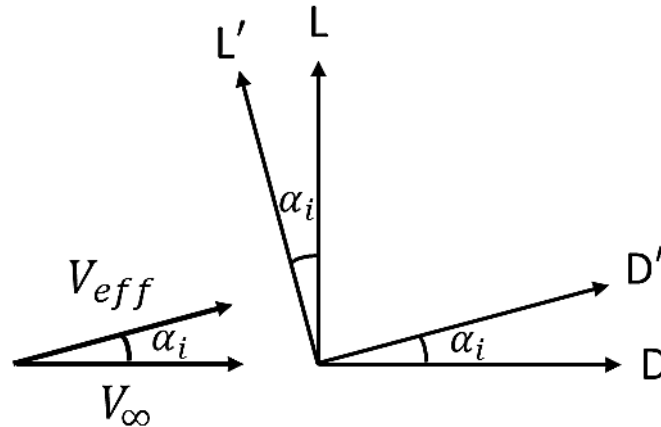
Figure 50. Graphical relation between the lift and drag obtained on global axes related to the direction of V_∞ (L and D) and the lift and drag obtained on local axes related to the direction of V_{eff} (L' and D')

In addition, as a_0 is not constant but depends on the effective angle, initially the induced angle is considered to be zero for all the geometric angles α, and therefore, the value of a_0 is constant spanwise. This is corrected with an iterating process too, that this time takes place inside each geometric angle of attack. Once the induced angle of attack is obtained, it is used for the next iteration on the α_{eff} used to calculate a_0, so the value of a_0 varies spanwise.

Before implementing this process, in which the data of the experiments are adjusted, the Prandtl lifting line is applied disregarding the fact that the effective angle and the geometric angle of the profile of the test on the wind tunnel are not the same. This still involves the iterative process for each geometric angle of attack, but this does not imply the recalculation of the two-dimensional lift coefficient against the angle of attack. However, the value of a_0 along the span of the wing varies in each iteration, because it depends on the value of $\alpha_{eff} = \alpha + \alpha_i$ that varies spanwise.

Applying this process, the distribution of C_L against α shown on Figure 51 is obtained. On this figure it can be also seen the results obtained from the force test on the wind tunnel. Comparing both, some differences can be observed but the approximation is acceptable. For angles higher than $-30°$, the downforce obtained from the lifting line theory is lower than the one obtained from the force test of the wind tunnel. Another difference is that the angle of the maximum downforce coefficient differs, as for the results of the wind tunnel the maximum is on $-30°$ and for the results of the lifting line the downforce for $-35°$ is a little bit higher than for $-30°$.
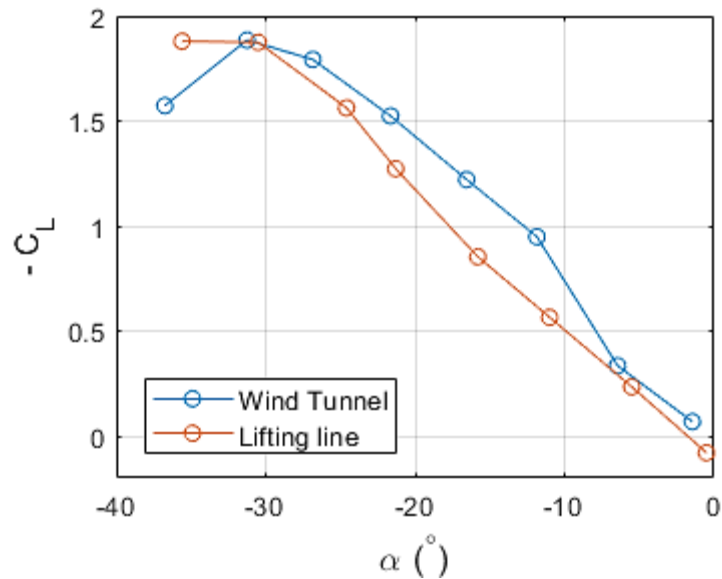
Figure 51. Variation of the downforce with α for the aileron without the car effect. Comparison between results obtained from Prandtl lifting line with method 1 with fixed 2-dimensional data and wind tunnel force test.

Once this first approximation of the lift coefficient is obtained, the complete iterative process described previously is carried out. At this stage, it is important to remark that the aileron has wing end-plates that reduce the effect of the wing tip vortex and, therefore, decrease the induced angle of attack. These effects are approximated with an increase on the effective aspect ratio. So, in order to try to take into account the effect of the end-plates on the aileron the iterative process is repeated incrementing the aspect ratio. In order to determine effective aspect ratio, the classical theory used on Donald R. Riley (1951) [25] on figure 13 has been used. As the height of the end plates is approximately $10\ cm$, which leads to $h/b = 0.074$, where h is the height of the end plates, the effective aspect ratio is approximately $AR_e = 1.144 \cdot AR = 9.085$. This is equivalent to a wing without end plates with a span of $155.25\ cm$ and the same chord as the real one. To sum up, the three methods used are:

- Method 1. No modification of the 2D data is done.

- Method 2. The 2D is modified with the effective angle of attack obtained in the profile where the measurements were performed.

- Method 3. Again, the 2D is modified as on method 2, but the effective aspect ratio is modified due to the end-plates effect.

Before taking a look into the comparison of the aerodynamic forces obtained from these three methods, the obtained induced angles of attack along the span are compared for one representative angle of attack, $\alpha = -21.3°$. As it can be observed on Figure 52, with the three methods the induced angle obtained has a similar shape with a central part more constant and an asymptotic behaviour on the tips. The method with the lowest α_i is the method 1, whereas the second method gives the biggest α_i. The third and last method provides an intermediate value, closer to the result of the second method.
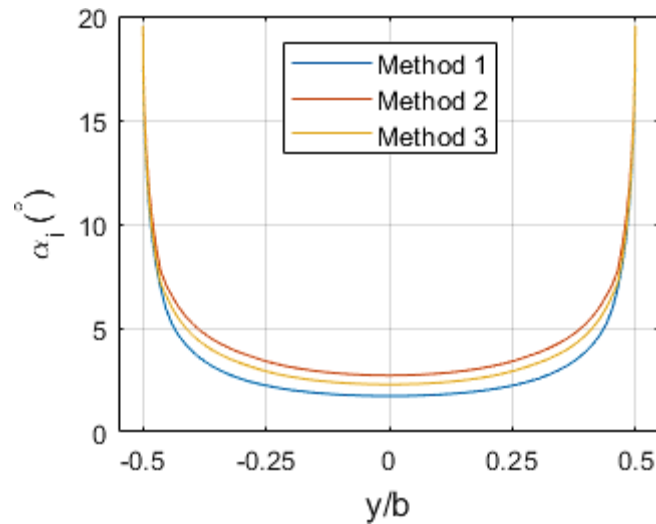
Figure 52. Induced angles of attack at $\alpha = -21.3°$. Comparison of the three methods defined to resolve the Prandtl lifting line.

On Figure 53 the solution obtained from these three methods for the lift coefficient together with the results of the force test on the wind tunnel can be observed. The method 1 corresponds to the one in which the 2-dimensional data remain fixed. While on methods 2 and 3 these data are modified, the method 2 with an aspect ratio of 7.94, that is, not taking into account the end-plates, and the method 3 with $AR = 9.085$, that is, approximating the effect of the end-plates.
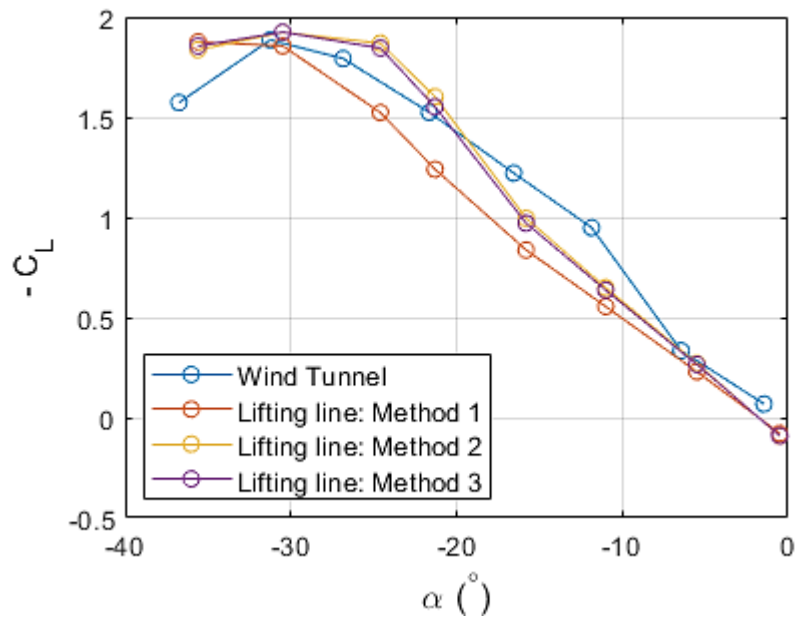
Figure 53. Variation of the downforce coefficient with α for the aileron without the car effect. Comparison between results obtained from Prandtl lifting line with three different methods and wind tunnel force test.

It can be seen that the three methods approximate considerably well the wind tunnel results, but both the second and the third ones gives better results. Not only because the global difference is smaller, but also as they approximate more correctly the form of the curve even though they are zones of the curves that differ. Comparing the method two and three, it can be observed that the result is practically the same, but the distance

between the curve of the method 2 and the wind tunnel results is a little bit lower than for the method 3.
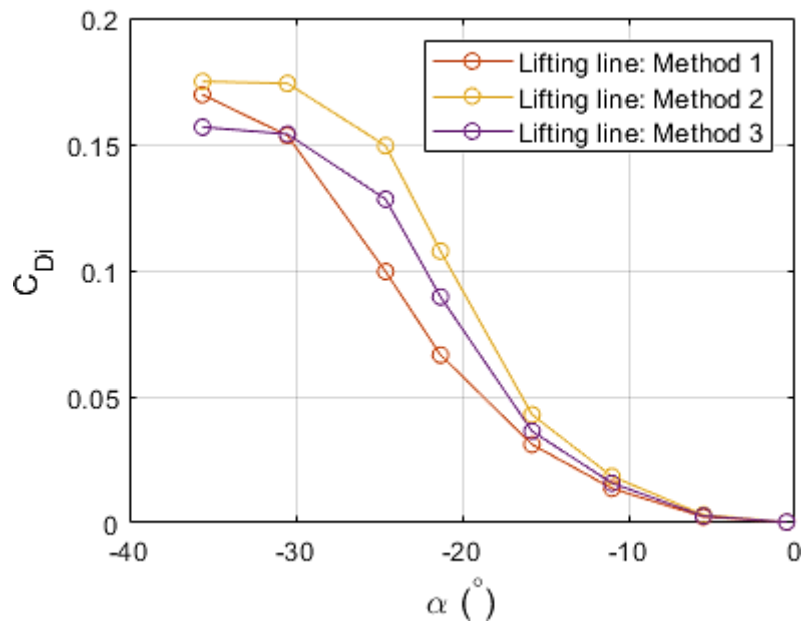
Figure 54. Variation of the induced drag coefficient with α for the aileron without the car effect obtained from Prandtl lifting line with three different methods.
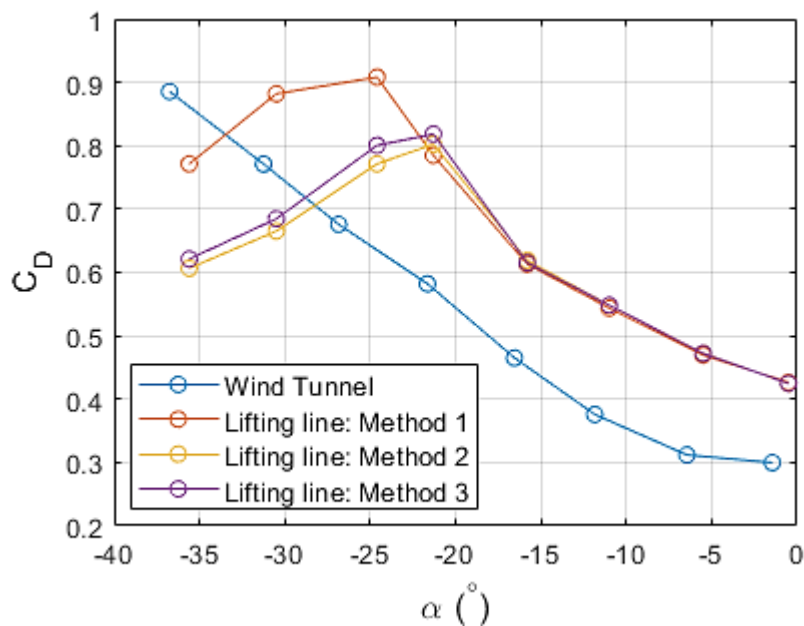
Figure 55. Variation of the drag coefficient with α for the aileron without the car effect. Comparison between results obtained from Prandtl lifting line with three different methods and wind tunnel force test.

Besides the lift coefficient, the induced drag coefficient is obtained too, and it is observed on Figure 54 for the three methods. Adding the profile drag, calculated by the integration of the 2D one considering the effective angles of attack, the total drag can be approximated and compared to the one obtained with the force test. The results from the three methods accompanied to the wind tunnel results are shown on Figure 55. It can be observed that the results for the drag are worse than for the lift comparing with the wind

tunnel results. The drag estimated is higher than the one obtained from the wind tunnel for almost all the angles of attack. In this time the approximation with the minimum difference with the reference is the first one, but the three differences are very similar.

As the method 2 was the one that better approximates the lift coefficient, from now on the two-dimensional distributions of the c_l and c_d against α obtained from method 2 are the ones that are going to be used to calculate the forces of the aileron when it is placed at the rear of the car in the next section and to compare with the simulations. These distributions are obtained from the induced angle of attack on the position $y = 40\ cm$ for each geometric angle of attack, shown on Figure 56.
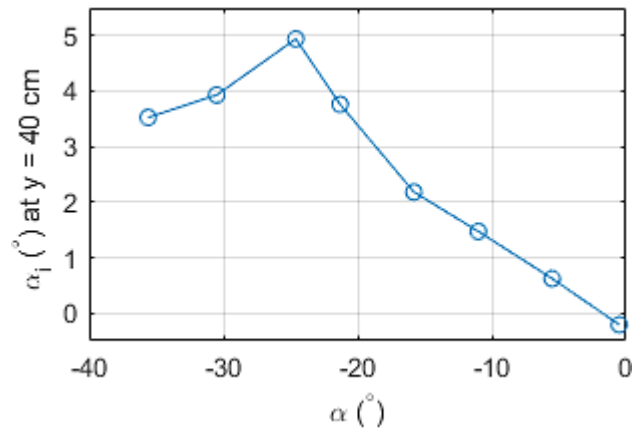
Figure 56. Distribution of induced angles of attack against the geometric angle of attack on the profile place at $y = 40\ cm$ obtained from Prandtl lifting line with method 2..

The corrected 2-dimensional lift and drag coefficient can be seen on Figure 57 and Figure 58, respectively, compared to the original ones. It is observed how the angles of attack are shifted to the right except for the highest α, thanks to the induced angle of attack. The more the distance between a certain angle and α_{L0} is, the larger the shift is. For the highest angle of attack that initially corresponds to $\alpha = -0.5$, as it is higher than α_{L0}, the shift is to the left, since the induced angles of attack are negative instead of positive due to the fact that the lift is positive. Apart from this shift, for all the angles, the value of the lift and drag coefficient varies thanks to the application of the equations that defines the change of axes.
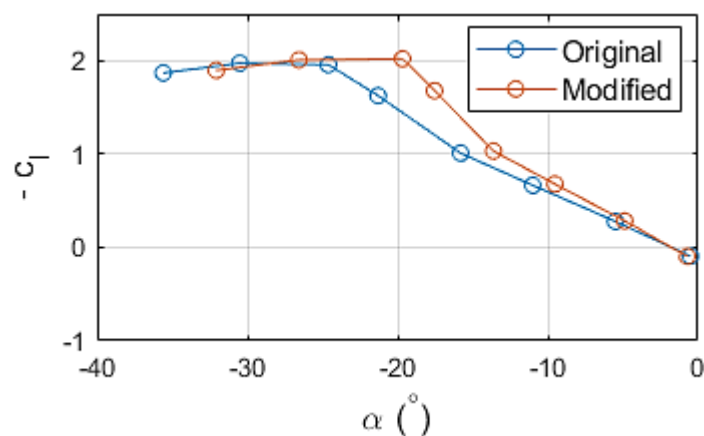
Figure 57. Corrected distribution of the 2-dimensional negative lift coefficient against α obtained from Prandtl lifting line with method 2 from original wind tunnel test for $U_\infty = 30\ m/s$.
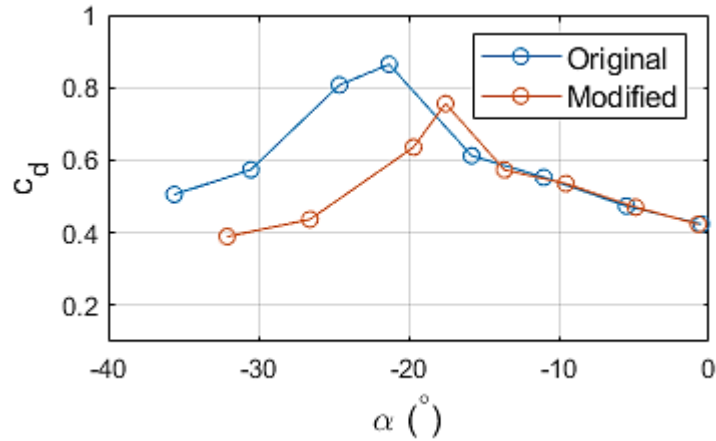
Figure 58. Corrected distribution of the 2-dimensional drag coefficient against α obtained from Prandtl lifting line with method 2 from original wind tunnel test for $U_\infty = 30\ m/s$.
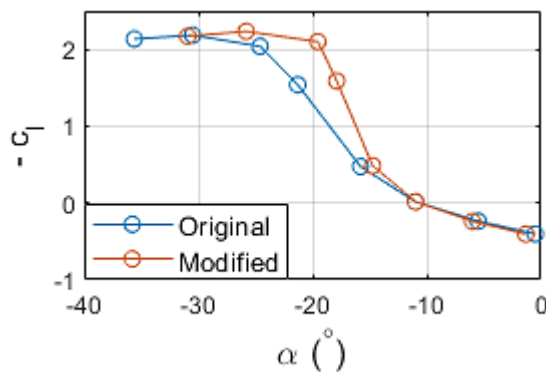
Figure 59. Corrected distribution of the 2-dimensional negative lift coefficient against α obtained from Prandtl lifting line with method 2 from original wind tunnel test for $U_\infty = 20\ m/s$
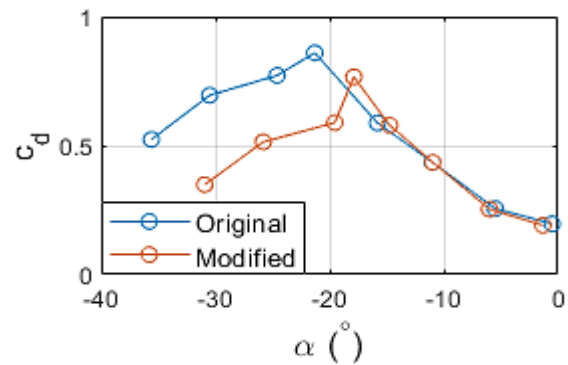
Figure 60. Corrected distribution of the 2-dimensional drag coefficient against α obtained from Prandtl lifting line with method 2 from original wind tunnel test for $U_\infty = 20\ m/s$.
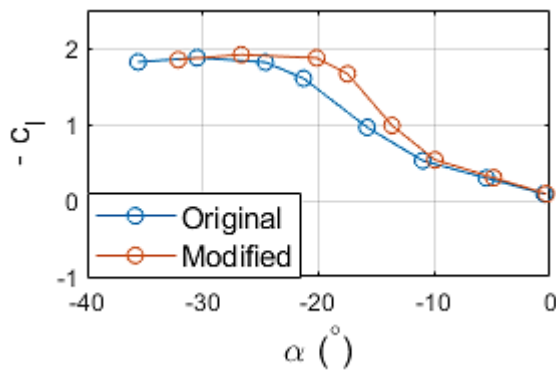
Figure 61. Corrected distribution of the 2-dimensional negative lift coefficient against α obtained from Prandtl lifting line with method 2 from original wind tunnel test for $U_\infty = 40\ m/s$
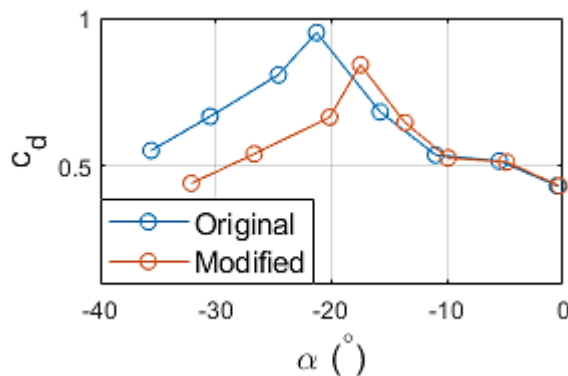
Figure 62. Corrected distribution of the 2-dimensional drag coefficient against α obtained from Prandtl lifting line with method 2 from original wind tunnel test for $U_\infty = 40\ m/s$.

As these corrected data is a more realistic approximation to a 2-dimensional behaviour. This same process, the method 2, in which the corrected data is obtained, is repeated with the velocities of $20\ m/s$ and $40\ m/s$ to use the corrected 2D coefficients later on the comparison with the numerical simulations and the 3D forces obtained to

select the optimum angles of attack on chapter 5. The results are shown on Figure 59 and Figure 60 for $20\ m/s$ and Figure 61 and Figure 62 for $40\ m/s$.

Both on the drag and lift cases, some deviations can be observed between the results predicted by the lifting line theory and the experimental ones. This difference is due to several reasons. On the first place, it is important not to forget that the Prandtl lifting line is based on a potential theory, so it does not consider the 3-dimensional effect of the viscosity. As, just like it has been seen before, for most of the angles of attack there is a detached boundary layer, the viscosity is greatly important on the study. The second deviation factor is found on the fact that the two-dimensional drag does not take into account the friction term. But, as the aileron belongs to the bluff bodies, the form drag is the dominant term and the contribution of the skin friction drag can be negligible. Another deviation factor, as it was anticipated, is the fact that the data used as two-dimensional, although they are a good approximation, they are influenced by three-dimensional effects. This has been tried to correct, but it is still an approximation.

Finally, there are a deviation related to the effect of the wing end plates. On one hand, the end plates have a contribution to the drag that is not considered here but is measured on the wind tunnel. On the other hand, even though the aspect ratio has been adjusted to take into account the effect of the plates, the correction applied is only an approximation where only the height of the plates has been taken into account while there are other parameters, as the form of the plate or the area of it that it places below or above the wing that, even though they are less important, they affect the aerodynamic performance of the wing.

Aileron with the car

Once the scope of the theory for the case of study is checked, the behaviour of the aileron when it is placed on the car is studied. In order to do that, the deflection angle induced by the car on the flow seen by the aileron has to be taken into account. This deflection angle, which has been previously obtained on the wind tunnel with a scale car, varies spanwise, so the angle of attack seen by each profile along the span is not constant, in contrast to the conditions studied on the wind tunnel. Inserting this angle called α_{car} into the formulation, and using the same sign criterion as for α_i, the effective angle becomes:

$$\alpha_{eff} = \alpha + \alpha_i + \alpha_{car} \tag{44}$$

And the fundamental equation becomes:

$$\alpha = \frac{2\Gamma(y_0)}{a_0 V_\infty c(y_0)} + \frac{1}{4\pi V_\infty} \int_{-\frac{b}{2}}^{\frac{b}{2}} \frac{\left(\frac{d\Gamma}{dy}\right) dy}{(y_0 - y)} + \alpha_{L0} - \alpha_{car} \tag{45}$$

$$\alpha = \frac{4b}{a_0 c(\theta_0)} \sum_{n=1}^{\infty} A_n \sin n\theta_0 + \sum_{n=1}^{\infty} n A_n \frac{\sin n\theta_0}{\sin \theta_0} + \alpha_{L0} - \alpha_{car} \tag{46}$$

The α_{car} distribution is obtained from the wind tunnel experiment performed with the scale car, of which results have been previously presented on section 3.2. Of the four series of data obtained at different Reynolds numbers, the one used is the one that corresponds to the highest Reynolds number, that is $Re_c = 2.86 \cdot 10^4$, as it is the closest one to the working Reynolds number, $Re = 3.38 \cdot 10^5$. It is obvious that some deviations due to the effect Reynolds are expected by using this data, but as there are little differences on Figure 33 with the Reynolds number and, at least the highest one is expected to be higher than the critical Reynolds number, this provides good expectations.

After having all the required information, the Prandtl lifting line is applied to some of the same angles of attack calculated previously on the wing without car. The range of geometric angles is smaller since, the deflection provoked by the car reduces the effective angle of attack, reaching the lower limit in which the theory is applied in this study for higher geometric angles of attack. The results obtained for the total lift coefficient and the drag coefficient are shown on Figure 63 and Figure 64. In addition, the lift-to-drag ratio is shown on Figure 65. Each of these results can be seen along with the results obtained on the previous section where the deflection angle induced by the car was not taken into account.
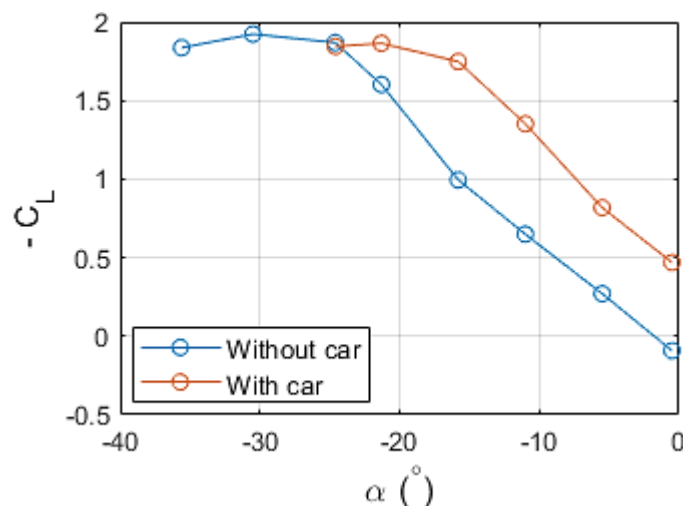
Figure 63. Comparison of the variation of the downforce with α obtained from Prandtl lifting line for the aileron with and without the car effect.

Regarding the variation of the lift coefficient with the angle of attack considering the effect of the car (orange line on Figure 63), it can be observed how it shifts to the right from the lift coefficient without the effect of the car (blue line). It makes sense as the effect of the car provokes that the angle of attack seen by the aileron was more negative than the geometric angle of attack. Together with this shitting effect, the form of the curve with the effect of the car is not exactly the same than the one without the car. This is due to the fact that α_{car} is not constant, so the angle of attack seen by each profile along the wing is not constant even without the effect of the induced angle of attack.
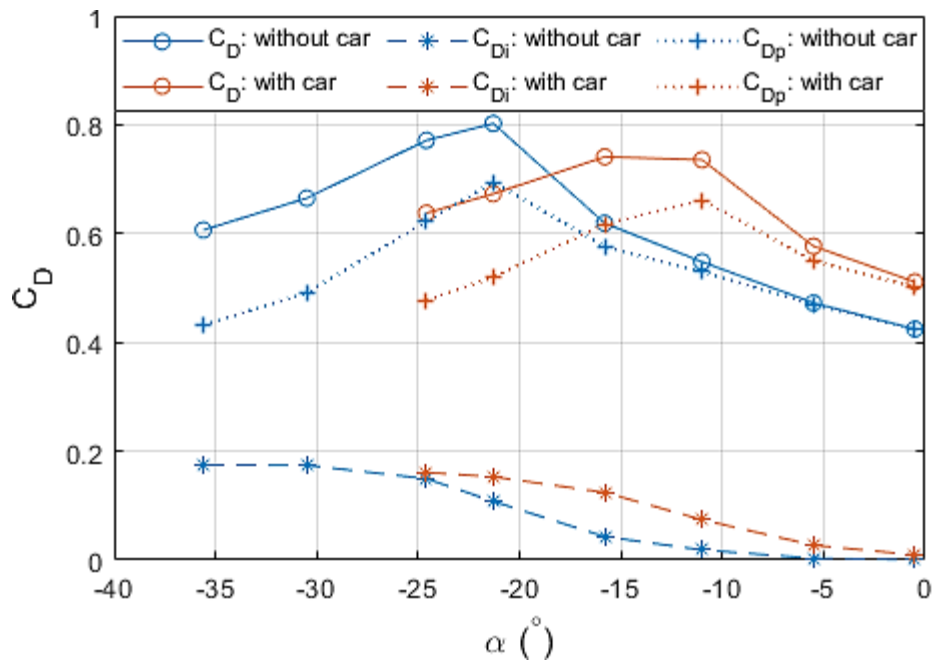
Figure 64. Comparison of the variation of the total drag and its components, profile and induced drag, with α obtained from Prandtl lifting line for the aileron with and without the car effect.

Regarding the variation of the drag coefficient the same effect is observed for all the contributions, profile and induced drag, and therefore, for the total drag too. Consequently, the variation of the lift-to-drag ratio has the same shift. This quantity, that is shown on Figure 65, rise almost constantly when the angle of attack decreases. This differs completely from the evolution of the 3D forces direct measured on the wind tunnel. This happens because of the deviations obtained with the theory from wind tunnel force experiment, especially for the drag, that were seen on the previous section on Figure 55.
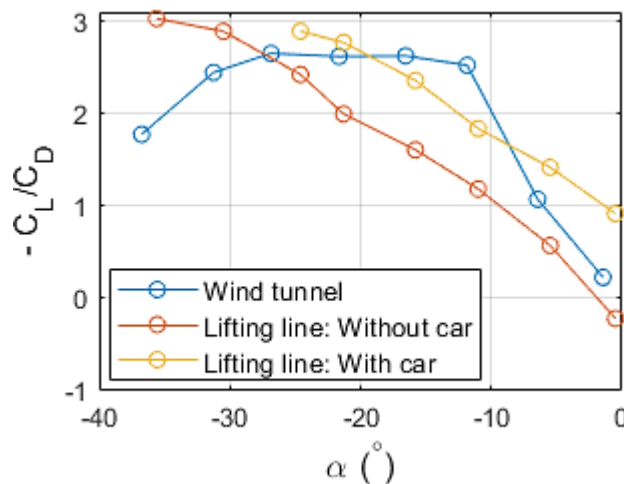
Figure 65. Comparison of the variation of the ratio of downforce to drag with α obtained from Prandtl lifting line for the aileron with and without the car effect and from the wind tunnel force experiment.

These discrepancies, probably, have their origins on the discrepancies between the 2-dimensional data used and the 3-dimensional results obtained from the wind tunnel. The most important one is the fact that the evolution of 2-dimensional drag is not constant at all while for the 3-dimensional drag it is almost a line. Even with the previously mentioned discrepancies that are transmitted to the final Prandtl lifting line results, what

can be concluded is that the effect of the car can be synthesise as a certain shift of about $+8°$. This is going to be discussed proximately on the chapter 5.

4. Numerical simulations results

Up to now, to study the two-dimensional profile of the aileron, the measurements obtained from the pressure wind tunnel test have been used. But, as it was explained previously, these measurements, even though they are performed on a 2D profile, are affected by the three-dimensional flow. These measurements have been tried to correct by means of the Prandtl lifting line theory, but they still differ from real 2D data. This is why the 2D profile of the aileron is studied with numerical simulations.

The results obtained from the numerical simulations are presented and compared to the results obtained from the wind tunnel on this chapter. To make the comparison, the wind tunnel data corrected with the induced angles obtained with the Prandtl lifting line theory are used. Once the numerical results are compared with the wind tunnel data and the differences between both are studied, they are used to analyse the behaviour of the flow around the airfoil.

The chapter is divided into two sections. On the first one a study on the Reynolds effect is done. On the second one, the airfoil is studied for different angles of attack.

4.1. Reynolds effect study

In order to study the Reynolds effect, simulations with several velocities at the angle of attack of reference, that is $\alpha = -30.5°$, are performed. As the maximum velocity reach by the Evo 2 Fun Cup is of around $200\ km/h$, that is $55.6\ m/s$, and taking into account the velocities at which the experiments were performed, a total of 4 velocities are simulated in a range from $20\ m/s$ to $50\ m/s$.

The results obtained from the simulations with a free stream velocity of $20\ m/s$, $30\ m/s$ and $40\ m/s$ are compared to the ones of the wind tunnel pressure test. In order to do that, the corrections made with the Prandtl lifting line theory to the experimental bidimensional information are used (figures 49 - 54). After this comparison, the Reynolds effect on the flow behaviour is studied from the velocity field of the numerical results.

4.1.1. Comparison with experimental results

Before making the comparison between numerical and experimental results, it is important to reconsider the differences between both. The first difference lies on the frictional part of bidimensional forces. As the bidimensional aerodynamic forces obtained on the wind tunnel were obtained from pressure measurements, the frictional part of the

forces is not considered. This could lead to differences, especially on the drag, with the numerical results, that takes into account this term. But, as it was explained before, since the shape of the wing is not streamlined, the frictional term is expected to be negligible. This is checked with the numerical results. Comparing the skin friction drag to the total drag, it was obtained that this term is not higher than a 1% for any of the velocities with any of the two models used. So, it is going to be considered as negligible.

The second difference comes from the three-dimensional effects on the wind tunnel experiment that are not corrected with the Prandtl lifting line. Especially those that can affect to the boundary layer behaviour and, therefore, to the position on the detachment of the flow, that is highly expected due to the profile shape. Moreover, there is not only the three dimensional effect of a rectangular wing, but also the end-plates, the frame of the aileron and the bulges of the wing used for jointing it with the frame can affect the flow seen by the measured profile.

On Figure 66 and Figure 67, the bidimensional forces coefficients obtained from the wind tunnel and the ones obtained with the two numerical models are shown. Regarding the lift coefficient, some differences, as expected, can be observed with both methods, especially for $20 \, m/s$, but the order of magnitude is similar. In general, none of the methods predicted the same evolution with the Reynolds effect, as the one obtained on the wind tunnel tests. This is not what happens regarding the drag, where with the numerical solution the drag obtained is of around the double of the one obtained experimentally. In order to examine the origin of this huge discrepancy, the pressure distribution is obtained.
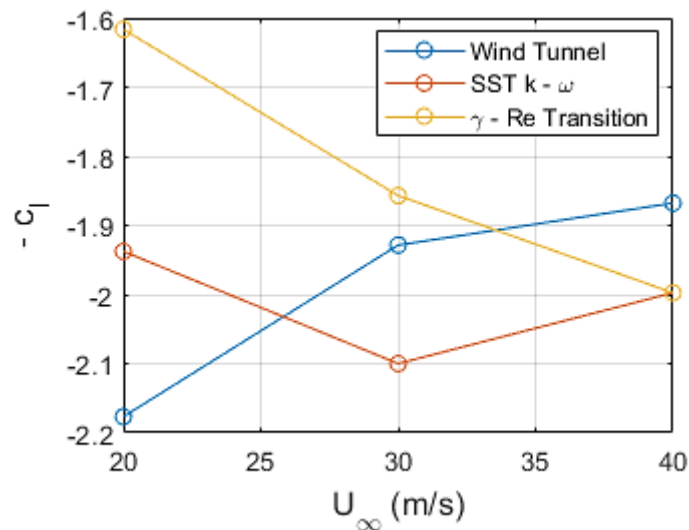
Figure 66. Comparison of the Reynolds effect on 2D negative lift coefficient at $\alpha = -30.5°$ between the wind tunnel pressure test results and the results obtained from simulations with the two numerical methods.
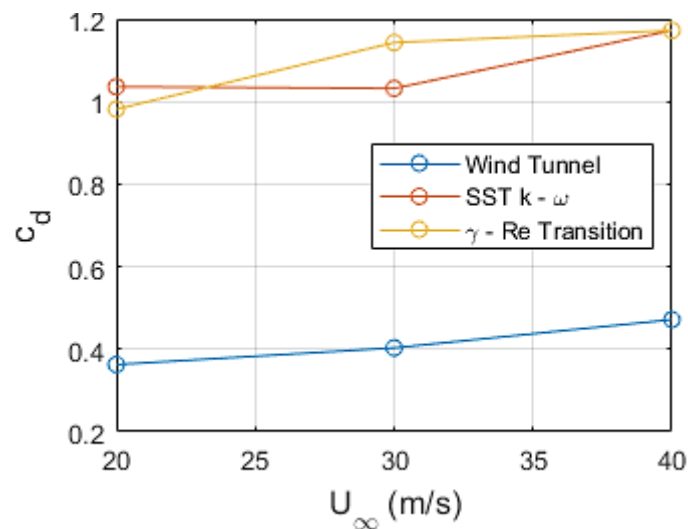
Figure 67. Comparison of the Reynolds effect on the 2D drag coefficient at $\alpha = -30.5°$ between the wind tunnel pressure test results and the results obtained from simulations with the two numerical methods.

The pressure distribution of both numerical simulations and wind tunnel tests are shown on Figure 68, Figure 69 and Figure 70 for a free stream velocity of $20\ m/s$, $30\ m/s$ and $40\ m/s$, respectively. It is important to remark that the angle of attack of each set of measurements is referred to the effective angle. Consequently, in the case of the wind tunnel results they take into account, in addition to the geometric angle, the induced angle of attack obtained from the Prandtl lifting line theory. Even though the measurements were done at the same geometric angle of attack for the three velocities, as the induced angle depends on the velocity, it can be observed how the angle is not the same in the three cases.
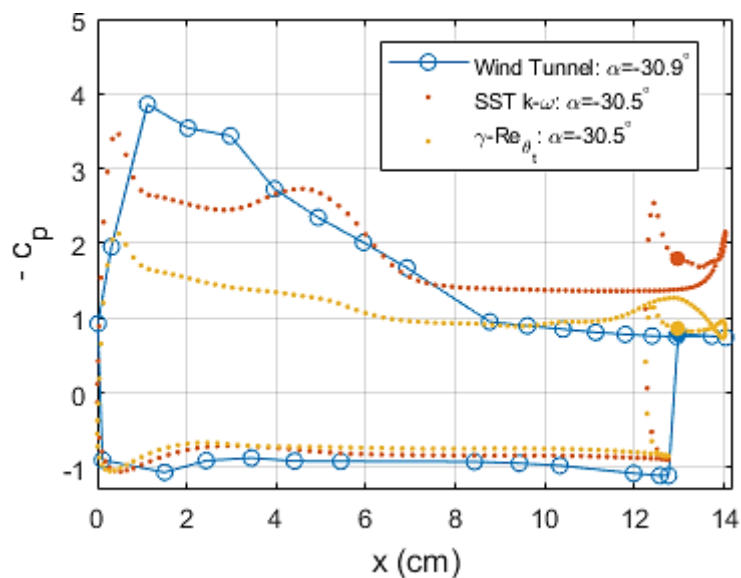
Figure 68. Comparison of the pressure coefficient distribution at $\alpha = -30.5°$ and $U_\infty = 20\ m/s$ between the wind tunnel pressure test results and the results obtained from simulations with the two numerical methods.

As for $U_\infty = 20\ m/s$, the effective angle of the measurement done at a geometric angle of mattáck of $-35.6°$ is almost the same than the one of the numerical simulations, they can be compared directly. However, for $U_\infty = 30\ m/s$ and $U_\infty = 40\ m/s$, the

effective angle for this measurement differs with respect to the one of the simulations on 1.6°, so the next effective angle is plotted too for a better comparison.
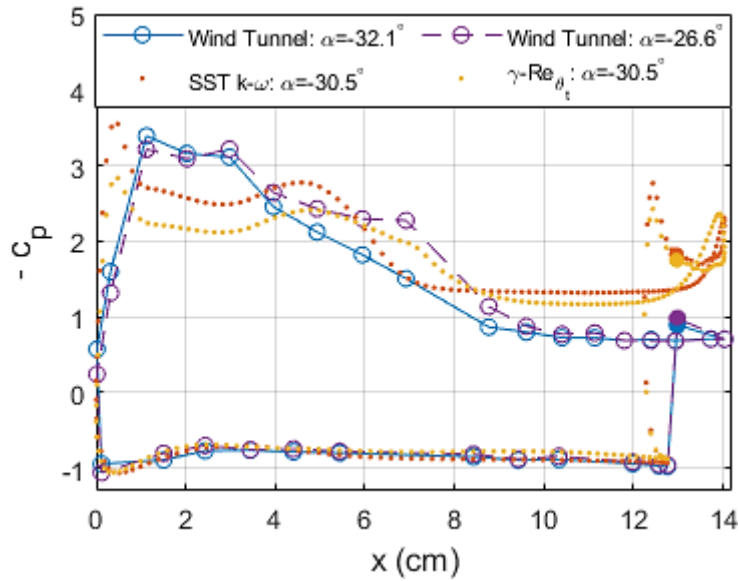
Figure 69. Comparison of the pressure coefficient distribution at $\alpha = -30.5°$ and $U_\infty = 30\ m/s$ between the wind tunnel pressure test results and the results obtained from simulations with the two numerical methods.
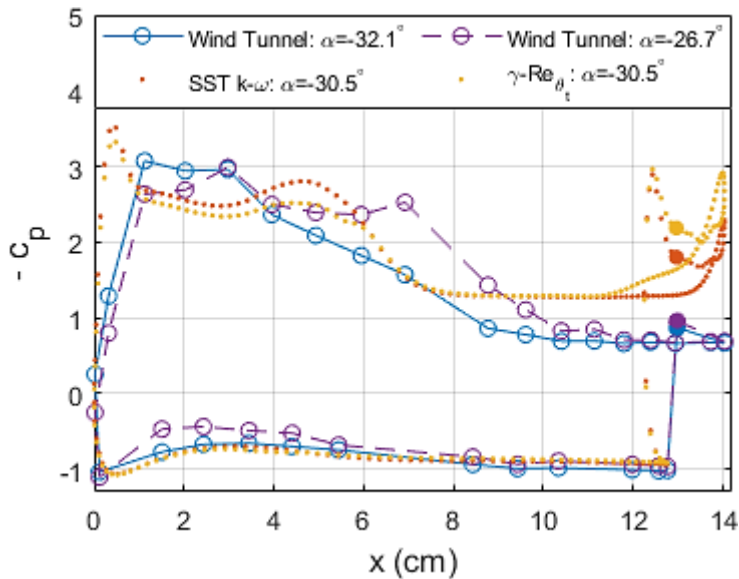
Figure 70. Comparison of the pressure coefficient distribution at $\alpha = -30.5°$ and $U_\infty = 40\ m/s$ between the wind tunnel pressure test results and the results obtained from simulations with the two numerical methods.

For the three velocities and the two numerical methods, some similarities on the comparison are found, with the exception of the $\gamma - Re$ Transition method for a free stream velocity of $20\ m/s$, that will be analysed separately. For all of them the pressure coefficient on the pressure side, which is the upper surface, is almost the same numerically and experimentally up to the tap immediately before to the trailing edge tap (tap 2 and tap 1 respectively). The higher difference is found for $20\ m/s$ where, even though the evolution is the same on the three cases (the two numerical models and the experimental results), there is a little step between the numerical results and the experimental one. The zone of the trailing edge will be analysed afterwards.

Regarding the suction side (lower side), what happens is completely different. The shape of the pressure distribution obtained numerically differs considerably from the one of the wind tunnel tests. On the first place, there is a suction peak on the numerical pressure coefficients at the leading edge that on the experimental distribution takes place afterwards and is less pointed as the pressure remains, in general, constant after the peak for the experimental pressure coefficient. On the mid zone of the profile, the numerical solutions and the experimental one are more similar on values, but the evolutions are not the same. The biggest difference comes after that. On the second half of the profile there is an almost constant zone that numerically takes place at a considerably lower pressure coefficient than experimentally.

After the constant zone on the suction side, the trailing edge zone is placed. For both sides, upper and lower ones, on the trailing edge the pressure coefficient is completely different between the numerical solution and the experimental one. A part of this difference can not be analysed properly, as there is a lack of pressure taps on this zone on the wind tunnel tests, caused by the shape of the aileron in this zone that limits the amount of pressure taps. This lack of taps affects especially to the upper side, were there is a suction peak measured numerically whose existence can not be assessed experimentally as there is no tap in this zone. But, apart from this, some differences are obvious. The pressure coefficient on the trailing, that is, the points highlighted with a coloured circle, is considerably lower numerically than experimentally. Moreover, on the suction side, before the trailing edge there is a decrease on the pressure that does not take place on the experimental distribution.

Finally, the Transition model for $20\,m/s$ has to be analysed. The pressure side behaviour is similar to the rest of the cases. Nervertheless for the suction side, unlike the other cases, this time the biggest disagreement is found on the first mid of the profile. This change on the behaviour does not seem realistic, so the explanation could be found on a bad behaviour of the model for this case.

To sum up, generally, the behaviour of the flow on the pressure side is almost the same with simulations than with experiments, while the behaviour on the suction side differs considerably, especially on the trailing edge. At this point, it is important to remark that both the end-plates and the frame are placed on the suction side. This could explain a big part of the disagreement found on this side of the aileron.

Coming back to the analysis of the huge disagreement on the drag coefficients, it can be observed that its origin is the trailing edge. The pressure on the zone around the trailing edge acts mostly horizontally. This explains that the differences on the lift coefficients are considerably smaller than the differences on the drag coefficients, since the mid zone, which is the higher contributor to the lift, is the zone where numerical and experimental results are more similar. Furthermore, it is important to remember that the 2D drag coefficient obtained from the pressure test does not fit with the 3D drag coefficient. In fact, with the Prandtl lifting line the 3D lift coefficient is approximated correctly, while the results for the 3D drag coefficients are really bad. This means that the experimental 2D drag coefficient is not really trustworthy.

Regarding the comparison between the two methods, excepting the case of $20\,m/s$ in which the $\gamma - Re$ Transition method differs from the rest of the results, both methods give a similar solution. The biggest differences are found, again, on the suction side, with

small steps, in the first mid for $U_\infty = 30\ m/s$ and in the zone of the trailing edge for $U_\infty = 40\ m/s$. Since in both cases these differences are small enough, and considering the commented disagreement on $20\ m/s$ of the $\gamma - Re$ Transition model, the SST $k - \omega$ model is used on the next section to analyse the flow,

4.1.2.   Flow behaviour

After comparing the results of the simulations for different free stream velocities with the results obtained from the wind tunnel experiments, the behaviour of the flow is analysed by its velocity field. But, before that, as on the previous figures all the pressure coefficients distribution at different velocities seem to be very similar, the ones obtained with the SST $k - \omega$ model are plotted all together (including now the one of $U_\infty = 50\ m/s$) on Figure 71. It can be observed that there is not a big variation. The highest difference is on the suction side on the second mid, where in the constant part the pressure rises with the velocity.
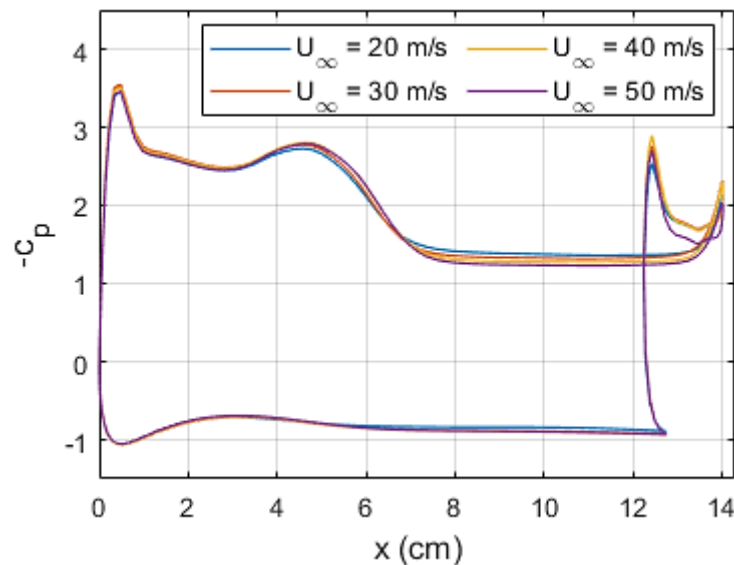
Figure 71. Reynolds effect on the pressure coefficient distribution at $\alpha = -30.5°$ obtained with the numerical model SST $k - \omega$.

As the differences are so small, only the velocity field of the two extreme cases for SST $k - \omega$ model, $U_\infty = 20\ m/s$ and $U_\infty = 50\ m/s$ are analysed, as the rest are almost the same. The velocity field of the simulations performed with the $\gamma - Re$ Transition model are shown on the Appendix I.

Observing the Figure 72 and the Figure 73, it can be observed how both velocity fields are almost the same. It is important to remark that the fields correspond to a particular time instance. In both cases, the flow is accelerated on the suction side from the stagnation point to a velocity of around twice the free stream one. After that, the flow separates due to the high adverse pressure gradient. On the pressure side, the flow separates rapidly and reattaches afterwards near the trailing edge, generating a recirculation burble. After that, on the trailing edge the flow accelerates, reaching again a velocity of twice the free stream one, and separates again due to the strong curvature

of the wing. This generates shedding vortices, characteristic of the bluff bodies, that lead to a high drag force and a lower lift. These vortices shed periodically leading to unsteady aerodynamic forces.

Regarding the differences between the flow with $U_\infty = 20\ m/s$ and $U_\infty = 50\ m/s$, they are anecdotic. The recirculation zone seems to be a little more extensive for $20\ m/s$. And on the trailing edge acceleration of the flow is higher for $20\ m/s$ too.
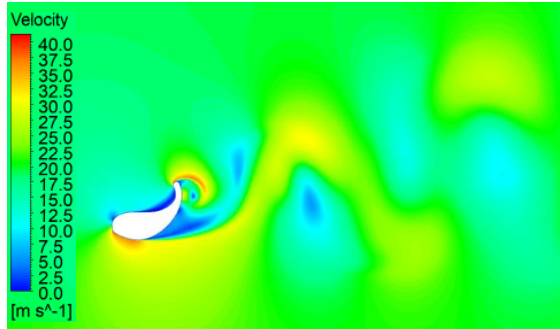
Figure 72. Velocity field in a particular time instance obtained with the numerical model SST $k - \omega$ at $\alpha = -30.5°$ and $U_\infty = 20\ m/s$.
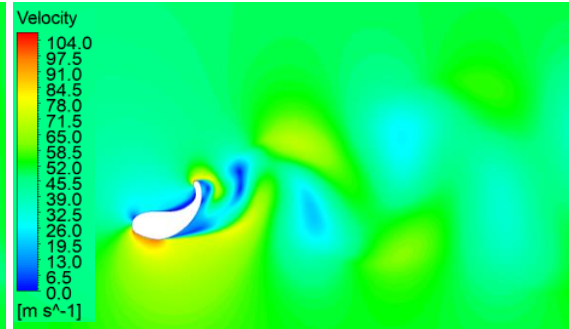
Figure 73. Velocity field in a particular time instance obtained with the numerical model SST $k - \omega$ at $\alpha = -30.5°$ and $U_\infty = 50\ m/s$.

4.2. Angle of attack effect study

Once the Reynolds effect is studied, the next step is to study how the angle of attack affects the performance of the aileron, as it was done experimentally. This analysis is done at $40\ m/s$ and for 6 different angles of attack from $-35.5°$ and $-10.5°$ each 5°. Just like in the previous section, first the numerical simulations are compared with the corrected wind tunnel results, and then the behaviour of the flow is analysed.

In addition, once the variation of the lift and drag coefficient is obtained, the Prandtl lifting line can be used as it was previously used with the experimental bidimensional data. But this time, no correction of the bidimensional information is needed as the study is actually bidimensional in contrast to the experimental one.

4.2.1. Comparison with experimental results

Before starting the comparison, it is important to check the importance of the skin friction drag obtained with the simulations performed at different α. Since, again, the skin friction drag is not higher than a 1% of the total drag for any of the simulations, it is still considered negligible.

On Figure 74 and Figure 75 the 2D lift coefficient and the 2D drag coefficient obtained from the wind tunnel experiment and from the two numerical models are shown. Again, numerical and experimental results are more or less similar for the lift coefficient and differ completely for the drag coefficient. The lift coefficients are very similar with the

exception of the two highest angles of attack, $\alpha = -15.5°$ and $\alpha = -10.5°$, where the numerical downforce is higher than the experimental one. For the drag, the only α at which numerical and experimental results are similar is $\alpha = -20.5°$, but having a look to the rest angles, it is clear that is merely incidental, as the evolution of the drag between the numerical models and the experimental one does not correlate at all.
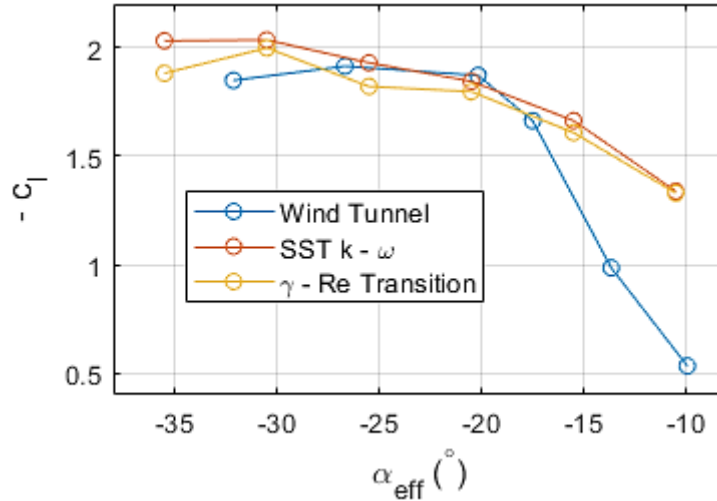
Figure 74. Comparison of the variation of the 2D negative lift coefficient with α at $U_\infty = 40 \, m/s$ between the wind tunnel pressure test results and the results obtained from simulations with the two numerical methods.
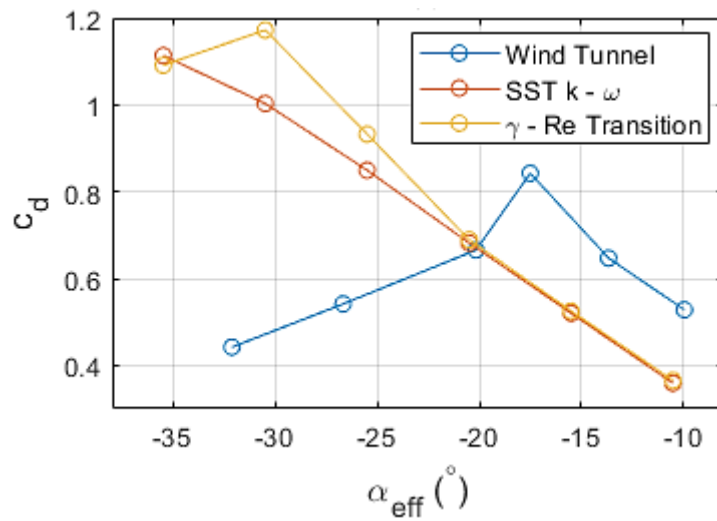
Figure 75. Comparison of the variation of the 2D drag coefficient with α at $U_\infty = 40 \, m/s$ between the wind tunnel pressure test results and the results obtained from simulations with the two numerical methods.

Once more, the pressure coefficient distributions are used to take a look into the commented disagreements in more detail. The pressure coefficient for all the angles of attack are shown on Figure 76 – Figure 80, with the exception of $-30.5°$ that has already been examined on Figure 70. On Figure 76, the pressure distribution is shown for the simulation performed at $\alpha = -35.5°$. It is important to remark that for this blue set of points the effective angle of attack is unknown, so the angle in the legend corresponds to the geometric one. The effective angle of attack should be smaller than the geometric one. The analysis for this angle is almost the same that the one for $\alpha = -30.5°$. The two highest differences are that the peak for the simulations this time is bigger, so it differs

more from the wind tunnel results, and that the two sets of the experiments are totally different, making more difficult a precise analysis.

Figure 76. Comparison of the pressure coefficient distribution at $\alpha = -35.5°$ and $U_\infty = 40\ m/s$ between the wind tunnel pressure test results and the results obtained from simulations with the two numerical methods.

On Figure 77 and Figure 78 the results for $\alpha = -25.5°$ and $\alpha = -20.5°$ are shown, respectively. Both angles are very similar. Again, the analysis for the pressure side is the same than previously. The analysis for the suction side is more or less the same too, but this time the differences are a little more remarkable on the mid zone than before.

Figure 77. Comparison of the pressure coefficient distribution at $\alpha = -25.5°$ and $U_\infty = 40\ m/s$ between the wind tunnel pressure test results and the results obtained from simulations with the two numerical methods.

Figure 78. Comparison of the pressure coefficient distribution at $\alpha = -20.5°$ and $U_\infty = 40\ m/s$ between the wind tunnel pressure test results and the results obtained from simulations with the two numerical methods.

Finally, on Figure 79 and Figure 80, the distributions for the last two angles are shown. This time the comparison differs from the previous ones. The pressure on the pressure side is no longer the same between experimental and numerical results, especially on the last case. And this time, the differences on the suction side are much smaller. Mainly, on the leading edge, where the higher difference is the one due to the lack of points of the wind tunnel test.
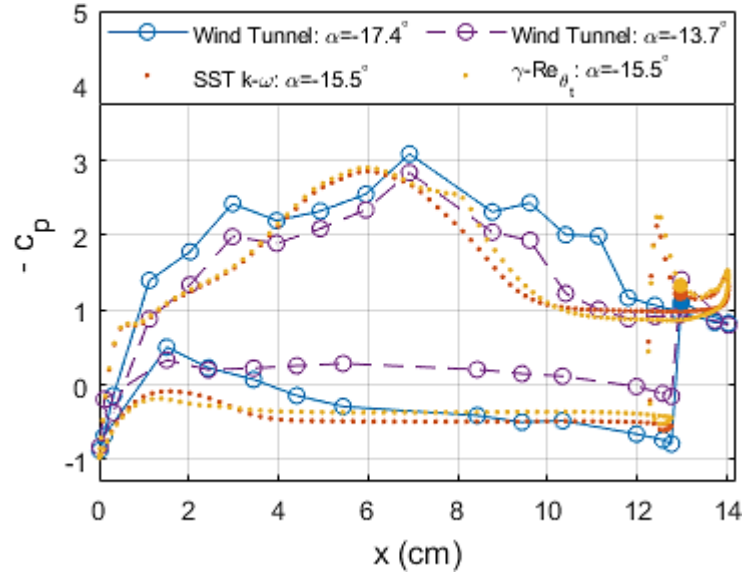
Figure 79. Comparison of the pressure coefficient distribution at $\alpha = -15.5°$ and $U_\infty = 40\ m/s$ between the wind tunnel pressure test results and the results obtained from simulations with the two numerical methods.
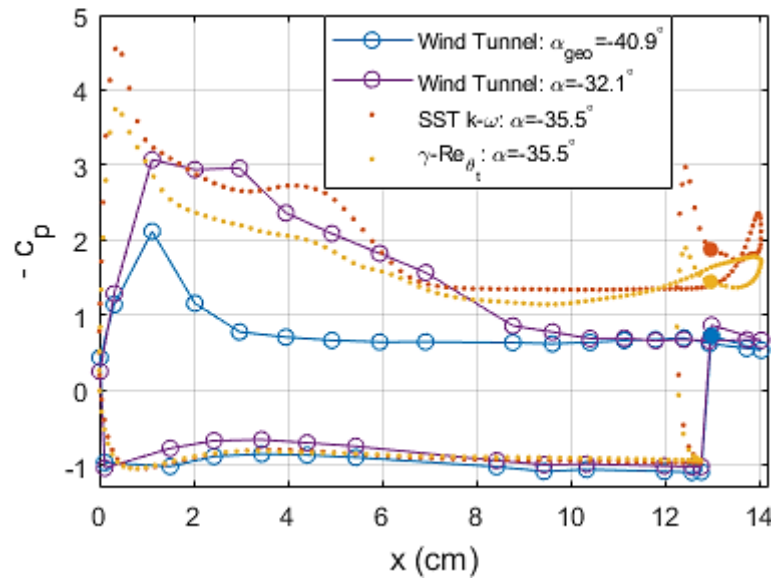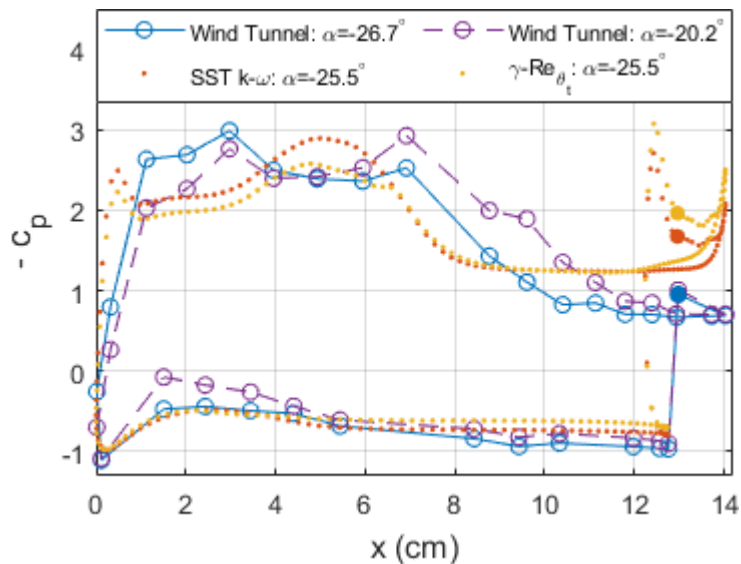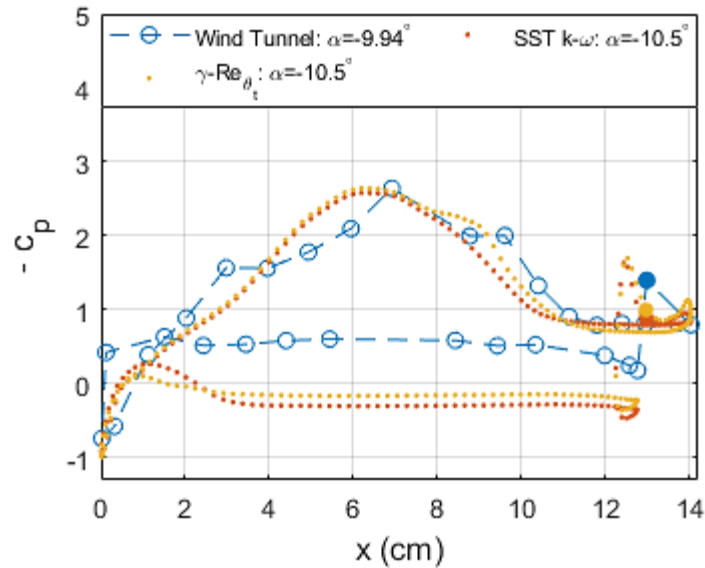
Figure 80. Comparison of the pressure coefficient distribution at $\alpha = -10.5°$ and $U_\infty = 40\ m/s$ between the wind tunnel pressure test results and the results obtained from simulations with the two numerical methods.
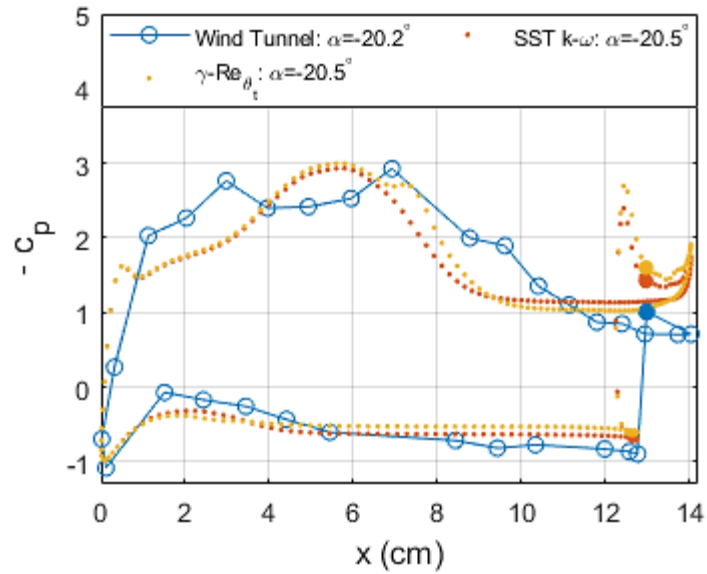
Regarding a comparison between the two numerical methods, in general, the results for the pressure side are the same and the ones of the suction side are very similar but with small deviations. These differences on the suction side are more noticeable for $\alpha = -35.5°$ and decrease when the angle of attack increases. While for the pressure side, a small step appears from $\alpha = -20.5°$, that increases when α increases too. Once again, given the similarities, the SST $k - \omega$ model is used on the next section to study the evolution on the behaviour of the flow.

4.2.2.   Flow behaviour

Again, all the pressure coefficients are plotted together to analyse how they vary with the angle of attack (Figure 81). This time, the variation between the different simulations is significant, in contrast to the results of the Reynolds effect. So, in general, the Reynolds effect on the measured range can be considered negligible comparing to the effect of the angle of attack.

Regarding the pressure side, after the initial rise of pressure coefficient up to 1, there is a decrease that is higher when the angle of attack rises (decreases in terms of the absolute value). After that, the pressure becomes constant and, again, decreases with the angle of attack. Regarding the suction side, the lower the α is, the more noticeable the suction peak of the trailing edge is. This peak disappears for the two biggest α, $-15.5°$ and $-10.5°$. When the angle of attack rises, the second peak, which appears on the mid part of the chord, takes place later in terms of the chord of the airfoil. Finally, on the second mid of the profile, the pressure is higher when the α is higher too.
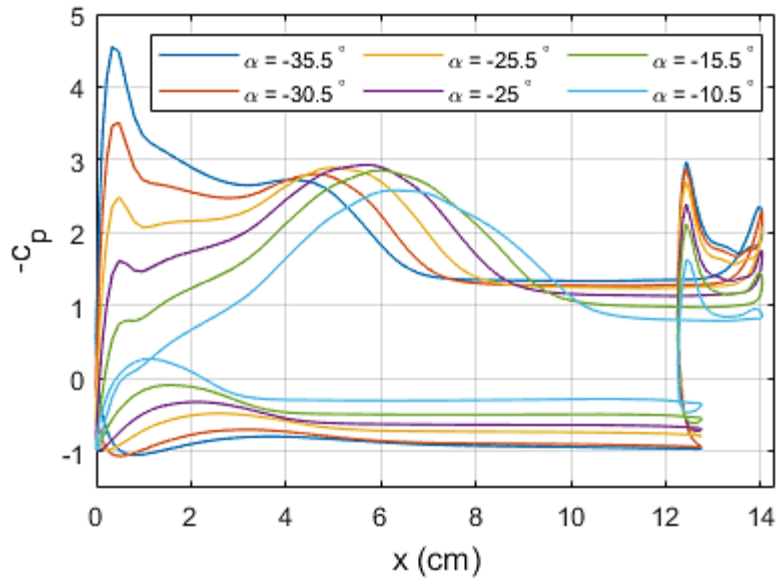
Figure 81. Effect of the angle of attack on the distribution of the pressure coefficient for a free stream velocity of $40 \, m/s$ obtained with the numerical model SST $k - \omega$.

On the Figure 82 – Figure 87 the velocity field of each simulation is shown. All the velocity fields have a similar appearance, but some differences can be appreciated. Firstly, the extension of the recirculation zone on the pressure side increases progressively when the angle of attack increases too. Secondly, with regard to the separation point of the suction side, there is a progressive delay with the rise of α. Finally, having a look to the wake, it can be observed how the height of the called Kármán vortex street becomes thinner with the increase of the angle of attack.
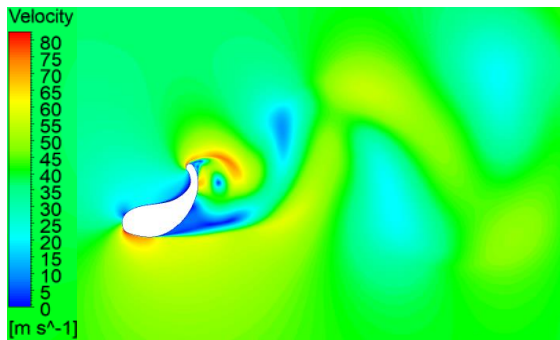
Figure 82. Velocity field in a particular time instance obtained with the numerical model SST $k - \omega$ at $\alpha = -35.5°$ and $U_\infty = 40 \, m/s$.
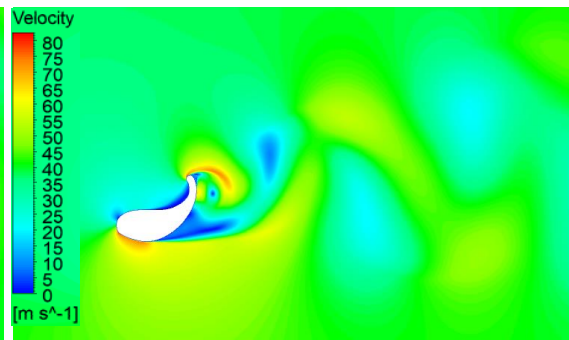
Figure 83. Velocity field in a particular time instance obtained with the numerical model SST $k - \omega$ at $\alpha = -30.5°$ and $U_\infty = 40 \, m/s$.
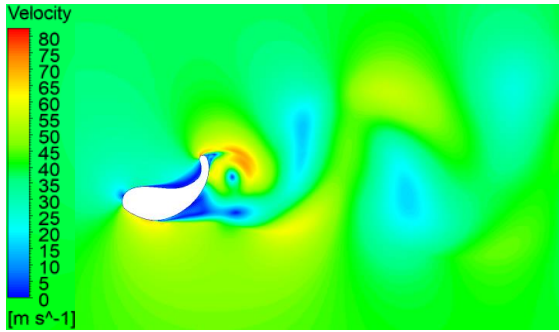
Figure 84. Velocity field in a particular time instance obtained with the numerical model SST $k - \omega$ at $\alpha = -25.5°$ and $U_\infty = 40\ m/s$.
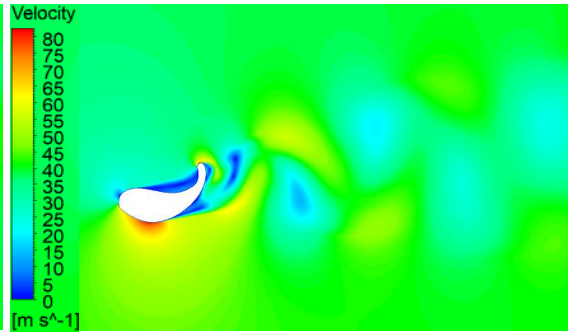
Figure 85. Velocity field in a particular time instance obtained with the numerical model SST $k - \omega$ at $\alpha = -20.5°$ and $U_\infty = 40\ m/s$.
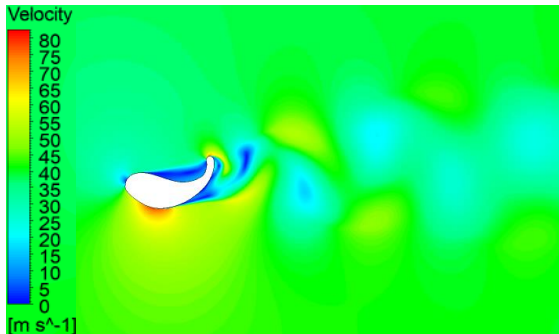
Figure 86. Velocity field in a particular time instance obtained with the numerical model SST $k - \omega$ at $\alpha = -15.5°$ and $U_\infty = 40\ m/s$.
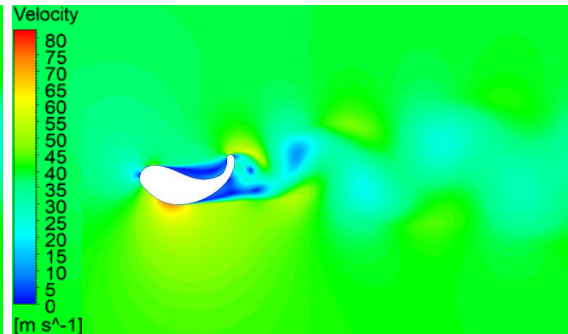
Figure 87. Velocity field in a particular time instance obtained with the numerical model SST $k - \omega$ at $\alpha = -10.5°$ and $U_\infty = 40\ m/s$.

4.2.3.   Prandtl lifting line
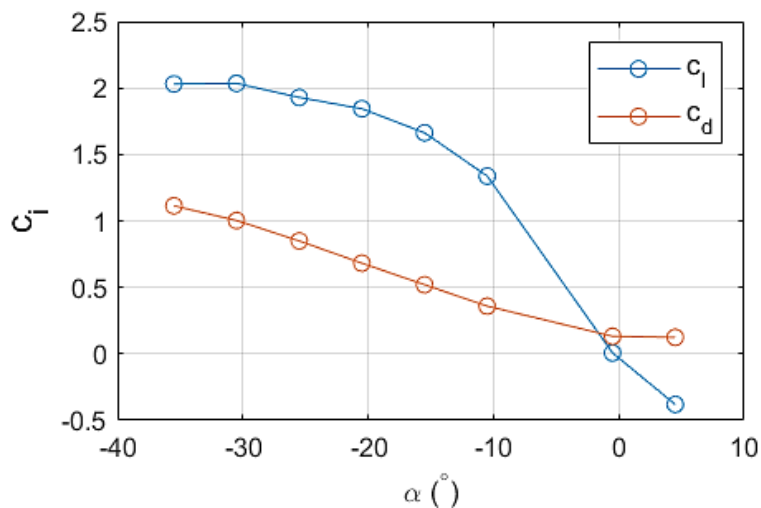
Figure 88. Variation of the 2-dimensional negative lift coefficient and drag coefficient with the angle of attack obtained with numerical simulations for $U_\infty = 40\ m/s$.

As a new set of 2-dimensional lift coefficient and drag coefficient is achieved, the Prandtl lifting line can be used again to get a new set of 3D forces. Again, the results of the SST $k - \omega$ model are used. This time, no correction on the 2-dimensional forces is

needed, so only the called method 1 is used. Since the range of α studied with the simulations does not covers the zone of zero lift, two additional simulations, at $\alpha = -0.5°$ and $\alpha = 4.5°$ are performed to obtain the angle of zero lift. On Figure 88 the lift coefficient and the drag coefficient with these additional two points are shown.

Aileron without car

Again, first the aileron is studied without the effect of the car, that is, with a uniform free stream. On Figure 89, Figure 90 and Figure 91 the 3D drag, the negative lift and the lift-to-drag ratio coefficients are shown for both the Prandtl lifting line perform from the wind tunnel pressure test and the one performed from the numerical simulations results.

Regarding the lift, the solutions obtained from the pressure test and the numerical simulations are very similar, as it happens with on the comparison of the 2D lift coefficient. Regarding the drag coefficient, as it was expected the results are very different. The drag coefficient obtained with the Prandtl lifting line from the wind tunnel 2D lift coefficients has a maximum at around $\alpha = -20°$, while on the one obtained from the simulations the drag rises continually when α decreases. Finally, with regard to the ratio of the downforce to drag coefficients, the opposite happens. This time, it is the result obtained from the simulations the one that has a maximum whereas the one obtained from the wind tunnel rises when α decreases.
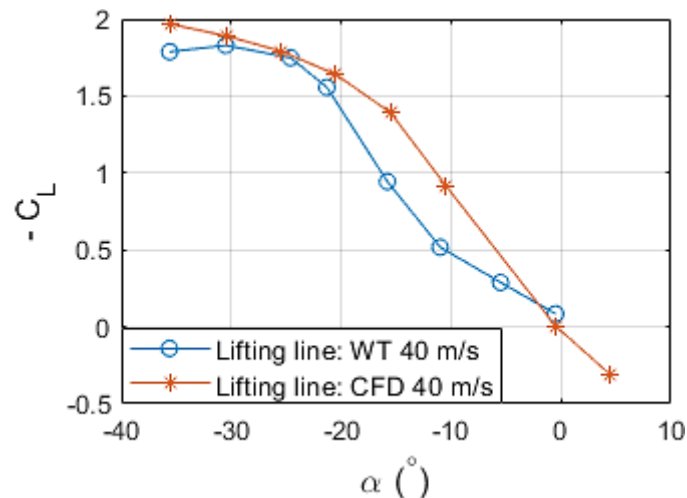
Figure 89. Variation of the negative lift coefficient with α for the aileron without the car effect. Comparison between results obtained with the Prandtl lifting line from the pressure test wind tunnel results and from numerical simulations results.
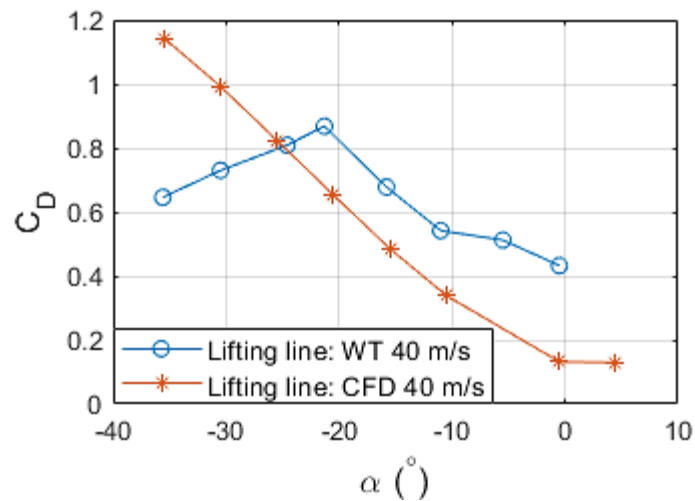
Figure 90. Variation of the drag coefficient with α for the aileron without the car effect. Comparison between results obtained with the Prandtl lifting line from the pressure test wind tunnel results and from numerical simulations results.
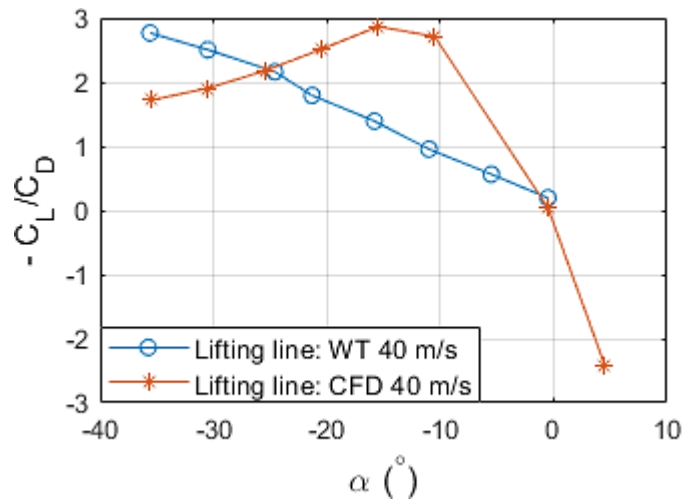
Figure 91. Variation of the ratio of lift to drag coefficients with α for the aileron without the car effect. Comparison between results obtained with the Prandtl lifting line from the pressure test wind tunnel results and from numerical simulations results.

Aileron with car

Repeating the process followed with the wind tunnel results, now, the α_{car} obtained on a wind tunnel test is used for modifying the flow seen by the aileron. The solution obtained for the lift coefficient, the drag coefficient and the lift-to-drag ratio are shown, respectively, on Figure 92, Figure 93 and Figure 94. As it was observed previously, the effect of the car on the lift and drag coefficients can be seen, in a first approximation, as a shift, this time of about 7.5°, to the right on the angles of attack. Apart from this behaviour, on the negative lift coefficient for the lowest angles of attack it can be observed how the downforce decreases and the shape of the curve achieves a maximum that was non-existent for the one without car.
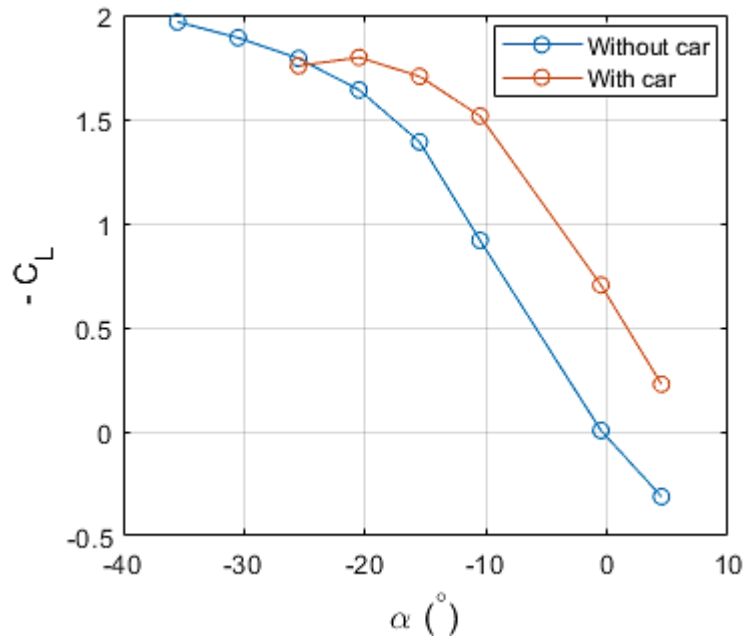
Figure 92. Comparison of the variation of negative lift coefficient with α obtained from Prandtl lifting line performed from numerical results for the aileron with and without the car effect.
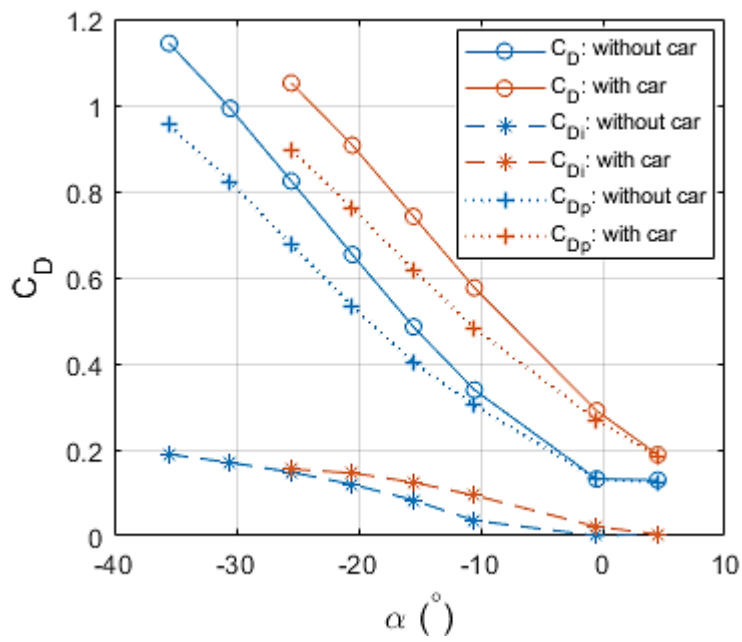
Figure 93. Comparison of the variation of the total drag and its components, profile and induced drag, with α obtained from Prandtl lifting line performed from numerical results for the aileron with and without the car effect.
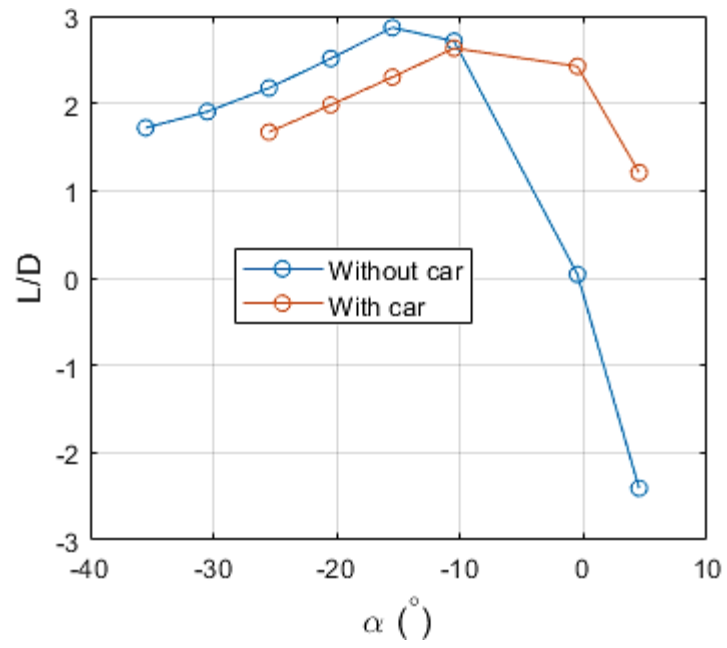
Figure 94. Comparison of the variation of the ratio of downforce to drag with α obtained from Prandtl lifting line performed from numerical results for the aileron with and without the car effect.

5. Discussion

Up to now, the results of the different experiments and numerical simulations have been presented and analysed, but, which is the angle of attack that optimizes the performance of the car? It seems to be a quite simple question, but there is not an unique answer. As it was explained on the introduction, on the aerodynamics of a race car there are two opposed requirements: to maximize the downforce and to minimize the drag. So, normally, there is a trade-off between these two requirements. This leads to the first objective which is analysed in this report, that is to maximize the lift-to-drag ratio, or what is the same the ratio of lift coefficient to drag coefficient.

But, apart from this compromise, there are some situations in which one of the requirements prevails over the other one. This leads to the second and third objective that are the two extreme cases, that is, to maximize the downforce and to minimize the drag, respectively. Besides these three objectives studied on this report, there are an infinity of them between the two extreme cases, depending on the specific desired performance on the car. This desired performance depends on the specific circuit and it is influence by other aspects of the car that are not considered in this project.

Since the motive of these objectives is to improve the performance of the car, it would be logical to only consider the results that take into account the effect of the car on the flow upstream the aileron. But, as the evolution of the forces with and without the aileron are similar, the study of the optimum α of the wing isolated could be interesting afterwards, so the chapter is divided into two sections. A first section that includes all the results in which the free stream is uniform, that is, the wing is isolated. And a second one that includes only the results in which the effect of the car is considered by the vertical deflection generated.

5.1. Optimization of the aileron isolated

On this section, the angles of attack that better fit each one of the three objectives stablished are obtained, based on all the previous results that involve the aileron isolated, that is, with uniform free stream conditions. The word isolated refers to the fact that the aileron is not placed on the car, so the free stream conditions are uniform. These three objectives are:

- Objective #1. To maximize the lift-to-drag ratio.

- Objective #2. To maximize the downforce.

- Objective #3. To minimize the drag.

Taking into account the errors accumulated and the fact that in general all the measurements and simulations are performed each $5°$, the angles of attack of this section are rounded to the unit instead using them with one decimal as up to now.

As the three objectives depend on the total aerodynamic forces of the wing, only the results of the 3-dimensional forces are studied, not taking into account the 2-dimensional information. So, the different sets of results of interest are:

- 3D forces obtained from the force test on wind tunnel at $30\ m/s$.

- 3D forces calculated with the Prandtl Lifting Line theory from the 2D forces obtained from the pressure test on wind tunnel at $20\ m/s$, $30\ m/s$ and $40\ m/s$.

- 3D forces calculated with the Prandtl Lifting Line theory from the 2D forces obtained from numerical simulations at $40\ m/s$.

Before proceeding with the comparison of the different results, it is important to remark the limitations of the last two sets. These limitations come not only for the intrinsic ones of the Prandtl Lifting Line theory, but also due to the commented limitations of the two-dimensional data and due to the effects of the frame and the end-plates. Regarding the 2D forces obtained with the pressure test on the wind tunnel, as it was commented previously, they are not really 2-dimensional. They are affected by the 3D flow of the wing, and they can also be affected by the frame and the end-plates. It is true that the end-plates are a part of the wing. But, as their effect is not constant spanwise, it is not correct to have the effect included only in the way the end-plates affected a specific point spanwise. Regarding the frame, it could affect the pressure measures too.

Regarding the 2D forces obtained from numerical simulations, the 2-dimensionality is not the problem. But, apart from the limitations of the CFD models, the problem is found on the end-plates that are not really considered. In addition, more differences are expected with the directed measured 3D forces associated with the frame. Even though the contribution of the frame to the aerodynamic forces is subtracted, the frame modifies the flow around the aileron. Furthermore, there is a protuberance on the wing to joint it with the frame that is considered part of the wing for the wind tunnel forces test, and that is not considered on the Prandtl lifting line.

To decide the angle of attack that best fits the first objective, the Figure 95, where the ratio of downforce to drag is shown for the 5 sets of results, is used. Comparing all the set of results, it can be observed that the three sets that corresponded to the Prandtl Lifting line performed from wind tunnel data have not got a maximum. This behaviour differs from the one of the other two sets where there is a maximum. But this maximum does not coincide between both. The maximum for the Prandtl lifting line performed from simulations is unique at $\alpha = -16°$, even though the value of the ratio at $\alpha = -10.5°$ is similar. However, the zone of the maximum for the direct measurements of the wind tunnel is composed by a range between $\alpha = -27°$ and $\alpha = -17°$. Inside this values the maximum is placed at $\alpha = -27°$, but as in this range the value of the ratio varies less than 0.1, any of the angles can be considered as the one that achieves the objective 1.
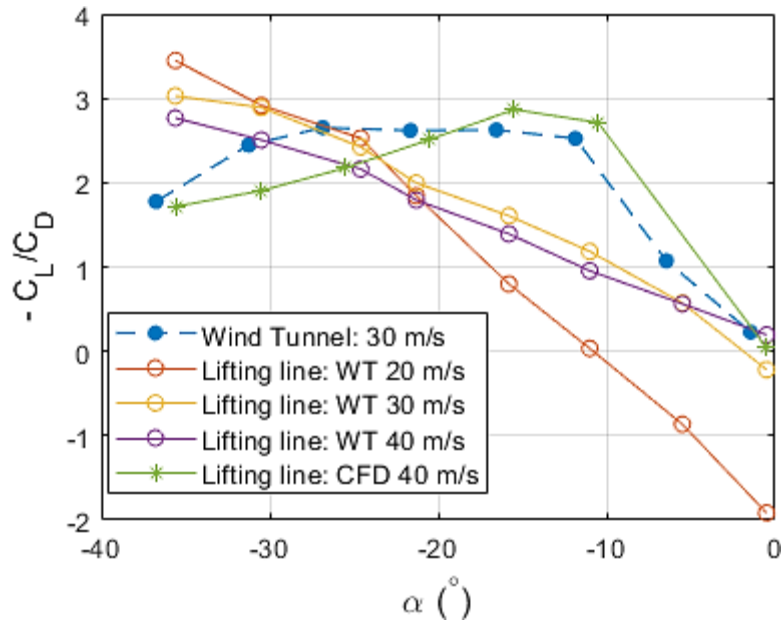
Figure 95. Comparison of the evolution of the ratio of negative lift coefficient to drag coefficient with α of all the results of the aileron isolated

So, as the α of maximum ratio of downforce to drag does not coincide for the different sets, the reliability of each result has to be taken into account. Even though the measurements of the forces test are affected by the frame, these measurements are more accurate as they are direct measurements and do not involve a limited theory as the rest. Nevertheless, there is still a problem, which is how to choose among the range that has the maximum ratio. In order to do that, two subobjectives are defined for the angles inside this range: the one of them with the maximum downforce (objective #1.1) and the one with minimum drag (objective #1.2).

Figure 96. Comparison of the evolution of negative lift coefficient with α of all the results of the aileron isolated

So, taking a look to the Figure 96 the objective #2 and objective #1.1 can be obtained. For the first one, this time there is an agreement between the different sets except for

the one of the lifting line performed from the numerical simulations. So, the angle that best fits the second objective is $\alpha = -31°$. Regarding the objective #1.1, as in the range of interest the downforce rises when α decreases, the sought angle is $\alpha = -27°$.

Finally, with the Figure 97 the objectives #3 and #1.2 are studied. This time the sets in agreement regarding the behaviour are the one of the force tests and the one of the Prandtl lifting line that uses the numerical simulations. For these two sets, the drag rises when α decreases, whereas for the three that correspond to the Prandtl lifting line performed from the wind tunnel results, there is a maximum at $\alpha = -21°$. However, all the results agree on the fact that the drag is smaller when α is about 1°. The problem is that no minimum is found for any of the sets. But, as this angle corresponds, more or less, to the angle of zero lift, it should be the one of less drag. Another problem relies, in fact, on this. As this angle produces no downforce, the aileron would be counter-productive as it only generates drag. So, it would be better to fit this objective to remove the aileron. However, on the rules of the competition it is not specified if this is allowed. So, assuming that this is not feasible, $\alpha = -1°$ is the angle for the third objective. Regarding the objective #1.2 and paying attention to force experiment results, the sought angle is $\alpha = -17°$.

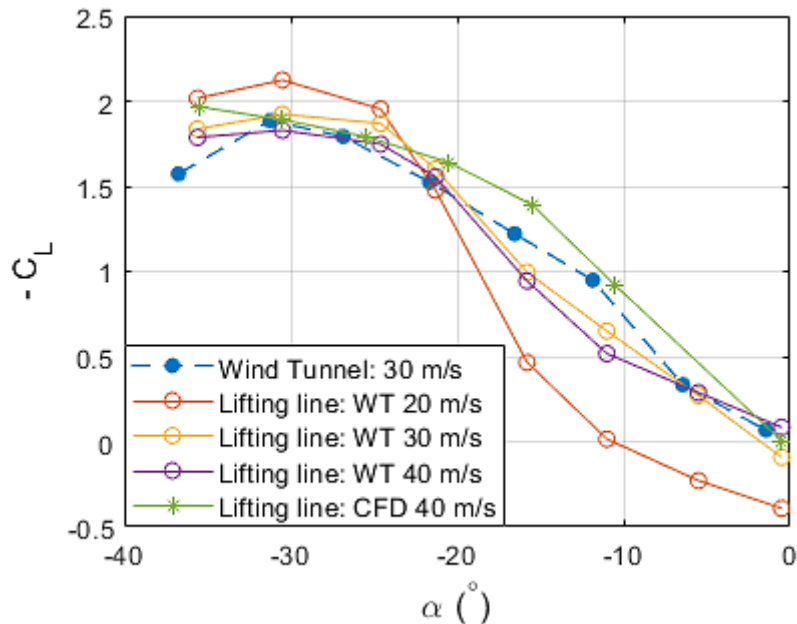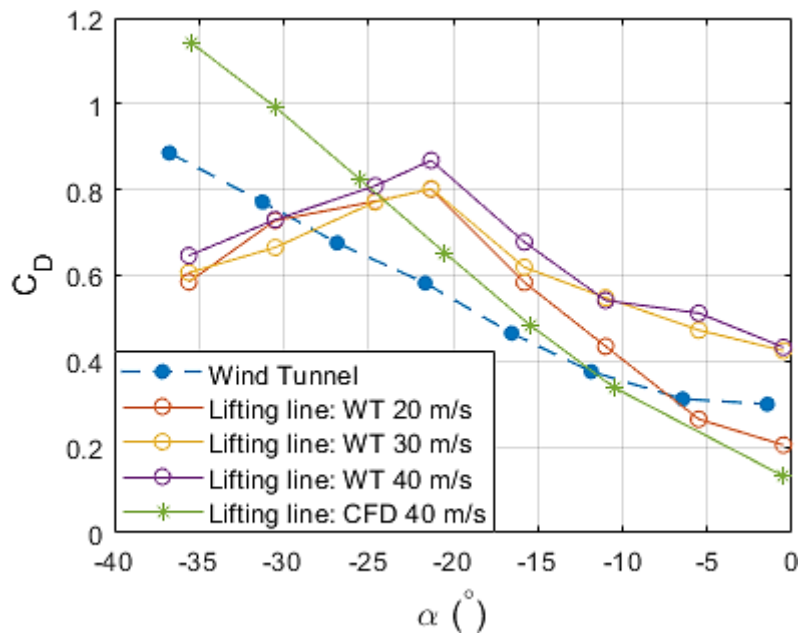*Figure 97. Comparison of the evolution of drag coefficient with α of all the results of the aileron isolated*

On Table 4, all these angles are shown.

Table 4. Angles of attack optimized for each objective for the aileron isolated

Objective	Angle of attack
#1	$-27°$ (#1.1: Maximum downforce)
	$-17°$ (#1.2: Minimum drag)
#2	$-31°$
#3	$-1°$

5.2. Optimization of the aileron with the car

On this section, the objective angles of attack are the same than the ones of the previous section, but this time, the effect of the car on the flow upstream the aileron is taken into account. As for the rest of the project, only the vertical deflection generated by the car on the flow is considered. This limits the amount of results that can be considered, as now there is no direct measurement. So, only the results obtained from the Prandtl Lifting Line are available. That is:

- 3D forces calculated with the Prandtl Lifting Line theory from the 2D forces obtained from the pressure test on wind tunnel, considering the α_{car} obtained from the wind tunnel test of the car at $20\ m/s$, $30\ m/s$ and $40\ m/s$.

- 3D forces calculated with the Prandtl Lifting Line theory from the 2D forces obtained from numerical simulations, considering the α_{car} obtained from the wind tunnel test of the car at $40\ m/s$.

The only difference between these sets of data, is the origin of the 2-dimensional characteristics. The respected limitations of each of the origins, numerical and experimental, have been commented on the previous section. Besides these sets of data, another one is included on the comparison. In previous chapters, it was observed that, on first approximation, the effect of the α_{car} was a shift of $8°$ rounded on the α. Therefore, the force test performed on the wind tunnel is included on this section, but applying on it this mentioned shift, so as to include the effect of the car.
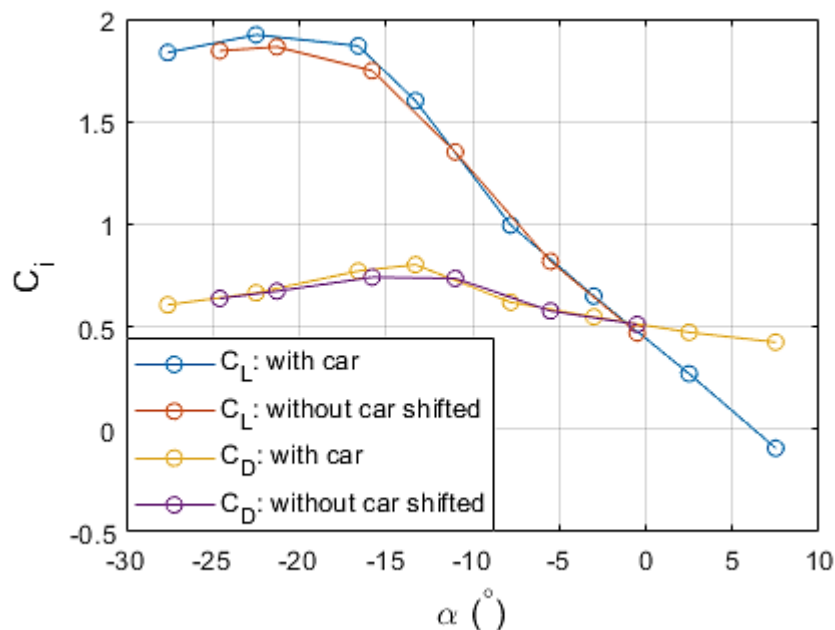

Figure 98. Lift and drag coefficients obtained with Prandtl lifting line from 2D wind tunnel results. Comparison between the results obtained with the car and the ones obtained without the effect of the car but shifted $8°$.

75

Even though the modification made on the wind tunnel force measurements in order to consider the effect of the car is only an approximation, it is still the most reliable result. This is like that, as the shift approximates very well the effect of α_{car} on the aerodynamic forces of the aileron. To check this, on Figure 98 the results obtained with the Prandtl lifting without the car shifted $8°$ and the results of the Prandtl lifting line with the car are shown. With this figure, it can be verified how the results of both sets are practically the same. The highest differences are found on the zones of the maximums, where the effect of the car produces a decrease that can not be represented with the shift. However, this reduction does not change considerably the behaviour of the curve or the angle of the maximum, so it could be negligible.

Figure 99. Comparison of the evolution of the ratio of negative lift coefficient to drag coefficient with α of all the results of the aileron affected by the car

Once it is checked that the more reliable set is the one of the force measurements performed on the wind tunnel, a similar reasoning than the one of the preceding section is used. For the first objective, there is again a range of α that accomplished it. This range is now between $\alpha = -19°$ and $\alpha = -9°$. Again, two subobjectives can be stablished with the angles of this range with maximum downforce and minimum lift, respectively. The angles that achieve these objectives are: $\alpha = -19°$ for the maximum downforce and $\alpha = -9°$ for the minimum drag.

Regarding the Figure 100, the angle of maximum downforce is placed at $\alpha = -23°$. Again, all the sets are, more or less, in agreement with this fact. Finally, the angle at which the drag is minimum is, once again, the highest one placed on the zone of zero lift. This time, the angle is $\alpha = 7°$.
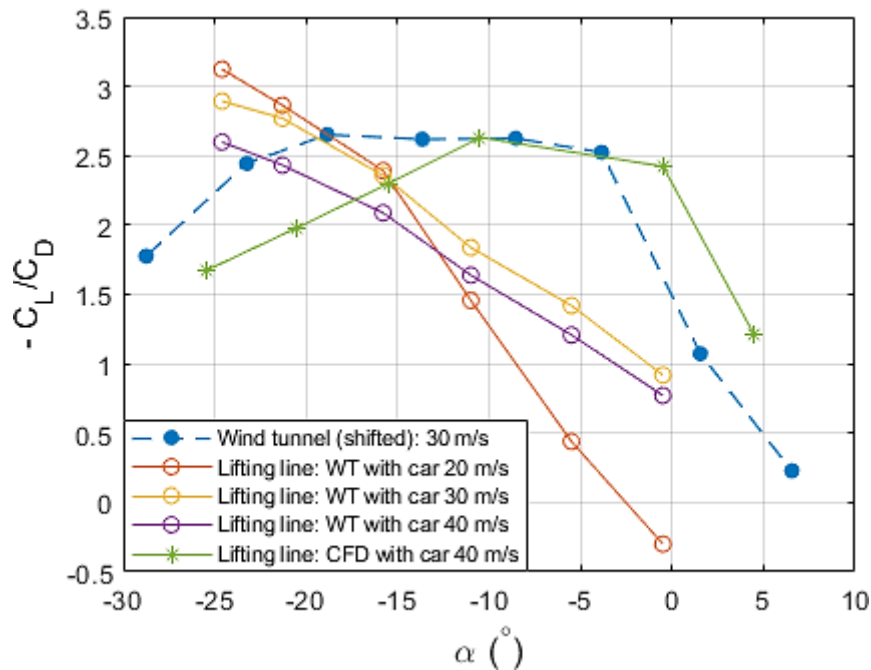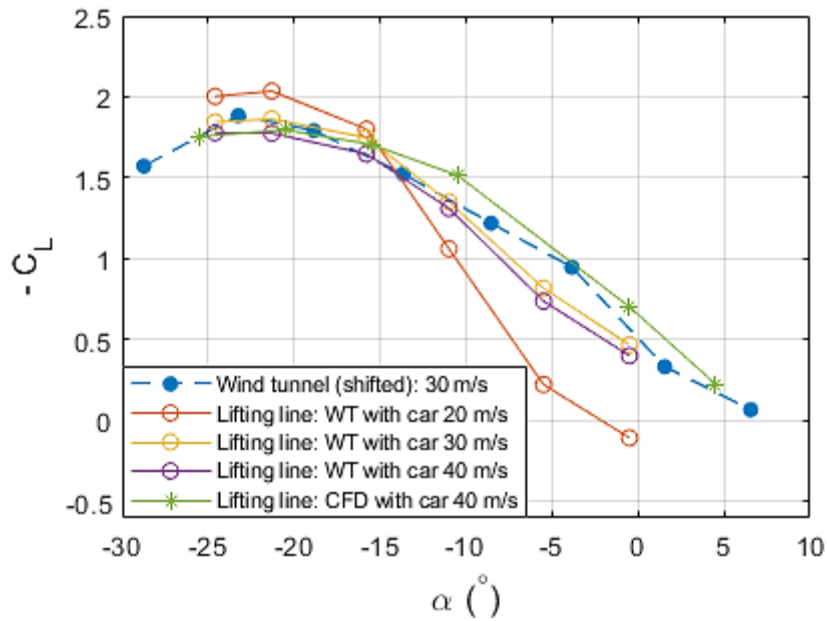
Figure 100. Comparison of the evolution of the negative lift coefficient with α of all the results of the aileron affected by the car.
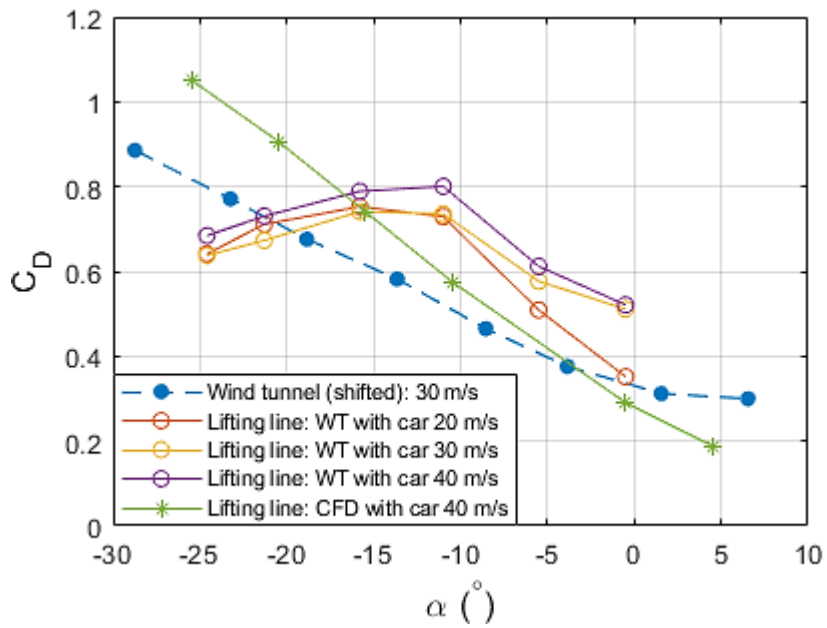
Figure 101. Comparison of the evolution of the drag coefficient with α of all the results of the aileron affected by the car.

All these results are collected on Table 5.

Table 5. Angles of attack optimized for each objective for the aileron with the effect of the car on the vertical deflection of the flow upstream the aileron

Objective	Angle of attack
#1	$-19°$ (#1.1: Maximum downforce)
	$-9°$ (#1.2: Minimum drag)
#2	$-23°$
#3	$7°$

6. Conclusion

6.1. Results and critical overview

In this work, the aileron of the Fun Cup race car has been optimized regarding the angle of attack. This optimization has been done considering different race conditions, so three different objectives have been defined:

- The α of maximum ratio of downforce to drag.

- The α of maximum downforce.

- The α of minimum drag.

This optimization has been done by means of wind tunnel experiments, that have been complemented with 2D numerical simulations.

Regarding the experiments, a total of two different experiments with the wing and one experiment with a scale model of the car have been performed. Even though in this work only the aileron of the car has been studied, the bodywork of the car deflects the flow seen by the aileron and, therefore, the performance of the car is modified. This has been studied by measuring the velocity vector at the rear part of the car, on the place where the aileron must be placed. Regarding the experiments performed on the wing, the goal of each of them was to measure the aerodynamic characteristics of the wing, globally and on a 2D profile, respectively. On the one hand, the global characteristics wer studied by measuring the aerodynamic forces with a balance. On the other hand, the 2D performance is obtained by measuring the pressure on the surface with a total of 31 taps distributed along the cited profile. Once the pressure along the 2D airfoil is obtained, the 2D lift and the 2D pressure drag are obtained.

Once the experiments were conducted, the 2D forces and the vertical deflection of the flow upstream of the aileron generated by the car were combined with the Prandtl lifting line theory to obtain the 3D performance of the aileron when is placed on the car. The Prandtl lifting line allows to calculate the three-dimensional performance from the 2D forces by accounting the effects of the shed tip vortices. This effect is measured by calculating the induced angle of attack along the span. As the effect of the car on the flow is 3-dimmensional too, the addition of the α_{car} (vertical deflection of the flow induced by the car upstream of the aileron) to the lifting line formulation allows to obtain the 3D forces of the aileron placed on the race car.

As the 2-dimensional measurements performed on the wind tunnel are affected by three-dimensional effects, they are complemented with numerical simulations. Since the

wing can be considered a bluff body, the flow around it is unsteady, so the simulations performed were unsteady too. The simulations have been performed with two different models: the transition $\gamma - Re$ model and the SST $k - \omega$ model. The results obtained from both methods have been compared, obtaining some differences but, in general, similar results. By comparing the results of the mean values of this two methods with the ones of the wind tunnel pressure test, taking into account the limitations of the experimental results, the SST $k - \omega$ model has been selected as the most adequate for the study.

The numerical simulations have been used not only for obtaining a new set of 2D forces, but also to study the behaviour of the flow around the wing. Regarding the 2D forces, as well as it was done with the one obtained from the wind tunnel measurements, the 3D forces are obtained with the Prandtl lifting line theory in combination with the results of α_{car}.

With regard to the physics of the flow, a highly unsteady component has been obtained, confirming what it was expected due to the non-streamlined shape of the profile. Analysing the velocity field, it was observed a large separation of the flow that leads to shedding vortices. In addition, on the pressure side (upper side) a recirculation zone can be observed too. This behaviour of the flow explains the bad performance of the aileron, measured with the ratio of downforce to drag, whose value is less than 3 for all the measured conditions.

After presenting and analysing all the results from the different experiments, from the simulations and from the Prandtl lifting line theory, they are used to optimize the α of the aileron for each of the three objectives. This optimization has been done firstly for the aileron on the wind tunnel conditions, that is, without accounting the effect of the car on the flow. To this optimization the measurements obtained on the wind tunnel force test have been used preferentially.

Finally, analysing the effect of the α_{car} on the lift and drag through the Prandtl lifting line, it can be approximated as a reduction on the effective angle of attack on $8°$. With this consideration, the results of the wind tunnel force test are adapted by shifting the angle of attack $+8°$. So, the final optimization is the same one than the one without the effect of the car but at angles of attacks of $8°$ higher. The first objective, maximum downforce-to-drag ratio, is achieving in all the range between $\alpha = -19°$ and $\alpha = -9°$, where $\alpha = -19°$ corresponds to the maximum downforce inside this range and $\alpha = -9°$ to the minimum drag. The second objective, maximum downforce, is accomplished at $\alpha = -23°$. And, the third objective, minimum drag, occurs at the zero lift α that is $\alpha = 7°$.

6.2. Future works

In this work, the aerodynamics of the aileron of the Fun Cup Evo 3 race car are studied concentrating on the effect of the angle of attack. However, the study of the aerodynamics of this aileron is much wider. Furthermore, the aileron does not constitute the only element of the car that has an effect on the aerodynamics of the car, so the study can be extended to the bodywork or the front spoiler. Hence, there are multiples

lines of investigation for future works that can be divided into three groups: wind tunnel experiments, numerical simulations and application of the lifting line.

Regarding the execution of new wind tunnel experiments:

- In order to complement the flow visualization obtained from the numerical simulations performed on this work, techniques that allow the experimental visualization of the flow, as the Particle Image Velocimetry (PIV), can be implemented. In addition, not only the 2D could be analysed, but also the 3D effects can be observed.

- As the effect of the aileron on the race car is especially important in corners, the yaw angle can be obtained. Both the pressure test and the force test could be performed at different yaw angles.

- The aerodynamic forces of the bodywork could be studied at several yaw angles and different velocities with the scale model. In addition, flow visualization techniques could be applied on this model to complement the measurements of the deflection of the flow upstream of the aileron. These studies could be done with and without a scale aileron.

Regarding the implementation of new numerical simulations:

- With the 2D numerical model developed, a more exhaustive study regarding the angle of attack effect around the α of interest could be performed in order to obtain more precise angles.

- In addition, the unsteady component of the flow could be further studied, with an analysis on the evolution of the Strouhal number.

- Numerical simulations on a 3D model of the wing can be performed. With this model both the effect of the angle of attack and the yaw angle can be studied, besides to the Reynolds effect.

- The aerodynamic characteristics of the bodywork could be extensively studied with a numerical 3D model. These characteristics can be studied for different yaw conditions too. Furthermore, this model can be used to the study of the deflection of the flow upstream the aileron. Adding the aileron and the frame to this model, a complete numerical study can be performed.

Regarding the aspects of the flow study with the Prandtl lifting line, in addition to the study of the effect of α_{car} on the performance of the aileron, the effective velocity and the β_{car} can be studied too, with some modifications of the formulation.

Finally, all these studies and performance at optimized α could be verified with on-track measurements.

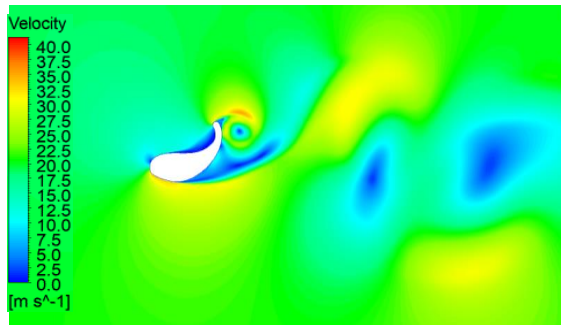# Appendix I. Velocity fields from numerical $\gamma - Re$ Transition model

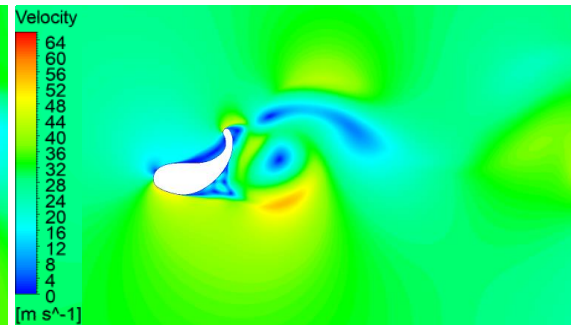*Figure 102. Velocity field in a particular time instance obtained with the numerical $\gamma - Re$ Transition model at $\alpha = -30.5°$ and $U_\infty = 20 \, m/s$.*

Figure 103. Velocity field in a particular time instance obtained with the numerical $\gamma - Re$ Transition model at $\alpha = -30.5°$ and $U_\infty = 30 \, m/s$.
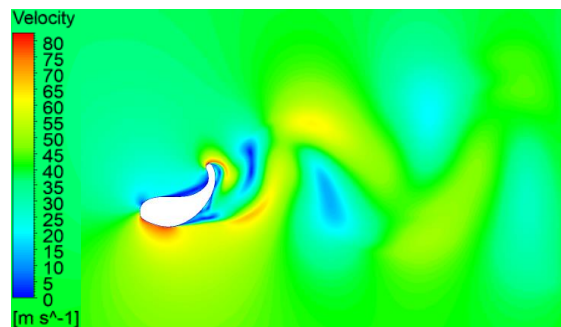

Figure 104. Velocity field in a particular time instance obtained with the numerical $\gamma - Re$ Transition model at $\alpha = -30.5°$ and $U_\infty = 40 \, m/s$.

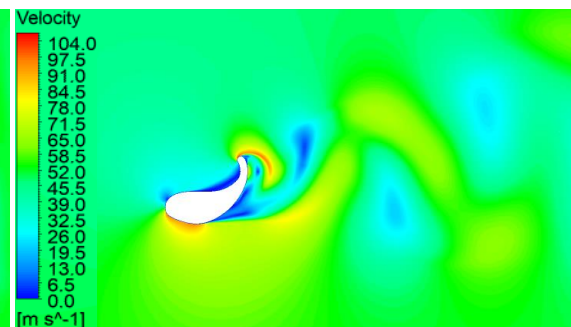*Figure 105. Velocity field in a particular time instance obtained with the numerical $\gamma - Re$ Transition model at $\alpha = -30.5°$ and $U_\infty = 50 \, m/s$.*

Figure 106. Velocity field in a particular time instance obtained with the numerical $\gamma - Re$ Transition model at $\alpha = -35.5°$ and $U_\infty = 40 \, m/s$.
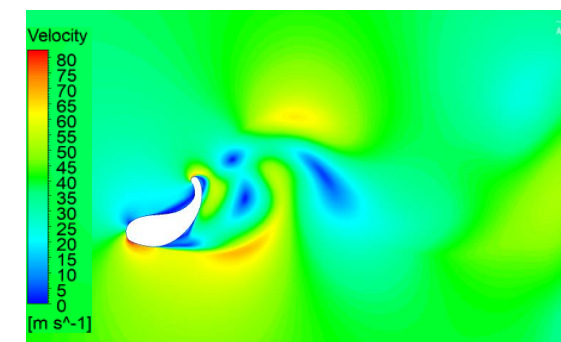

Figure 107. Velocity field in a particular time instance obtained with the numerical $\gamma - Re$ Transition model at $\alpha = -25.5°$ and $U_\infty = 40 \, m/s$.

Figure 108. Velocity field in a particular time instance obtained with the numerical $\gamma - Re$ Transition model at $\alpha = -20.5°$ and $U_\infty = 40 \, m/s$.
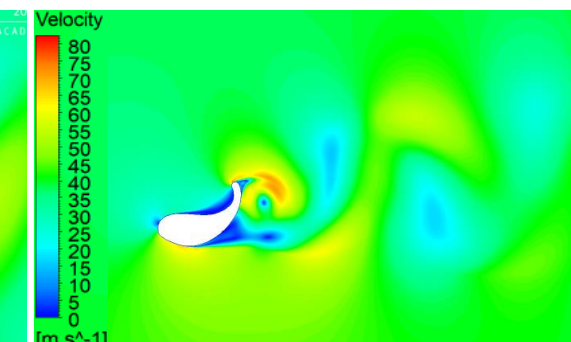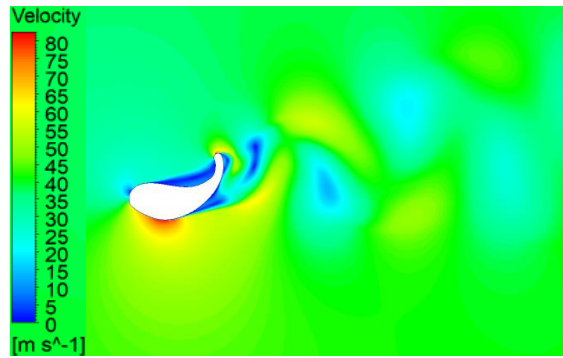

Figure 109. Velocity field in a particular time instance obtained with the numerical $\gamma - Re$ Transition model at $\alpha = -15.5°$ and $U_\infty = 40 \, m/s$.
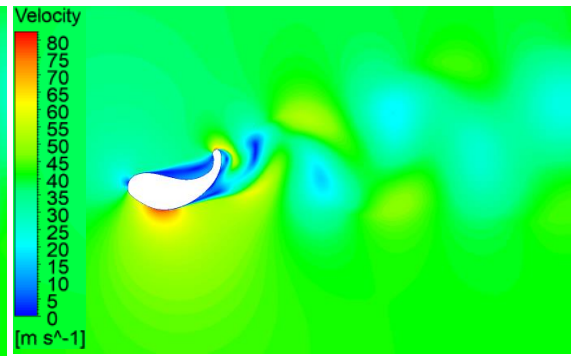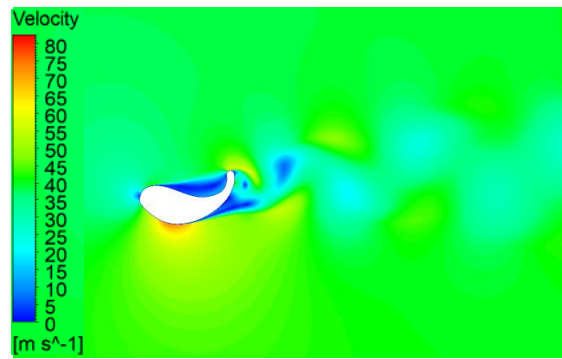

Figure 110. Velocity field in a particular time instance obtained with the numerical $\gamma - Re$ Transition model at $\alpha = -10.5°$ and $U_\infty = 40 \, m/s$.

Bibliography

[1]   J. Katz, «Mechanix Illustrated,» TechnicaCuriosa, 2017. [En línea]. Available: https://mechanixillustrated.technicacuriosa.com/2017/03/04/an-introduction-to-automobile-aerodynamics/.

[2]   A. M. I. Mukut y M. Z. Abedin, «Review on Aerodynamic Drag Reduction of Vehicles,» *International Journal of Engineering Materials and Manufacture,* vol. 4, pp. 1-14, 2019.

[3]   J. Katz, «Overview: Aerodynamics and Race Cars,» de *Race Car Aerodynamics: Designing for Speed*, Bentley Publishers, 1995, pp. 1-22.

[4]   J. Katz, «Aerodynamics of Race Cars,» *Annual Review of Fluid Mechanics,* vol. 38, pp. 27-63, 2006.

[5]   J. Katz, «Aerodynamics of the Complete Vehicle,» de *Race Car Aerodynamics: Designing for Speed*, Bentley Publishers, 1995, pp. 179-242.

[6]   Université de Liège, «The University of Liège Wind Tunnel Facility - Technical description,» 2009.

[7]   ANSYS, Inc, «4.11 Large Eddy Simulation (LES) Model,» de *ANSYS FLUENT 12.0 Theory Guide*, 2009.

[8]   ANSYS, Inc, «4.2.1 Reynolds-Averaged Approach vs. LES,» de *ANSYS FLUENT 12.0 Theory Guide*, 2009.

[9]   ANSYS, Inc., «4.2.2. Reynolds (Ensemble) Averaging,» de *ANSYS FLUENT 12.0 Theory Guide*, 2009.

[10]   ANSYS, Inc., «4.2.3. Boussinesq Approach vs. Reynolds Stress Transport Models,» de *ANSYS FLUENT 12.0 Theory Guide*, 2009.

[11]   ANSYS, Inc., «4.5 Standard and SST k - omega Models,» de *ANSYS FLUENT 12.0 Theory Guide*, 2009.

[12]   F. R. Menter, «Two-Equation Eddy-Viscosity Turbulence Models for Engineering Applications,» *AIAA Journal,* vol. 32, nº 8, pp. 1598-1605, 1994.

[13]   J. Ke y J. Edwards, «RANS and LES/RANS Simulation of Airfoils under Static,» de *51st AIAA Aerospace Sciences Meeting*, Texas, 2013.

[14]   ANSYS, Inc., «4.7 Transition SST Model,» de *ANSYS FLUENT 12.0 Theory Guide*, 2009.

[15]   ANSYS, Inc., «18.1 Overview of Flow Solvers,» de *ANSYS FLUENT 12.0 Theory Guide*, 2009.

[16]   J. M. Calleja Vazquez, *Master thesis: Experimental and numerical analysis of the aerodynamics of the A&M Shell Eco-marathon vehicle prototype,* Liège, 2017-2018.

[17]   ANSYS, Inc., «4.12. Near-Wall Treatments for Wall Bounded Turbulent Flows,» de *ANSYS FLUENT 12.0 Theory Guide*, 2009.

[18]   ANSYS, Inc., «7.3.4 Velocity Inlet Boundary Conditions,» de *ANSYS FLUENT 12.0 Theory Guide*, 2009.

[19]   ANSYS, Inc., «7.3.8. Pressure Outlet Boundary Conditions,» de *ANSYS FLUENT 12.0 Theory Guide*, 2009.

[20]   W. F. Phillips y D. O. Snyder, «Modern Adaptation of Prandtl's Classic Lifting-Line Theory,» *JOURNAL OF AIRCRAFT,* vol. 37, nº 4, pp. 662-670, 2000.

[21]   J. D. Anderson Jr., S. Corda y D. M. Van Wie, «Numerical Lifting Line Theory Applied to Drooped Leading-Edge Wings Below and Above Stall,» *JOURNAL OF AIRCRAFT,* vol. 17, nº 12, pp. 898-904.

[22]   J. Meseguer Ruiz y Á. Sanz Andrés, Aerodinámica Básica, Garceta, 2011.

[23]   T. Merlin, «Multidisciplinary Design in Aeronautics, Enhanced by Simulation-Experiment Synergy».

[24]   H. Glauert, «Chapter XI. The Monoplane Airfoil,» de *The elements of aerofoil and airscrew theory*, Cambridge Science Classics, 1947.

[25]   D. R. Riley, «Wind-Tunnel Investigation and Analysis of the Effects of End Plates on the Aerodynamic Characteristics of an Unspwept Wing,» National Advisory Committee for Aeronautics, Washington, 1951.